

VEGAS: A VST Early-type Galaxy Survey.

I. Presentation, wide-field surface photometry, and substructures in NGC 4472

Massimo Capaccioli^{1,2}, Marilena Spavone¹, Aniello Grado¹, Enrichetta Iodice¹, Luca Limatola¹, Nicola R. Napolitano¹, Michele Cantiello³, Maurizio Paolillo², Aaron J. Romanowsky^{4,5}, Duncan A. Forbes⁶, Thomas H. Puzia^{7,8}, Gabriella Raimondo³, and Pietro Schipani¹

¹ INAF-Astronomical Observatory of Capodimonte, Salita Moiarriello 16, I80131, Naples, Italy
e-mail: capaccioli@na.infn.it

² University of Naples Federico II, C.U. Monte Sant'Angelo, Via Cinthia, 80126, Naples, Italy

³ INAF-Astronomical Observatory of Teramo, Via Maggini, 64100, Teramo, Italy

⁴ Department of Physics and Astronomy, San José State University, One Washington Square, San José, CA 95192, USA

⁵ University of California Observatories, 1156 High Street, Santa Cruz, CA 95064, USA

⁶ Centre for Astrophysics & Supercomputing, Swinburne University, Hawthorn, VIC 3122, Australia

⁷ Institute of Astrophysics, Santiago, Chile,

⁸ National Research Council Canada, Victoria, Canada

Received; accepted ...

ABSTRACT

Context. We present the VST Early-type Galaxy Survey (VEGAS), which is designed to obtain deep multiband photometry in g, r, i , of about one hundred nearby galaxies down to 27.3, 26.8, and 26 mag/arcsec² respectively, using the ESO facility VST/OmegaCAM. **Aims.** The goals of the survey are 1) to map the light distribution up to ten effective radii, r_e , 2) to trace color gradients and surface brightness fluctuation gradients out to a few r_e for stellar population characterization, and 3) to obtain a full census of the satellite systems (globular clusters and dwarf galaxies) out to 20% of the galaxy virial radius. The external regions of galaxies retain signatures of the formation and evolution mechanisms that shaped them, and the study of nearby objects enables a detailed analysis of their morphology and interaction features. To clarify the complex variety of formation mechanisms of early-type galaxies (ETGs), wide and deep photometry is the primary observational step, which at the moment has been pursued with only a few dedicated programs. The VEGAS survey has been designated to provide these data for a volume-limited sample with exceptional image quality.

Methods. In this commissioning photometric paper we illustrate the capabilities of the survey using g - and i -band VST/OmegaCAM images of the nearby galaxy NGC 4472 and of smaller ETGs in the surrounding field.

Results. Our surface brightness profiles reach rather faint levels and agree excellently well with previous literature. Genuine new results concern the detection of an intracluster light tail in NGC 4472 and of various substructures at increasing scales. We have also produced extended $(g-i)$ color profiles.

Conclusions. The VST/OmegaCAM data that we acquire in the context of the VEGAS survey provide a detailed view of substructures in the optical emission from extended galaxies, which can be as faint as a hundred times below the sky level.

Key words. Techniques: image processing – Galaxies: elliptical and lenticular, cD – Galaxies: fundamental parameters – Galaxies: formation

1. Introduction

Recent years have witnessed renewed interest in bright early-type galaxies (ETGs). Observations at high redshift revealed that ETGs have undergone remarkable amounts of size evolution over time (e.g., Daddi et al. 2005; van Dokkum et al. 2010). Theory suggests this growth to be a basic aspect of hierarchical structure formation, with mergers building up extended bulges and stellar halos (Oser et al. 2010; Hopkins et al. 2010).

The new paradigm of “two-phase” or “inside-out” galaxy assembly, pictured by cosmological simulations, outlines two regimes in the formation of the baryonic structure of a galaxy.

In a first early ($z \gtrsim 2$) phase there is rapid in situ star formation from infalling cold gas, followed by a longer accretion phase where the system considerably grows in size and mass by accreting smaller satellites. This new paradigm motivates a return to classical studies of nearby ETGs, searching for the expected signatures of formational processes, particularly at large radii.

Pilot studies have indeed revealed extensive evidence of outer galaxy assembly: from pervasive photometric substructures (Tal et al. 2009; Janowiecki et al. 2010) to metallicity gradients (Coccato et al. 2010; Forbes et al. 2011), rotational changes (Proctor et al. 2009; Coccato et al. 2009; Arnold et al.

2011), and accretion signatures in chemo-dynamical phase space (Romanowsky et al., 2012).

A full understanding of any galaxy begins with photometry. The situation for nearby ETGs is the following: the central regions are studied in much detail (e.g., Ferrarese et al. 2006, F+06 hereafter; Côté et al. 2007), while the faint outskirts are still poorly investigated, even if they are becoming a hot topic with multiple surveys being carried out (e.g., Kormendy et al. 2009, K+09 hereafter, Duc et al. 2015). (e.g., Kormendy et al. 2009, K+09 hereafter, Duc et al. 2015). There is a critical need for modern, wide-field (WF), multiband CCD photometry of a large sample of galaxies in a broad range of environments, replacing the photographic and narrow-field CCD work of decades past (e.g., Peletier et al. 1990; Caon et al. 1994). The aim is to systematically gauge the basic global properties of ETGs over a wide baseline of sizes: luminosity profiles, isophote shapes, substructure characteristics, color gradients, surface brightness fluctuations, inventories of satellite galaxies and globular clusters (GCs), etc. The wide range of science results and applications available from such a dataset, beyond the general goal of testing two-phase assembly models, cannot be covered here, therefore we briefly highlight a few topics.

Multiband surface brightness (SB) mapping of ETGs allows us to measure key physical parameters through the fit of generalized $R^{1/n}$ profiles (Caon et al., 1993): total luminosity, Sersic index n , effective surface brightness and radius, μ_e and R_e , boxy- or diskyness, etc. (Caon et al. 1993; Balcells et al. 2007). The correlations between them, such as μ_e vs R_e , mass vs size or photometric plane (Kormendy 1985; Capaccioli et al. 1992; Shen et al. 2003) help shedding light into formation processes. Along the same line, outer breaks in the SB profiles might correlate in a non-trivial way with the inner core or cusp transition (e.g., Côté et al. 2007); this has not been studied so far. Moreover, photometry is a way to identify and gauge substructure and/or light excesses as expected from the diffuse stellar components (e.g., Zibetti et al. 2005), especially in the intracluster environment (Mihos et al. 2005; Mihos et al. 2013), through deviations from the regular $R^{1/n}$ behavior. Radial color gradients are critically related to the formation mechanisms (Carlberg, 1984) because they give a hint of the different distributions in stellar ages and metallicities (Saglia et al. 2002; Pipino et al. 2008; Tortora et al. 2011). The combination of color distribution with surface brightness fluctuations (SBF, Tonry & Schneider 1988) supplies further information on the chemical properties of the stellar populations and helps lift the age-metallicity degeneracy out to a few effective radii (Cantiello et al., 2013).

Furthermore, accurate photometry up to $10 R_e$ is mandatory (and still lacking) for dark matter studies because of the advent of efficient kinematical tracers such as the planetary nebulae (PNe, e.g., Romanowsky et al. 2003; Napolitano et al. 2009) and globular clusters (GCs, e.g., Romanowsky et al. 2009, Napolitano et al. 2014). In particular, extended deep photometric mapping will naturally provide a fairly complete census of galaxy satellites, from globular clusters (GCs) to satellite galaxies: a multipurpose database that is also useful for testing the formation scenarios.

Among the key questions that still remain open there is the well-known bimodality of the color distribution of GCs in galaxies (e.g., Peng et al. 2006). This has different possible explanations: i) either high-redshift, two-phase formation of elliptical systems (e.g., Forbes et al. 1997), ii) the dissipative merging of late-type spirals (e.g., Ashman & Zepf 1992); iii) the hierarchical feeding of a bright (metal-rich) elliptical by (metal-poorer) dwarfs (e.g., Côté et al. 1998), iv) the recent proposal of a uni-

modal metallicity distribution that is transformed into a bimodal color distribution because of the nonlinearity of color-metallicity relations (e.g., Yoon et al. 2006, Cantiello et al. 2015, and references therein). Although a unique consensus on the interpretation of this phenomenon is still lacking, we note that as in the Milky Way GC system, the systems of several other early-type galaxies are clearly bimodal in metallicity (Brodie et al. 2012, 2014; Usher et al. 2012, 2015).

Finally, satellite galaxies are important because they can be tidally disrupted in their journey around larger systems. These events are possibly the mechanisms producing the diffuse halos around galaxies (Ibata et al. 1994; Zibetti et al. 2004; Arnaboldi et al. 2012) or even the intragroup or cluster light (Mihos et al. 2013; Zibetti et al. 2005).

In view of all this and considering the special characteristics of the VLT Survey Telescope (VST; Capaccioli & Schipani 2011), a project for a photometric survey of nearby ETGs, dubbed VEGAS, has been undertaken on the Italian Guaranteed Time Observation (GTO). This is the first paper of a series where we present the survey project and its strategy, the data reduction and analysis techniques, and report on a test case conducted to assess and certify the quality of our products.

The paper is organized as follows. In Sect. 2 we briefly describe the VEGAS survey aims and objectives. The observations of a test galaxy are described in Sect. 3. In Sect. 4 we illustrate the strategies adopted for the data analysis, with a particular emphasis on the determination of the sky background and the measurement of accurate surface brightness profiles. In Sect. 5 we discuss the surface brightness profiles of the objects in this study and compare results with previous literature, while in Sect. 6 we discuss the effects of the scattered light on the surface brightness profiles. Finally, in Sect. 7 we discuss that the VST/OmegaCAM data are of the highest quality for wide-field imaging and why we believe that this machinery is a powerful tool for an “industrial” analysis of optical photometry of nearby galaxies. In Appendix A and B we describe the details of the data reduction and of the point spread function.

We adopt a distance modulus for the Virgo cluster of 31.14 ± 0.05 mag as in Mei et al. (2007). This correspond to a distance of 16.9 Mpc, so 1 arcsec is 81.9 pc. The magnitudes throughout the paper are in the AB system. Our surface brightness data are not corrected for Galactic extinction, but the total magnitude values listed in Table 1 have been corrected assuming the recipe of Arrigoni Battaia et al. (2012).

2. VEGAS survey

The VST Elliptical GALaxies Survey (VEGAS) is a deep multiband (g, r, i) imaging survey of early-type galaxies in the southern hemisphere carried out with VST at the ESO Cerro Paranal Observatory (Chile). The large field of view (FOV) of the OmegaCAM mounted on VST (one square degree matched by pixels 0.21 arcsec wide), together with its high efficiency and spatial resolution (typically better than 1 arcsec; Kuijken 2011) allows us to map with a reasonable integration time the surface brightness of a galaxy out to isophotes encircling about 95% of the total light. Observations started in October 2011 (ESO Period 88), and since then, the survey has acquired exposures for about 20 bright galaxies (and for a wealth of companion objects in the field), for a totality of ~ 80 hr (up to Period 93).

Since the OmegaCAM detector is a mosaic of 32 CCDs, a dithering strategy has to be devised to fill the blind gaps among the 2000×4000 pixels of individual CCDs. The actual implementation of the dithering strategy has consequences for setting

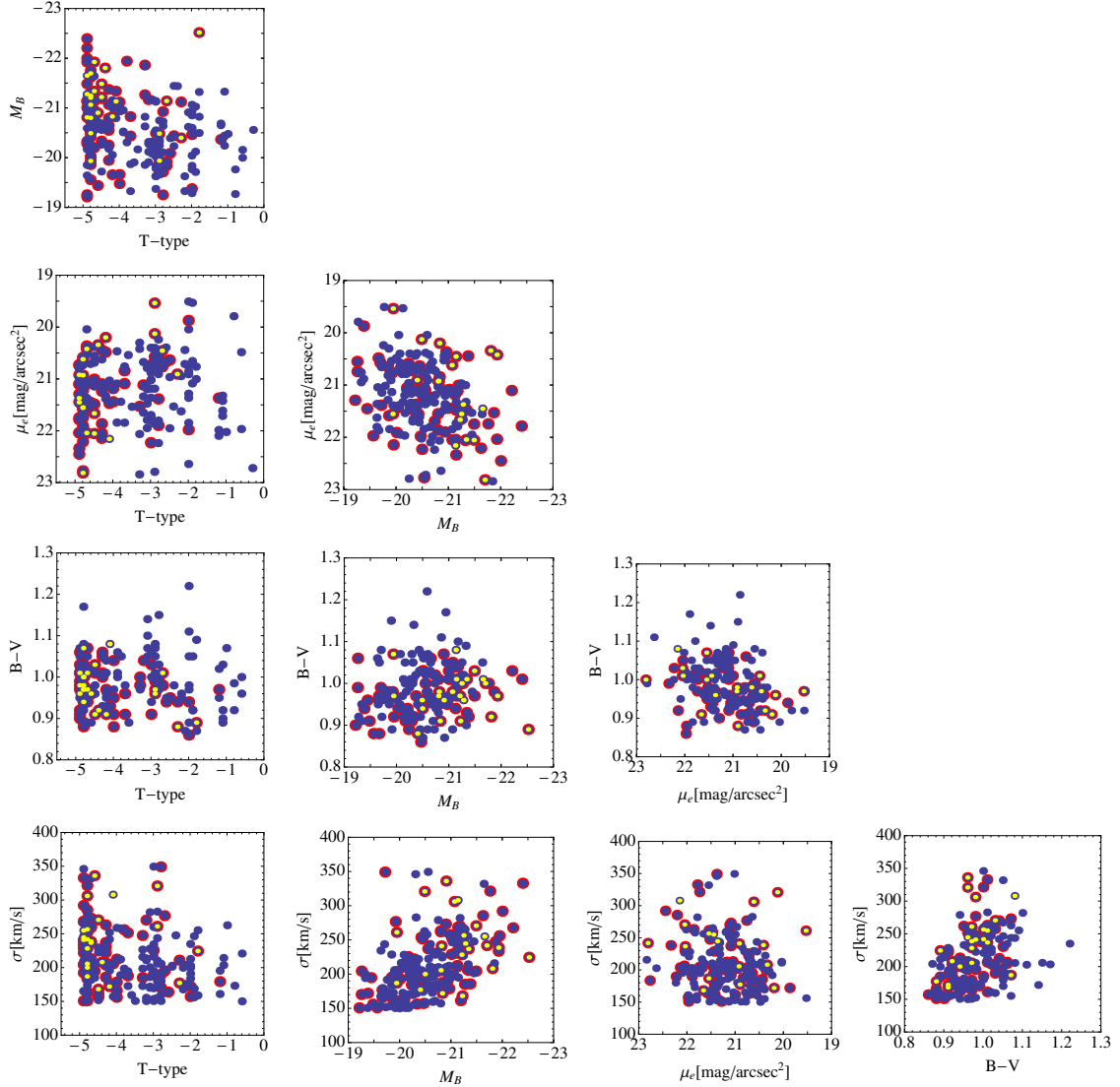


Fig. 1. VEGAS potential target distribution in the parameter space (blue points). Higher priority is given to galaxies with HST data (red circles) and Chandra/XMM data (yellow dots). We note that close systems are observed in a single VST/OmegaCAM pointing in many cases.

the weight map of the various pixels of the final combined image, as well as for mixing and averaging the residual errors in the engineering of the individual CCDs because of the overlapping of adjacent CCDs.

The survey project is designed to map the surface brightness of galaxies with $T_{type} < 0$, $\sigma > 150$, $Dec < +5$, $V_{rad} < 4000$ km/s, and $B_{tot} < -19.2$, sampling all environmental conditions and the whole parameter space. To this end, we selected from the catalog of nearby galaxies by Prugniel & Simien (1996) a large sample of about 240 potential E/S0 targets (Fig. 1) with the aim of optimizing the observing strategy throughout the year so as to observe half of this sample in five years and to uniformly cover the galaxy parameter space.

The distribution of parameters in Fig. 1 refers to the central targets of the VEGAS pointings, while we expect to simultaneously observe many lower luminosity systems. Higher priority is given to galaxies with ancillary data (e.g., *HST* or *Chandra/XMM*, see Fig. 1).

The expected depths at a signal-to-noise ratio (S/N) of > 3 in the g , r , and i bands are 27.3, 26.8, and 26 mag arcsec $^{-2}$,

respectively. They are the result of a compromise between a reasonable exposure time and the need to detect signatures of a diffuse stellar component around galaxies (see, e.g., Zibetti et al. 2005) and the dynamical interaction of ETGs with the intergalactic medium.

The main products of the VEGAS survey are 1) a 2D light distribution out to 8-10 R_e : galaxy structural parameters and diffuse light component, inner substructures as a signature of recent cannibalism events, inner disks and bars fueling active nuclei present in almost all the objects of our sample; 2) radially averaged surface brightness profiles and isophote shapes out to 10 R_e ; 3) color gradients and the connection with galaxy formation theories; 4) detection of external low-surface brightness structures of the galaxies and the connection with the environment; 5) census of small stellar systems (SSS: GCs, ultra-compact dwarfs and galaxy satellites) out to $\sim 20 R_e$ from the main galaxy center, and their photometric properties (e.g., GC luminosity function and colors, and their radial changes out to several R_e), allowing us to study the properties of GCs in the outermost “fossil” regions of the host galaxy. This latter subproject is also called

Table 1. Parameters of NGC 4472

Parameter	Value	Ref.
Morphological type	E2	RC3
R.A. (J2000)	12h29m46.7s	NED
Dec. (J2000)	+08d00m02s	NED
Helio. radial velocity	981 km/s	NED
Distance	16.9 Mpc	Mei et al. (2007)
Mean axis ratio	0.81	NED
Absolute magnitude M_g	-22.85 ^a	This work
Absolute magnitude M_i	-24.22 ^a	This work

Notes. ^(a) Corrected for interstellar extinction as in Arrigoni Battaia et al. (2012).

VEGAS-SSS (Cantiello et al., 2015). We note that the majority of studies on the photometric properties of the GC system in ETGs cover the central (few arcmin) region of the host galaxy (e.g., ACS Virgo & Fornax cluster surveys, Côté et al. 2004 and Jordán et al. 2007). An exception to the inner imaging studies is the SLUGGS survey that uses the Subaru/Suprime camera (e.g., Blom et al. 2012).

As a natural byproduct of the survey (for the depth and high S/N in the central galaxy regions), a galaxy SBF, and a SBF-gradient analysis is planned to chemically characterize the stellar population within $\sim 2R_e$ (or more, for the nearest ETGs in the sample).

A fundamental aspect of the survey resides in the legacy value of the data-set for ETGs, to be used for a wide range of research lines. The survey area extends from -70 to $+5$ degrees in Dec and $0-24$ h in RA (see Fig. 1), which ensures observability throughout the year and an advantageous overlap with the KiDS survey area (de Jong et al., 2013).

VEGAS will provide a volume-limited survey in the South complementary to the Next Generation Virgo Cluster Survey (NGVS, Ferrarese et al. 2012), with similar depth but no environmental restrictions, and will be the southern equivalent to MATLAS (Duc et al., 2015). The updated status of VEGAS observations is posted at the link <http://www.m2teamsoftware.it/vst/index.php/science/gto-surveys/vegas>.

3. NGC 4472 field: observations and data reduction

This first VEGAS paper presents a deep photometric analysis of the ETGs in the VST field of the galaxy NGC 4472 (M 49), the brightest member of the Virgo cluster (Table 1). We have chosen this field for the following reasons:

- it is well-studied with an ample scientific photometric literature (Kim et al. 2000; Ferrarese et al. 2006; Kormendy et al. 2009; Janowiecki et al. 2010; Mihos et al. 2013);
- it offers a wide range of cases for investigating the ability of VEGAS to map the faint galaxy outskirts. Together with this supergiant nearby object that fills almost the entire OmegaCAM field, there are smaller ETGs either embedded in the light of NGC 4472 or close to the edges of the frame (see Fig. 2). Each one of these cases requires a different data reduction strategy and calls for an independent verification.

The data used in this paper consist of exposures in g and i SDSS bands (Table 2) obtained with VST + OmegaCAM in service mode under photometric sky conditions and with the following constraints:

Table 2. VST exposures used in the photometry of the NGC 4472 field.

Band	Date	Nr. frames	Total exp. time [sec]	FWHM ^a [arcsec]
g	2013-03-19	5	1225	0.83
	2013-03-20	5	1225	1.40
	2013-04-15	10	2120	0.85
	2013-04-16	5	1125	0.92
i	2013-03-19	5	1250	0.66
	2013-04-16	10	1670	0.73
	2013-05-14	10	1670	0.77

Notes. ^(a) Median value of the FWHM.

- S/N ≥ 3 per arcsec²;
- dark time;
- seeing $\leq 1''$;
- airmass ≤ 1.2 .

For the sake of clarity, we repeat that the FOV of each frame covers one square degree, with a scale of 0.21 arcsec pixel⁻¹. The total integration time is 5695 seconds in g and 4590 seconds in i . The different exposures have the same center, which has been chosen not to coincide with that of NGC 4472, principally in order to move the galaxy core out of the central crossing of the gaps. More details about the dithering strategy can be found in the VST manual at the following link: <https://www.eso.org/sci/facilities/paranal/instruments/omegacam/doc/>.

The data were processed with a pipeline specialized for the VST-OmegaCAM observations (dubbed VST-tube; Grado et al. 2012), which performs the following main steps:

- prereduction;
- astrometric and photometric calibration;
- mosaic production.

Science images are first treated to remove the instrumental signatures, applying overscan, bias, and flat-field corrections, as well as gain harmonization of the 32 CCDs, illumination correction and, for the i band, defringing. Relative and absolute astrometric and photometric calibrations are applied before creating the final coadded image mosaics. In Appendix A we describe the various steps of the procedure in detail.

4. NGC 4472 field: photometric processing

4.1. Sky background subtraction

The background estimate and subtraction is the most critical operation in deep photometric analysis because it affects the ability of detecting and measuring the faint outskirts of galaxies.

There are at least two ways to model the sky background. The first one, extensively tested in classical photographic surface photometry (Capaccioli, 1988), consists of fitting a surface, typically a 2D polynomial, to the pixel values of the mosaic that is unaffected by celestial sources or defects. The advantage comes from the simultaneity of the exposure of the galaxy and the background, which is particularly relevant in wide-field images owing to the differential effects of refraction and to the moon light, if any. Minor glitches in the CCDs' sensitivity are averaged as well. The second method mimics the ON-OFF procedure devised in IR astronomy that is made possible by the use of digital detectors. The background is estimated from exposures taken as close as possible, in space and time, to the scientific ones. The

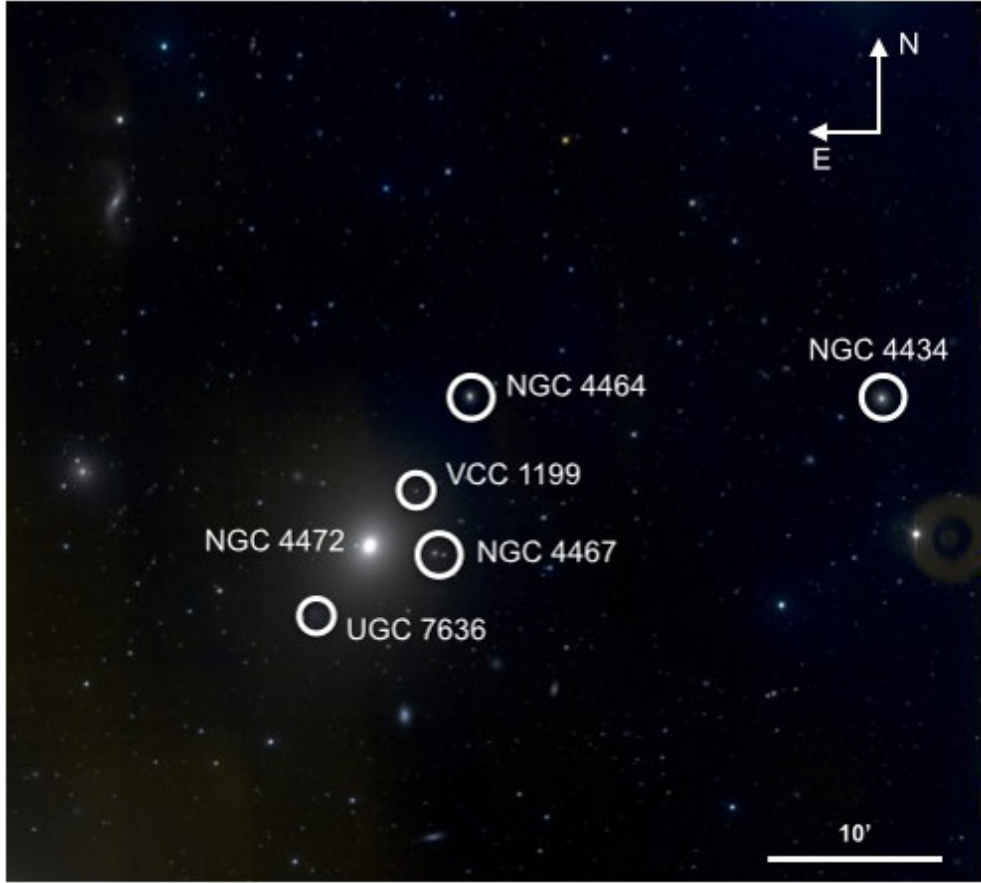


Fig. 2. VST color composite image of the $0.9^\circ \times 0.8^\circ$ field around the giant galaxy NGC 4472 from g and i band VEGAS images. Circles mark the other four ETGs studied in this paper and the interacting system UGC 7636.

main advantage is that the risks in guessing which pixels belong to celestial sources and which to the background are largely reduced, particularly in the target galaxy outskirts. A shortcoming of this strategy, in addition to the already mentioned lack of simultaneity in the galaxy and background exposures, is that it consumes more telescope-time.

In this first paper we have adopted the direct polynomial interpolation procedure described below. The reason is that it is capable of exploring the background for galaxies embedded in the light of more extended sources, as is the case for all the objects of this study except NGC 4472. At the same time, we have tested the procedure on the giant galaxy whose size competes with that of the VST frame.

VST images contain a very large number of sources (stars, galaxies, and image defects). They have to be masked out to define the subset of bona fide background pixels to perform the interpolation. To this end, we used ExAM¹ (Huang et al., 2011), a program based on SExtractor (Bertin & Arnouts, 1996), which was developed to accurately mask background and foreground sources, reflection haloes, and spikes from saturated stars. Very bright stars and galaxies were masked manually. Figure 3 shows a 0.89×0.91 square degrees OmegaCAM g -band image² of

the NGC 4472 field to which the masking procedure has been applied. Masked areas are marked as blank circles.

The most critical step is to optimize the size of the galaxy mask. In principle the problem is very simple. The pixels to be removed from the image are all and only those belonging to the galaxy: *a)* “all” because we wish the residual galaxy halo to avoid causing an overestimate of the background that induces spurious cutoff in the outer light profiles, *b)* “only” because we wish to avoid unnecessarily widening the blank area where the computed surface interpolates the background, which might again induce unreal trends in the faint end of the light distribution. The problem is particularly difficult for ETGs compared to spirals and irregulars because the outermost light distribution smoothly fades.

We solved the problem by creating a set of elliptical masks of increasing sizes centered on the galaxy, with fixed flattening and orientation mimicking the mean behavior of the outer galaxy halo. For each mask we then computed the fifth-order Chebyshev polynomial that best fit the residual source-free image. We then analyzed the median values of the differences between the image and the fitted surface in elliptical annuli around each mask as a function of the mask size to find the smallest mask with vanishing residuals. Clearly this procedure hardly converges when the targeted galaxy fills a significant portion of the OmegaCAM FOV.

This is the case for NGC 4472 (see Fig. 4). Our compromise strategy here assumes that the background level is the median value over the outer annuli of the mosaic. This rough constant estimate is first subtracted from the image and then further im-

¹ ExAM is a code developed by Z. Huang during his PhD. A detailed description of the code can be found in his PhD thesis, available at the following link: <http://www.fedoa.unina.it/id/eprint/8368>

² The reduced size with respect to the nominal VST FOV of one square degree results from a trimming of the low-weight pixels at the rim of the mosaic.

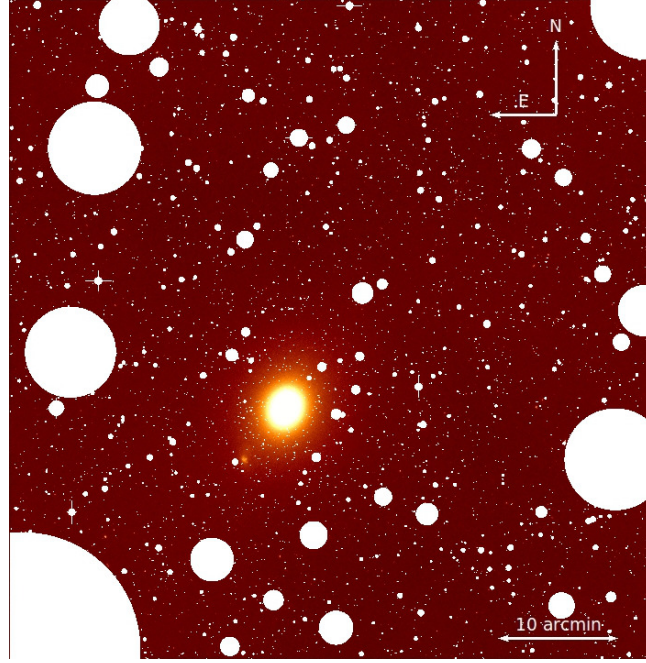


Fig. 3. VST g -band mosaic of NGC 4472 showing the masking of bright sources in the field, done either automatically or manually depending on the brightness of the sources.

proved by randomly picking 5×5 pixel² boxes at the edge of the image and averaging the median counts. By this approach we have estimated a further correction of $\Delta c = -0.3$ ADU over ~ 100 ADU for the g band and $\Delta c = -1.3$ ADU over ~ 600 ADU for the i band.

As a test we assumed that the surface brightness profile of the galaxy (see Sect. 4.3) can be well approximated by an $r^{-1/4}$ law (de Vaucouleurs, 1948), and fitted³ the function $I(a) = I_0 \times 10^{(-3.3307 \times (a/a_e)^{1/4})} + \Delta c'$, where a is the galaxy semi-major axis, to the azimuthal light profiles derived in Sect. 4. The free parameters are I_0 , a_e and $\Delta c'$. It turns out that $\Delta c'$, meaning that the second-order correction of Δc is about zero with an uncertainty of 0.1% in the less favorable case (g band).

Moreover, we applied the methodology described by Pohlen & Trujillo (2006) to quantify the sky variations. As described in the following subsection, we extracted from the sky-subtracted image of NGC 4472 the azimuthally averaged intensity profile out to the edges of the frame by fixing both the position angle and the ellipticity of the galaxy. From this profile (Fig. 5) we estimated a residual background of $\sim 0.3 \pm 0.09$ counts by extrapolating the outer trend. The uncertainty in the extrapolated value is lower than 0.1% of the sky background, which means that it becomes relevant at a level of 29 mag/arcsec². This limit is not intrinsic to VST, but arises from the fact that NGC 4472 practically fills the field of view of the camera. In Fig. 6 we show a false-color image of the NGC 4472 field (left) together with its 2D residuals (right) obtained by subtracting the galaxy model described in Sect. 5.1.2. The white circles mask the areas ignored in the isophotal fitting. The bluish foggy patch in the middle of the right side in both images is due to the malfunctioning of CCD

82 of OmegaCam (a problem now solved by the replacement of the board).

In conclusion, we stress that the background-subtraction procedure for the OmegaCAM images is sometimes made quite difficult by the residual unevennesses left in the mosaic by the combination of the 32 independent CCDs. For this reason, we will evaluate the ON-OFF background-subtraction procedure in another paper.

4.2. Isophotal analysis

The isophotal analysis of the VEGAS galaxies is performed on the final mosaic in each band with the IRAF⁴ task ELLIPSE. Briefly, ELLIPSE computes the intensity, $I(a, \theta)$, azimuthally sampled along an elliptical path described by an initial guess for the isophote center, (X, Y) , ellipticity, ϵ , and semi-major axis position angle, θ , at different semi-major axis lengths, a . At a given a_0 , $I(a_0, \theta)$ is expanded into a Fourier series as

$$I(a_0, \theta) = I_0 + \sum_k (a_k \sin(k\theta) + b_k \cos(k\theta)) \quad (1)$$

according to Jedrzejewski (1987). The best-fit parameters are those minimizing the residuals between the actual and the model isophotes; a_k and b_k are the coefficients measuring the deviations from a pure ellipse, including the signature of boxiness and/or diskiness (Bender et al., 1989).

4.3. Light and color distribution

Together with the geometrical parameters, the task ELLIPSE provides the light distribution azimuthally averaged either over each isophote or within isophotal annuli of specified thickness.

³ We used MINUIT (James & Roos, 1975), which is a program written by staff of CERN (European Organization for Nuclear Research). It searches for minima in a user-defined function with respect to one or more parameters using several different methods as specified by the user.

⁴ IRAF (*Image Reduction and Analysis Facility*) is distributed by the National Optical Astronomy Observatories, which is operated by the Associated Universities for Research in Astronomy, Inc. under cooperative agreement with the National Science Foundation.

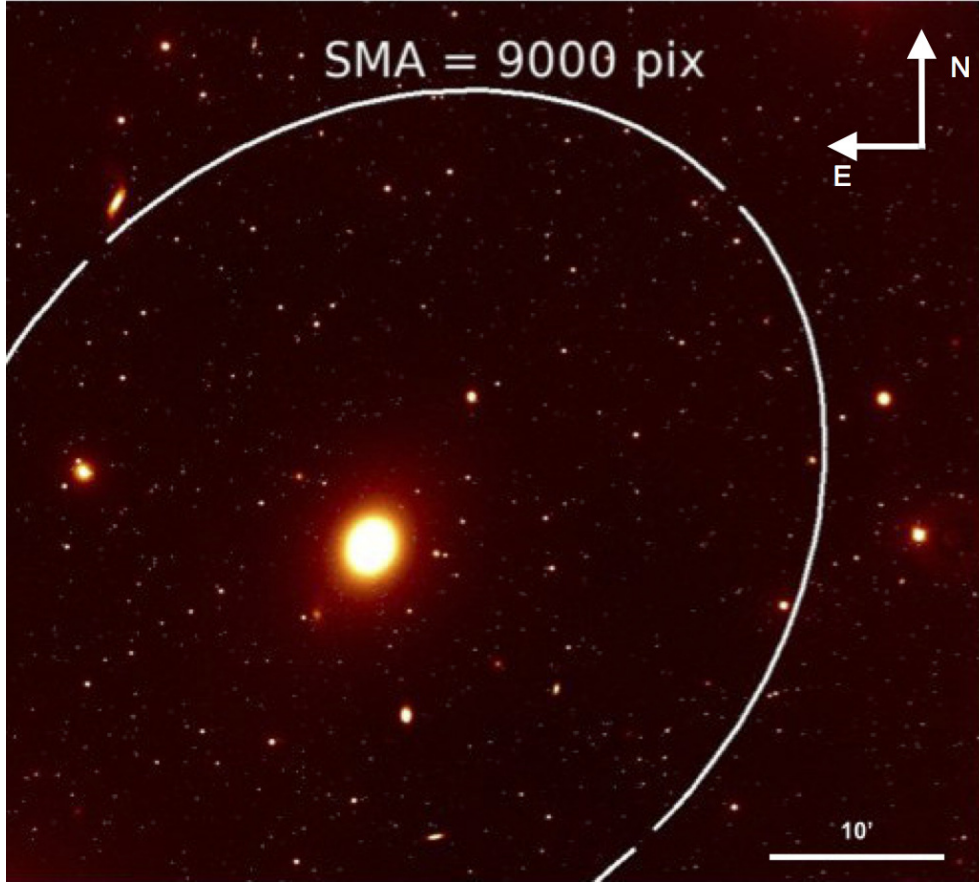


Fig. 4. VST g -band mosaic of NGC 4472. The isophotal contour (in white) represents the last isophote fitted to obtain the surface brightness profile. The image size is $0.9^\circ \times 0.8^\circ$.

The error associated with the surface brightness measurements was computed with the formula

$$\sigma_\mu = \sqrt{\left(\frac{2.5}{I \ln 10}\right)^2 (\sigma_I + \sigma_{sky})^2 + \sigma_{ZP}^2}, \quad (2)$$

where the flux I and the errors σ for the flux I , the sky, and the photometric ZP, and the resulting σ_μ are in counts. We assumed simple Poissonian behavior, therefore $\sigma_I = \sqrt{I/n}$, where n is the number of pixels producing the median value I . The errors on the background are those discussed in Sect. 4.1, while those on the ZP are listed in Table A.1.

The resulting light profiles are presented and discussed in the next section, and the tables with the corresponding data for each galaxy are published in the online version of this journal. Here we comment on the resolution of the innermost and the reliability of the outermost measurements. Although our data have a good overall resolution, as shown by the FWHM values of the PSF (see Tab.2), we did not attempt any deconvolution to improve the resolution since our galaxies have previously been observed by *HST*. The direct comparison with *HST* profiles (Kormendy et al. 2009; see next section) shows our profiles to be unaffected by seeing for $r > 2$ arcsec in the g band; this limit is also valid for the i band. When we present the light profiles below, we also show and quote the seeing-blurred innermost measurements, but they will not be used for fitting the data with empirical photometric laws.

The faintest end of the luminosity profiles has large errors. They do not reach the same threshold value in all cases because

of the different nature of the background to be subtracted combined with the size of the object (the smaller the better).

5. Individual galaxies: results and comparisons

In this section we present and discuss the results for the objects of this study and compare them with the available literature. Tables with the photometric and geometric profiles are available online; for the sake of clarity, we repeat that these data are not corrected for interstellar extinction. The effective parameters and the total magnitudes are listed in Table 3, while Table 4 provides the effective parameters of the $r^{1/4}$ models that best fit our profiles outside of the seeing-convolved cores.

The effects of the scattered light are illustrated for NGC 4472 in Appendix B. At the end of this section, we list the effects for the smaller companions.

5.1. NGC 4472

Figure 7 shows the results of the isophotal analysis performed by ELLIPSE. Some comments are in order.

The profiles in the two bands are substantially similar out to $a \sim 15'$ or $(a/a_e)_g \sim 4.83$, where a_e is the effective semi-major axis. The rapid change in the inner region is due to the well-known peculiarity of the nucleus of NGC 4472. Ferrarese et al. (2006) in fact detected a “boomerang-shaped” dust lane crossing the central regions of the galaxy. Beyond $a^{1/4} \simeq 4$ arcsec both the ellipticity and the position angle profiles diverge in the two bands: the g isophotes flatten outward, while in the i band

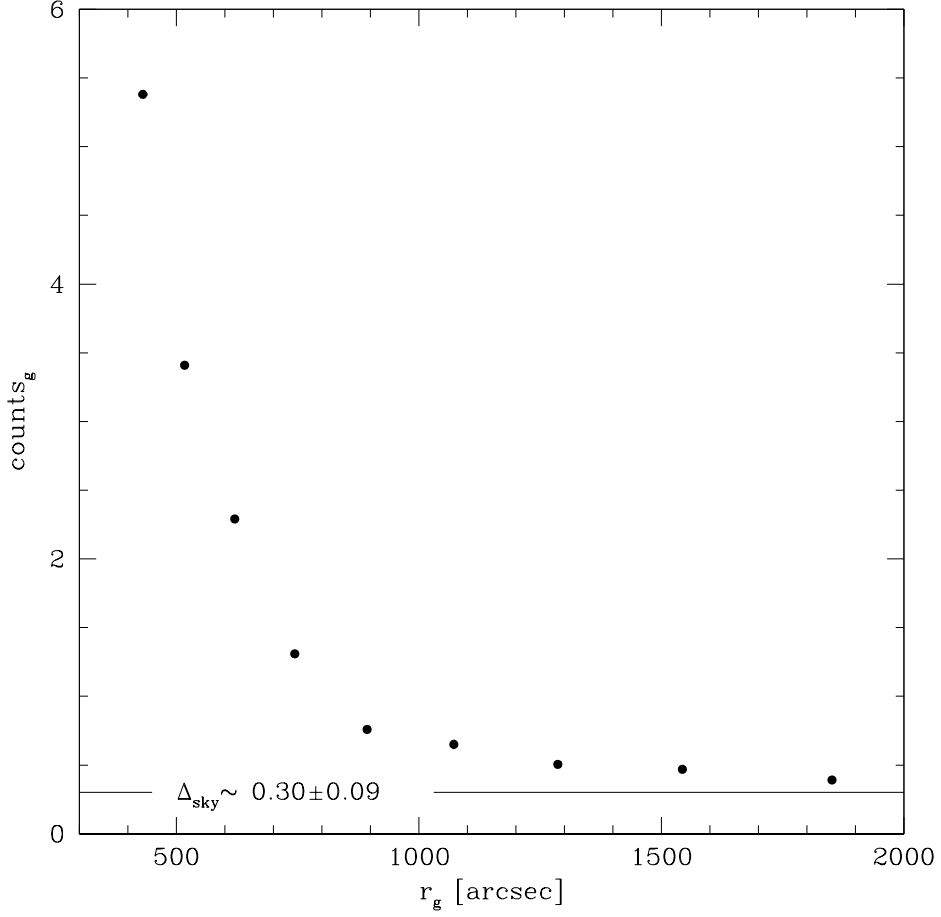


Fig. 5. Azimuthally averaged intensity profile of NGC 4472 as a function of the semi-major axis. The horizontal line indicates the residual background counts of $\Delta_{\text{sky}} \sim 0.3$.

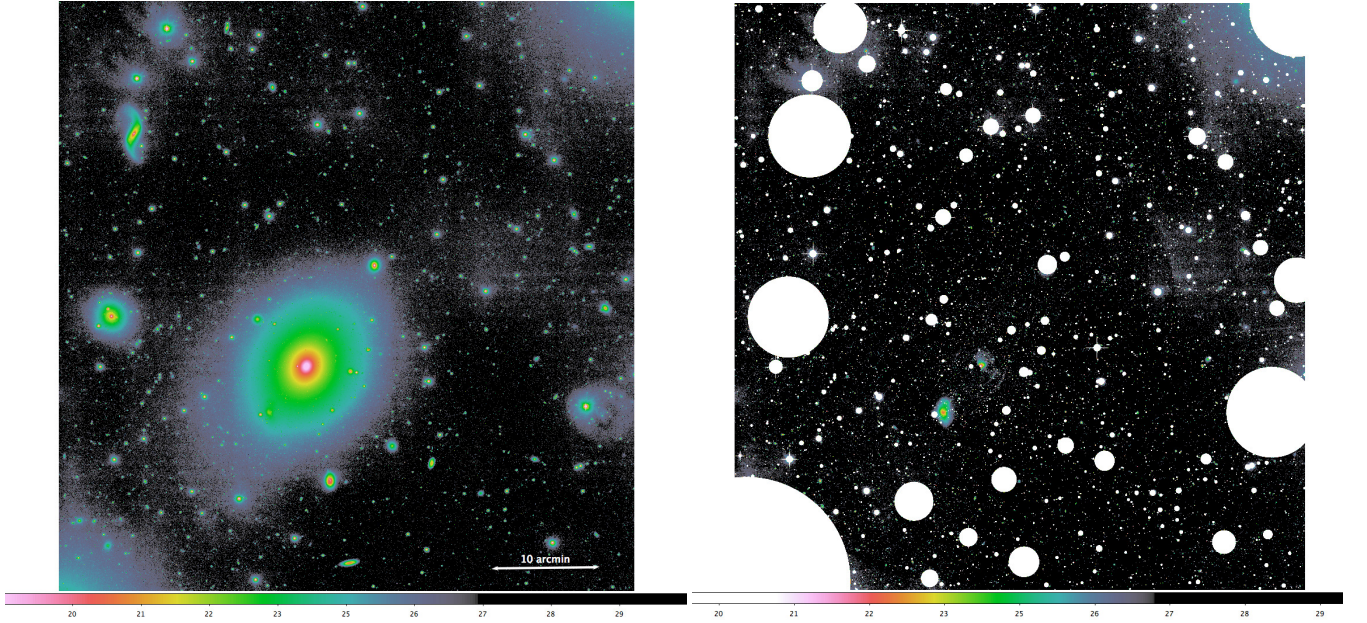


Fig. 6. *Left:* False-color image of the VST pointing of NGC 4472, trimmed to the same size as that in Fig. 4. The magnitude scale adopted to produce the picture is shown at the bottom. The last clearly visible isophote is at $\mu_g \sim 27 \text{ mag/arcsec}^2$. *Right:* Residual image obtained by subtracting from the left picture the galaxy model described in Sect. 5.1.2. Masks adopted to exclude features from the fitting are shown as circles.

Table 3. Magnitudes and effective parameters.

Name	Band	$a_L^{1/4}$ [arcsec ^{1/4}]	m_L [mag]	Δm [mag]	m_T [mag]	$a_e^{1/4}$ [arcsec ^{1/4}]	μ_e [mag]	$\langle \epsilon \rangle$	$r_e^{1/4}$ [arcsec ^{1/4}]	$(\mu_e)_V$ [mag]	$(r_e^{1/4})_V$ [arcsec ^{1/4}]
(1)	(2)	(3)	(4)	(5)	(6)	(7)	(8)	(9)	(10)	(11)	(12)
NGC 4472	<i>g</i>	5.47	8.55	0.05 ^a	8.50	3.49	22.59	0.16	3.42	22.73	3.73
NGC 4472	<i>g</i>	6.56	8.48	0.11 ^b	8.37	3.71	23.03	0.19	3.61		
NGC 4472	<i>g</i>	6.56	8.37	0.10 ^c	8.27	3.86	23.31	0.16	3.78		
NGC 4472	<i>i</i>	6.47	7.19	0.23 ^d	6.96	3.99	22.27	0.18	3.89		
NGC 4472	<i>i</i>	6.56	7.10	0.10 ^e	7.00	3.90	22.09	0.16	3.82		
NGC 4434	<i>g</i>	2.89	12.52	0.60	12.46	1.83	21.08	0.05	1.82	20.08	1.83
NGC 4434	<i>i</i>	2.89	11.45	0.50	11.40	1.83	19.81	0.05	1.82		
NGC 4464	<i>g</i>	2.76	13.04	0.40	13.00	1.67	20.43	0.27	1.61	19.92	1.66
NGC 4464	<i>i</i>	2.76	11.84	0.20	11.82	1.67	19.05	0.27	1.61		
NGC 4467	<i>g</i>	2.33	14.63	0.40	14.59	1.57	21.31	0.22	1.52	20.91	1.56
NGC 4467	<i>i</i>	2.33	13.50	0.20	13.48	1.55	20.03	0.23	1.50		
VCC 1199	<i>g</i>	2.02	15.92	0.10	15.94	1.25	20.81	0.11	1.23	20.28	1.22
VCC 1199	<i>i</i>	2.02	14.71	0.10	14.70	1.25	19.57	0.12	1.23		
UGC 7636	<i>g</i>	3.41	14.22	0.07	14.15	2.62	24.91	0.39	1.41		
UGC 7636	<i>i</i>	3.41	13.38	0.53	12.85	3.13	21.26	0.39	2.95		

Notes. Column 3: Major axis of the faintest isophote for which SB is measured. Column 4: Magnitude within a_L , computed assuming a fixed mean ellipticity $\langle \epsilon \rangle$ (Col. 7). Column 5: Extrapolation of the growth curve to infinity. Column 6: Total magnitude $m_T = m_L + \Delta m$. This value is not corrected for interstellar extinction. According to Arrigoni Battaia et al. (2012), the correction would be $A_g = 0.074$ and $A_i = 0.044$ mag. Column 7: Major axis of the effective isophote of flattening $\langle \epsilon \rangle$ that encircles half of the total light. Column 8: SB at the effective semi-major axis a_e . Column 9: Adopted mean ellipticity. Column 10: Mean effective radius $r_e = a_e \sqrt{1 - \langle \epsilon \rangle}$. Columns 11 and 12: Effective parameters for the V band (Kormendy et al., 2009).

Notes. ^(a) Excluding the ICL tail. ^(b) Including the ICL tail. ^(c) Including the ICL tail, but flattening the ellipticity profile from 1.75 arcmin on. ^(d) With measured ellipticity. ^(e) With ellipticity modified as for the *g* band (note c).

Table 4. Effective parameters of the $r^{1/4}$ models that best fit our light profiles outside the seeing-blurred cores.

Galaxy	<i>g</i> band $r_e^{1/4}$ [arcsec ^{1/4}]	<i>g</i> band μ_e [mag/arcsec ²]	<i>i</i> band $r_e^{1/4}$ [arcsec ^{1/4}]	<i>i</i> band μ_e [mag/arcsec ²]
NGC 4472	3.51	22.52	3.51	21.25
NGC 4434	1.85	21.13	1.75	19.64
NGC 4464	1.59	20.16	1.50	18.48
NGC 4467	1.33	20.18	1.30	18.86
VCC 1199	1.00	18.73	0.97	17.11

they have a rounded shape. The deviations are far larger than the formal errors provided by ELLIPSE. Nonetheless, we doubt that this behavior is spurious; it may be due to the excessively large size of the supergiant elliptical that almost fills the OMEGACam FOV. A comparison with Kormendy et al. (2009) suggests that the diverging *g*-band flattening profile might not be real. We return to this point below.

The shape parameters in both the *g* and *i* bands (Fig. 7) show a moderate boxiness of the isophotes, which confirms the presence of dust in the central regions of the galaxy. Since the dust optical depth decreases toward longer wavelengths, the *i*-band profiles are less affected by dust.

The azimuthally averaged light profiles in the *g* and *i* bands are shown in Fig. 8 as a function of the isophote semi-major axis a . The average surface brightness extends out to $a \simeq 30.6$ arcmin from the galaxy center for the *g* band, with the largest formal errors of about 0.3 mag, while in the *i* band we reach ~ 17.6 arcmin with errors four times larger.

The effect produced by the extended PSF onto the image of NGC 4472, and therefore onto its azimuthally averaged light profile, was estimated by the methods outlined in Appendix B.

The result is that no significant contribution is present in the light distribution out to the faintest measured point. This conclusion is particularly important because it verifies that the observed bending in the light profile occurs at $\mu_g \sim 27$ mag/arcsec². This cannot be due to scattered light.

The surface brightness profiles in both the *g* and *i* band are fairly linear in $r^{1/4}$ units except at the center. When forcing a de Vaucouleurs (1948) law (de Vaucouleurs, 1948) over the range $1''$ to $625''$, the best-fit parameters are $r_e = 152'' \pm 6''$ and $\mu_e = (22.52 \pm 0.05)$ mag/arcsec² in *g* band and $r_e = 152'' \pm 7''$ and $\mu_e = (21.25 \pm 0.05)$ mag/arcsec² in *i* band (see also Table 4). Interestingly enough, the effective radii are exactly the same, with the same error in both bands. The color at r_e is $(g - i) = 1.27 \pm 0.07$.

The $r^{1/4}$ fit highlights a neat change in the slope of the *g*-band light profile at $a_e^{1/4} \simeq 5.5$, where $\mu_g \sim 27$ mag arcsec⁻². Is this bending, just outlined by the less extended *i*-profile and by the B-band major axis profile of Caon et al. (1994), a signature of intracluster light (ICL)? To determine whether it might be an artifact of the turn-up of the flattening of the outer isophotes (see Sect. 4.2), we simulated an $r^{1/4}$ galaxy using the *g*-band inter-

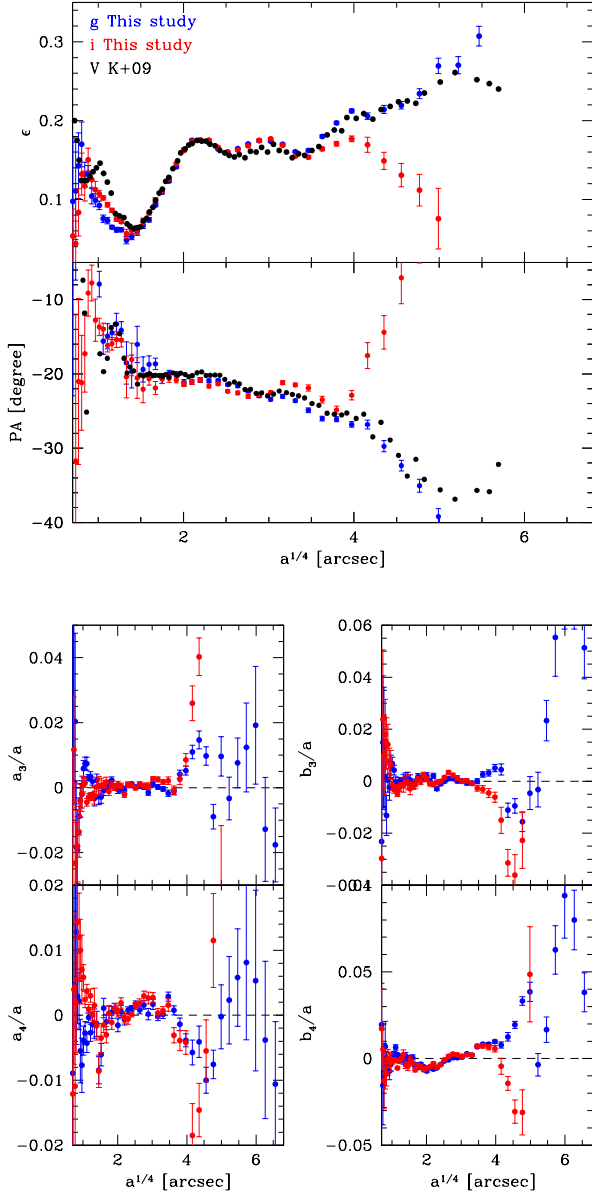


Fig. 7. NGC 4472. Top: position angle (P.A.) and ellipticity (ϵ) profiles in the *g* and *i* bands compared with those in K+09. Bottom: isophotal shape parameters in the *g* and *i* bands.

polarization parameters of NGC 4472 for two isophotal geometries: a fixed ellipticity $\epsilon = 0.25$, which in the second case increases linearly from $a_e = 750''$ and mimicks the *g*-band ellipticity profile of Fig. 7. The outer light profile of the second case remains brighter where the ellipticity increases, but the effect is quantitatively negligible compared to what we observe. Moreover, we note that as suggested by Gonzalez et al. (2005), the presence of an outer and more elliptical component with a significant gradient in the P.A. is most likely due to a population of some ICL.

There is another possibility of how a spurious change of slope in the SB profile might be produced: an incorrect setting of a background level. However, this is not the case here because a too faint value for the background would produce a smooth change in the slope instead of a sharp break. Finally, we note that the level at which the break occurs is compatible with the typical SB values at which Zibetti et al. (2005) have observed

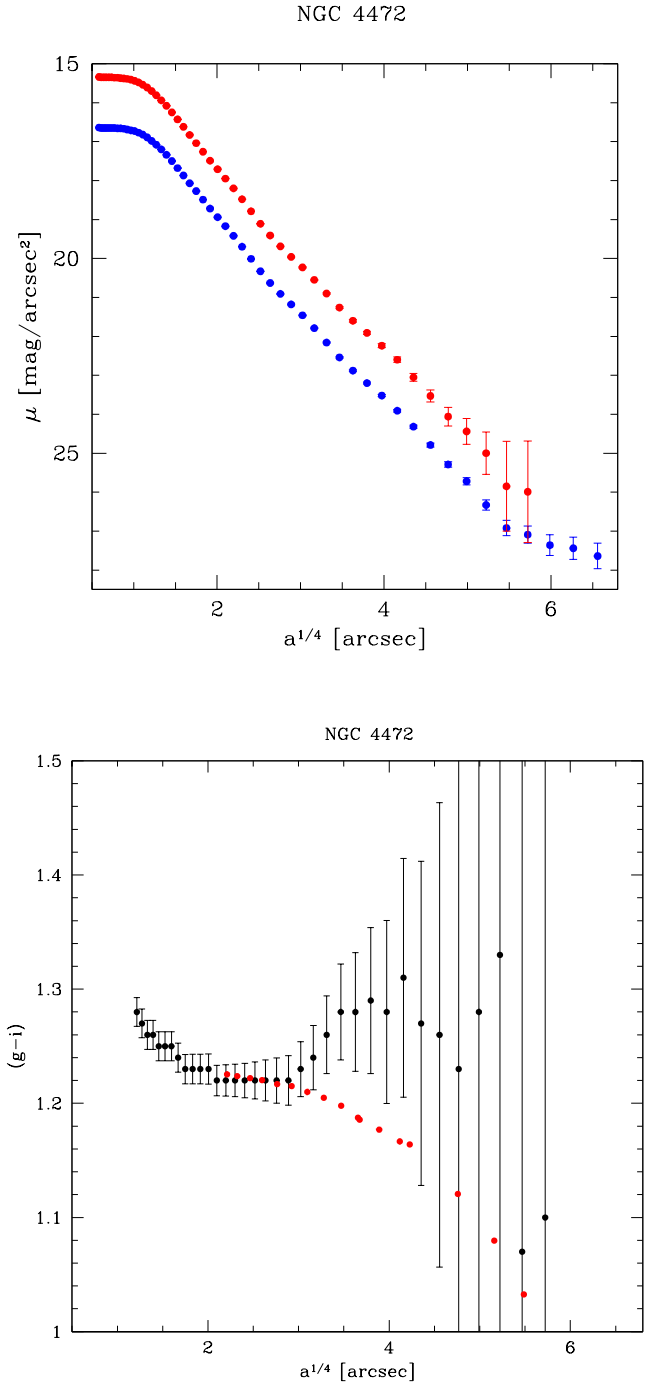


Fig. 8. NGC 4472. Top: azimuthally averaged light profiles in the *g* (blue) and *i* (red) bands. Bottom: $(g-i)$ color profile in the region ($a > 2$ arcsec) unaffected by differential seeing. The red dots trace the $(B-V)$ profile published by Mihos et al. (2013) shifted by +0.25 mag, measured in the regions of high S/N for both datasets. The comparison supports the blueward gradient that we found for $a/a_e > 4$, although with very large errors.

changes of slope induced by the ICL in a series of stacked galaxy clusters.

Our azimuthally averaged *g*-band profile is compared with results from the available literature in Fig. 9. The offsets providing the best match to our photometry are -0.35 mag for the *B*-band profile of Mihos et al. (2013), +0.35 for the *V* photome-

try of Kormendy et al. (2009) and Janowiecki et al. (2010), and $+0.92$ for the R -like band of Kim et al. (2000). Caon et al. (1994) have not been considered here because these authors provided main axes and no azimuthal profiles. In spite of the different color bands, the agreement among the various profiles is good from outside the seeing-blurred core to $\mu_g \sim 27 \text{ mag arcsec}^2$. Janowiecki et al. (2010), whose data extend far enough out, did not confirm the ICL tail exhibited by our profile.

There is instead a problem in the zero points of the various photometric analyses of NGC 4472. In particular, by adding the offsets to the B band (Mihos et al., 2013) and the V band (Kormendy et al., 2009), we obtain a $\langle(B-V)\rangle = 0.70$, which is largely inconsistent with the known average color of NGC 4472 (e.g., $\langle(B-V)\rangle = 0.96$ from RC3 (de Vaucouleurs et al., 1991)). Comparison with the stellar population synthesis models by Bruzual & Charlot (2003) with standard assumptions⁵ provide $\langle(B-g)_{BC}\rangle = 0.49$ and $\langle(g-V)_{BC}\rangle = 0.48$, which turn into zero-point residuals of $\Delta\langle(B-g)_{BC}\rangle = 0.14$ and $\Delta\langle(g-V)_{BC}\rangle = -0.13$, which might be the zero-point shifts in both Mihos et al. (2013) and Kormendy et al. (2009). The very small error estimated for our photometry by the comparison with 2MASS (see Appendix A.6) is confirmed by the comparison of our photometry of NGC 4472 with that of Ferrarese et al. (private communication) which in the range from 18 to 26 mag/arcsec^2 provides an average value of $\Delta\mu_g = 0.002 \pm 0.016$.

A clearer way to compare these different data is to plot their residuals with respect to $r^{1/4}$ fits all with the same slope (Fig. 9). The agreement is spectacular: the scatter is better than the formal error computed for our photometry for all μ_g brighter than $\sim 27 \text{ mag arcsec}^2$. Thereafter, the scatter increases significantly with no apparent dependence on the color band. In the same figure we have plotted as a solid line the residuals for the East-West photometric cross-section of the standard elliptical galaxy NGC3379 from de Vaucouleurs & Capaccioli (1979), scaled in such a way that the effective surface brightness of the two galaxies coincides. We note in NGC 4472 the same inner core as was discovered in NGC 3379 by de Vaucouleurs & Capaccioli (1979) and the occurrence of a wavy pattern of the residuals of similar amplitude, which calls for an explanation. A recent study of the M96 galaxy group (Watkins et al., 2014) has revealed faint shells around NGC 3379 and a dusty disk in the inner regions. The observed trend in the observed minus calculated (O-C) residuals seems to be typical for galaxies with such substructures. We intend to verify with VEGAS whether this behavior is a common feature for ETGs.

The bottom panel of Fig. 8 plots the mean $(g-i)$ color profile for NGC 4472, obtained from the two azimuthally averaged luminosity profiles above. Data points affected by differential seeing ($a < 2 \text{ arcsec}$) were removed. On average, the center of the galaxy has a redder color, with a maximum value up to $(g-i) \sim (1.3 \pm 0.18) \text{ mag}$. Our $(g-i)$ color profile is fully consistent with that published by Chen et al. (2010), which only extends up to $a^{1/4} \sim 2.8$ or $a/a_e \sim 1$, however. The color stays bluer in the range $5'' \leq a \leq 150''$ ($1.5 \leq a^{1/4} \leq 3.5$), then it turns redder again, and the gradient is almost flat, although the errors here are too large to robustly assess whether there are color gradients outside this radial range. However, a comparison with the $(B-V)$ color profile published by Mihos et al. (2013) (red dots in Fig. 8, plotted with a shift $\Delta(B-V) = 0.25$, measured in the regions of high S/N for both datasets) seems to confirm the steep blueward

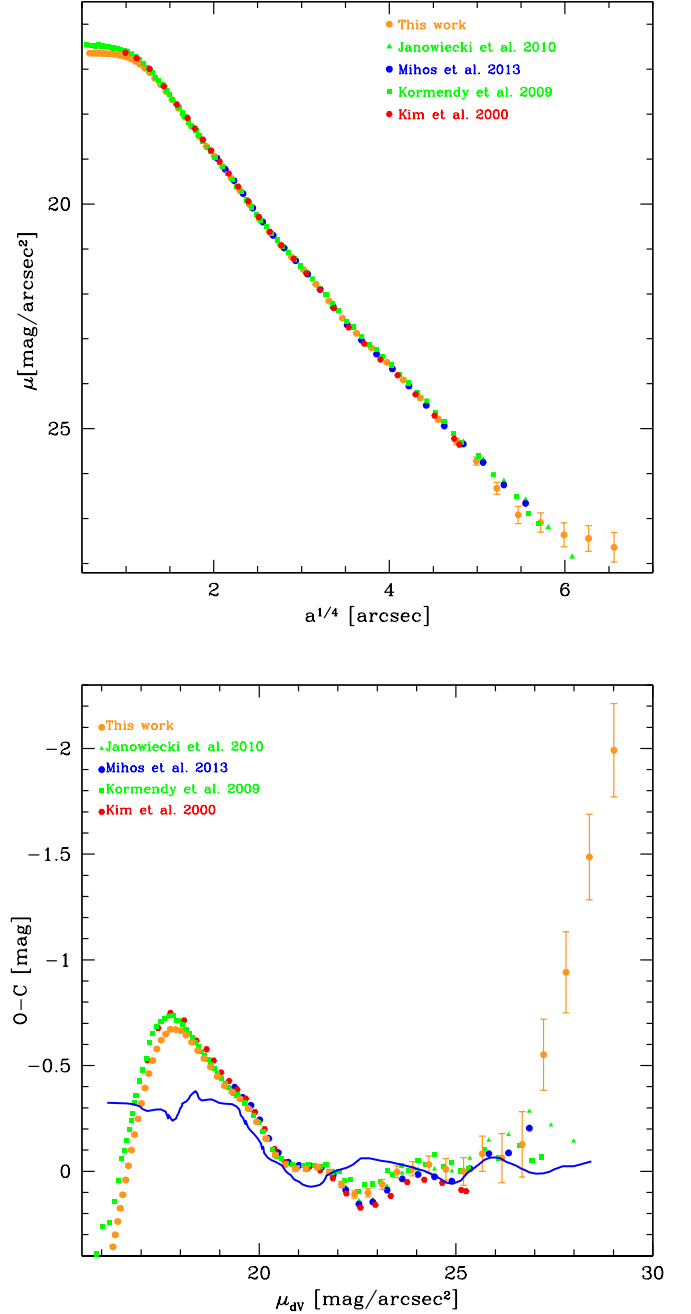


Fig. 9. NGC 4472. *Top panel:* Azimuthally averaged g-band profile from VEGAS compared to literature. The color code of the symbols mimicks the corresponding photometric bands. Arbitrary shifts have been used to match with the VEGAS profile. In particular, the B-band profile by Mihos et al. (2013) has been shifted by -0.35 mag , the V band by Mihos et al. (2009) and Janowiecki et al. (2010) by $+0.35 \text{ mag}$, and the profile by Kim et al. (2000) by $+0.92 \text{ mag}$. *Bottom panel:* (O-C) residuals of mean profiles from a best-fitting $r^{1/4}$ model used only to remove the main gradient and facilitate comparison. The blue solid line plots the (O-C) residuals for the east-west photometric cross-section of the standard elliptical galaxy NGC3379 from de Vaucouleurs & Capaccioli (1979). There are clear similarities: the bright core and a wavy trend overimposed on the smooth $r^{1/4}$ trend.

⁵ We adopted a star formation history with an exponentially decreasing rate, as is typically used for ETGs in the local Universe, with a Salpeter IMF in a metallicity range between Z_{\odot} and $2.5Z_{\odot}$.

gradient in the galaxy outskirts, from approximately $a \sim 10'$ or $a/a_e > 4$.

5.1.1. Total magnitudes

Total magnitudes require a careful examination of the trends of the light profiles as well as a critical analysis of the geometry of the isophotes. Direct integration over all pixels encircled by a given outermost isophote is out of consideration because it is difficult to interpolate the light profile around contaminating sources (satellite galaxies, GCs, background galaxies, foreground stars, etc.). The procedure we adopted consists of summing the areas encircled between successive isophotes multiplied by an average flux value. These growth curves, built using the azimuthally averaged light profiles and the flattening profiles under the assumption of elliptical isophotes, are then plotted against the reciprocal of the outer semi-major axis $1/a$ of the various elliptical annuli to estimate the extrapolation to $1/a \rightarrow 0$. There is no need to correct for resolution since the convolution with the PSF preserves the energy. In contrast, much care must be placed 1) in judging the meaning of the ellipticity measurements at faint levels because they may significantly affect the result, and 2) in the method of extrapolating a signal there where the trend of the light profile is totally unknown. Errors in the total magnitude reflect onto the estimates of the effective radius, which is thus a rather poorly defined parameter. It can be shown that for an $r^{1/4}$ galaxy, an error Δm in the extrapolation turns into a relative error $\Delta r_e/r_e = 1.84\Delta m$.

The case of NGC 4472 is particularly complex for two reasons: 1) it shows a stretched tail in the outermost g -band profile, which is interpreted as intracluster light that may be cut off in computing the total luminosity of the galaxy, and 2) the trend of the flattening with radius for $a > 150$ arcsec, which is just opposite in the two bands (see Fig. 7) and poses the question of whether this is real or if the truth is in between these two curves. The difference is non-negligible. Table 3 reports the total magnitude in the g and i bands, computed using the nominal ellipticity curves shown in Fig. 7. The integration is performed out to the last observed point at a_L . The extrapolation term Δm was estimated assuming an $r^{1/4}$ extension mimicking the behavior of the main body of the galaxy, that is, cutting out the ICL tail. The exercise was repeated including ICL, but in this case, the extrapolation is large and indeed uncertain. It is very difficult to set a reliable figure for the error on m_T . The overall uncertainty in the light profile combines with those on the isophotal shape and on the extrapolation to give an uncertainty of at least 0.1 mag. In any case, it seems that ICL contributes some 15% of the total g -band light of NGC 4472.

The effective semi-major axes were derived by the growth curves at 50% of the total luminosity given by m_T , while the corresponding surface brightness was interpolated at a_e in the light profiles.

5.1.2. Substructures of NGC 4472

To examine the inner structure of NGC 4472 and detect the high-frequency structures, we first smoothed the images in the two bands with the IRAF task FMEDIAN, which takes a median in a 2D window of 150×150 pixels in i band and of 300×300 pixels in g band. These sizes were chosen by trial and error to best emphasize the inner structure of the galaxy. Each image was then divided by its smoothed version to remove the low-frequency components. The final unsharp masked images are shown in Fig.

10. They both show an X-shaped pattern in the inner regions that most likely is the signature of boxy isophotes, as pointed out in Sect. 4.2. Boxy isophotes are indicative of an interaction or a mass transfer from a passive satellite (Binney & Petrou 1985; Whitmore & Bell 1988) and of the presence of dust.

To highlight possible larger substructures, we produced a 2D model of NGC 4472 that best fit the azimuthally averaged isophotes with the IRAF task BMODEL. Only the g -band image was considered here because of its higher S/N ratio. The image and its model are shown in Fig. 11, while Fig. 12 shows the difference between them. This residual map shows a clear asymmetry in the nuclear region and some diffuse features, such as a tail associated with the dwarf irregular galaxy UGC 7636 interacting with NGC 4472 and concentric shells and fans of material (white contours) that were also identified photometrically by Janowiecki et al. (2010) and Arrigoni Battaia et al. (2012) and by D'Abrusco et al. (2015) using globular clusters. The outer boundaries of these shells and substructures mimic the pattern of the minima in the O-C residuals of the azimuthal light profile with respect to a smooth $r^{1/4}$ interpolation, shown in the bottom panel of Fig. 9.

The 2D modeling above assumed the isophotes to be homocentric and elliptical. To relax these requirements and search for asymmetric features, we rotated the original g -band image around the galaxy center by 180° and then subtracted the image itself. The result is shown in Fig. 13. In this way, we discovered the possible presence of a long tail connecting UGC 7636 to NGC 4472, twisted around the nucleus. The brightest part of this tail associated with UGC 7636 is also visible in the residual map of Fig. 12. The tail is not shown in the BMODEL subtraction residual image, but this method is probably less sensitive to local very low surface brightness features.

5.2. NGC 4434

NGC 4434 (also known as VCC 1025) is an E0 galaxy where F+06 highlighted the large nucleus, derived from a “break” in the surface brightness profiles around $1''$.

The ellipticity and P.A. profiles in Fig. 14 show strong variations within the first $20''$, which are not mirrored in the shape parameters (a and b high-order coefficients), which look very regular and featureless in the central $20''$, making this galaxy a quite perfect E0 system (there is a peak of 0.1 in the ellipticity at $a \sim 6''$ while $\epsilon < 0.05$ everywhere). However, the shape parameters start to show strong variation outside, which are difficult to comment on because of the large errors.

Figure 15 reproduces the azimuthal SB profile in g and i bands. Even deeper than for NGC 4472, reaching ~ 28 mag/arcsec² in g band and ~ 27 mag/arcsec² in i band at $a/a_e \sim 10$, they appear regular and very similar, and both show a bump in the profiles at $a/a_e \sim 2.5$. This feature is evident as an excess of the residuals with respect to the best-fitting de Vaucouleurs profiles (Table 4), which are again overplotted on the SB profiles and are better highlighted by the (O-C) curves (central panel of Fig. 15).

The ($g-i$) color distribution (bottom panel of the same figure) is fairly constant out to $40''$ ($a^{1/4} \sim 2.5''$ and $a/a_e \sim 3.6$), while it decreases steeply immediately after the bump in the light profile. One might be tempted to blame an improper background subtraction as responsible for the effect, since the galaxy lies at the edge of the OmegaCAM field. However, the change in the slope of the i -band profile with respect to the g profile occurs at a surface brightness level where the photometric error is typi-

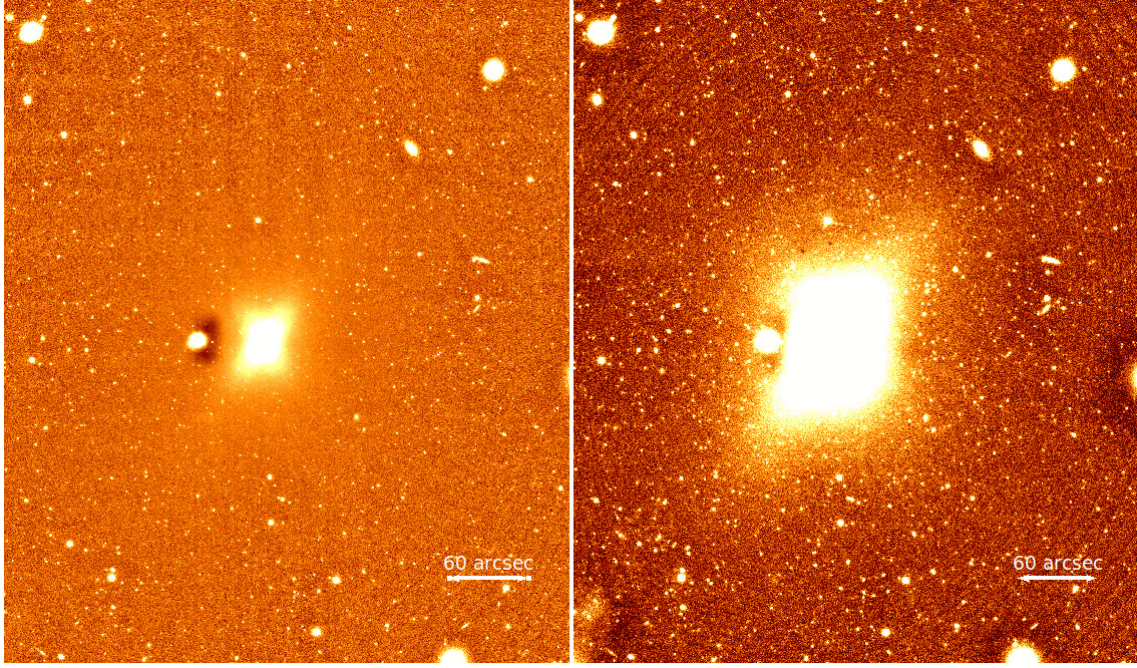


Fig. 10. NGC 4472. Unsharp masked image, extracted from the whole VST mosaic (500×600 arcsec) in the i (left panel) and g band (right panel). Lighter colors correspond to brighter features.

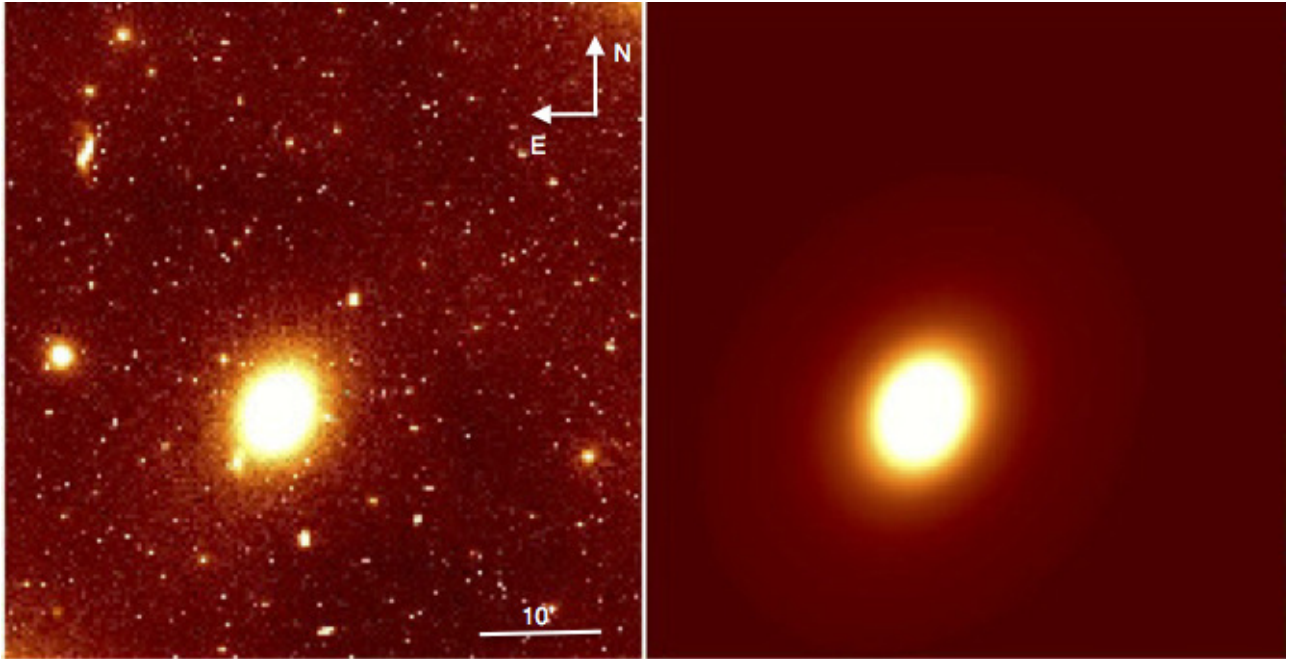


Fig. 11. NGC 4472. Left panel: A region of 55×56 arcmin of the VST g band mosaic. Right panel: 2D model (see text).

cally small. Moreover, just the same pattern is shown by another two galaxies of our sample (Sect. 7).

The bump shows up lighter in the K+09 photometry, over-plotted on our g band profile in Fig. 15 using the same color term as applied to NGC 4472. Here we also see that our profile deviates from that of *HST* in the very central regions ($r < 1''$) as a result of the seeing broadening, while it remains consistent within the errors with K+09 at all the other radii.

Total luminosity and effective parameters are estimated as for NGC 4472 (Sect. 5.1.1) and listed in Table 3.

5.3. NGC 4464

NGC 4464 (VCC 1178) is an E3 system. Figure 17 shows the azimuthal SB profiles reaching ~ 30 mag/arcsec² in g band and ~ 29 mag/arcsec² in i band at about $100''$ ($a/a_e \sim 12.8$). In this case as well, the color distribution outside $1''$ is very flat over a wide radial range: $(g - i) \sim 1.2$ for $a/a_e < 3$. Outside, the color profile bends toward a minimum in correspondence of a rapid variation of the ellipticity, P.A., and shape parameters (Fig. 16). In particular, a_4 indicates “disky” isophotes both in g and i bands, although outside $a \sim 20''$, the shape parameters are again rather noisy.

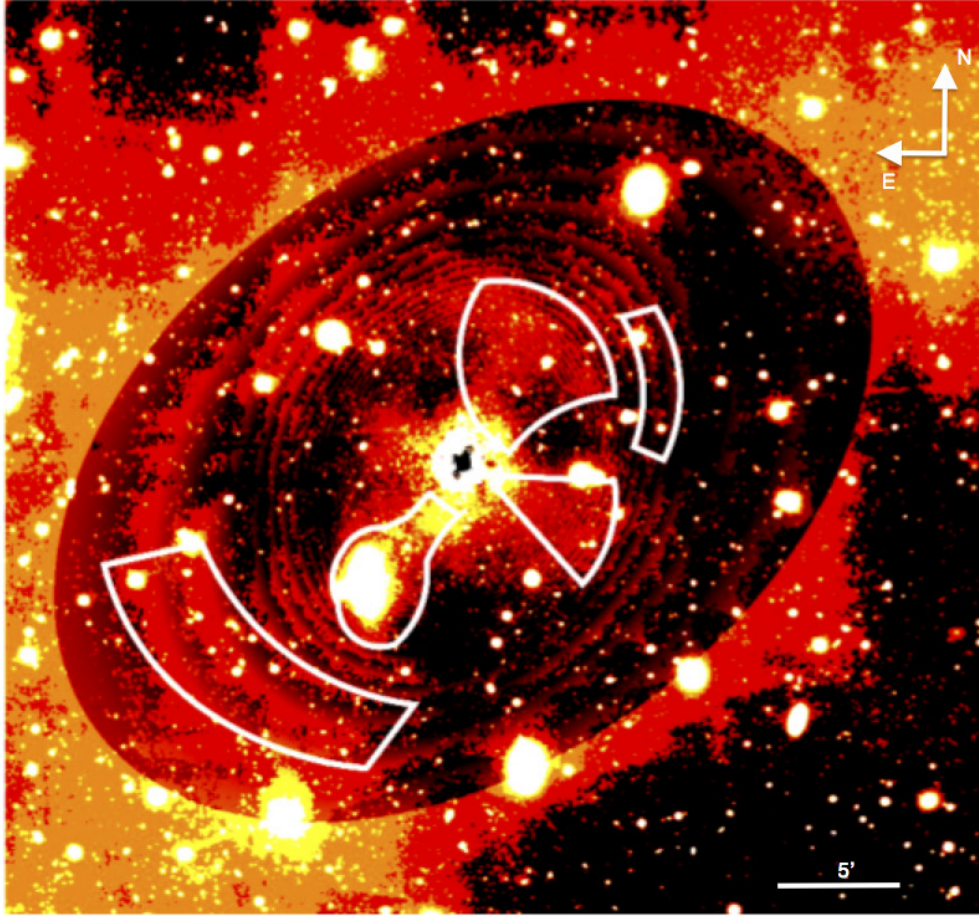


Fig. 12. NGC 4472. Zoom (37×35 arcmin) of the median-smoothed residual image. The outermost elliptical contour marks the region where the b-model subtraction was not applied. The superimposed white contours are 1) the tail connecting UGC 7636 to the giant ETG, and 2) shells and fan of material identified by Janowiecki et al. (2010) and Arrigoni Battaia et al. (2012) that is visible in our residual image. The wave-like residuals, concentric with the NGC 4472 nucleus, are spuriously introduced by the numerical procedure.

Table 5. Average colors computed as shifts giving the best match of the inner light profiles.

Name	(g-V) [mag]	(g-i) [mag]
NGC 4472	+0.35	+1.24
NGC 4434	+0.20	+1.10
NGC 4464	+0.39	+1.23
NGC 4467	+0.29	+1.16
VCC 1199	+0.20	+1.24

The SB profiles in both bands also show for this galaxy some hints of a substructure as light excess with respect to the $r^{1/4}$ fit (Table 4) shown in Fig. 17 (in this case around $a/a_e \sim 1.7$; see the (O-C) profile).

The multiple components along the line of sight have previously been discussed by Halliday et al. (2001) and are most likely due to the occurrence of significant asymmetrical and symmetrical deviations of the line-of-sight velocity distribution (LOSVD) from a Gaussian at $a \leq 10''$ along the major axis. In particular, for $a \leq 5''$, the measurements are consistent with the superposition of a bulge and an additional more rotationally supported component, which agrees with our finding of flatter isophotes and $b_4 > 0$ in both bands.

The comparison with the K+09 photometry is shown in Fig. 17. As for NGC 4434, the steep inner profile nicely follows the $r^{1/4}$ fit in Fig. 17, which is a fair reproduction of the whole galaxy surface brightness distribution, with the caveat of the possible multicomposition as highlighted above.

5.4. NGC 4467

NGC4467 is a faint-system classified dwarf elliptical (e.g., Bender et al. 1992, but see also the classification as an E3 galaxy by F+06). It lies at an apparent distance of $4.2'$ from NGC 4472, equivalent to 23 kpc. F+06 found that its SB profile is tidally truncated in the outer regions, where the ellipticity is also affected by the close giant companion. They also detected a small blue cluster within $0.1''$ from the nucleus, a second about $0.9''$ to the southeast. This galaxy appears to be very compact, with a nucleus brighter than galaxies of similar magnitude.

Our azimuthal SB profiles are shown in Fig. 19. Despite the bright background of NGC 4472, flux could be measured out to $a/a_e \sim 6.8$, where $\mu_g \sim 28.3$ mag/arcsec² and $\mu_i \sim 27.0$ mag/arcsec². The SB profiles deviate from an $r^{1/4}$ profile at all radii, as shown by the (O-C) profile in the same figure.

The color distribution has a shallow gradient followed by a sharp decrease starting at $a/a_e \sim 2.1$. The shape parameters (in particular b_4 , see Fig. 18) show the emergence of disk isophotes

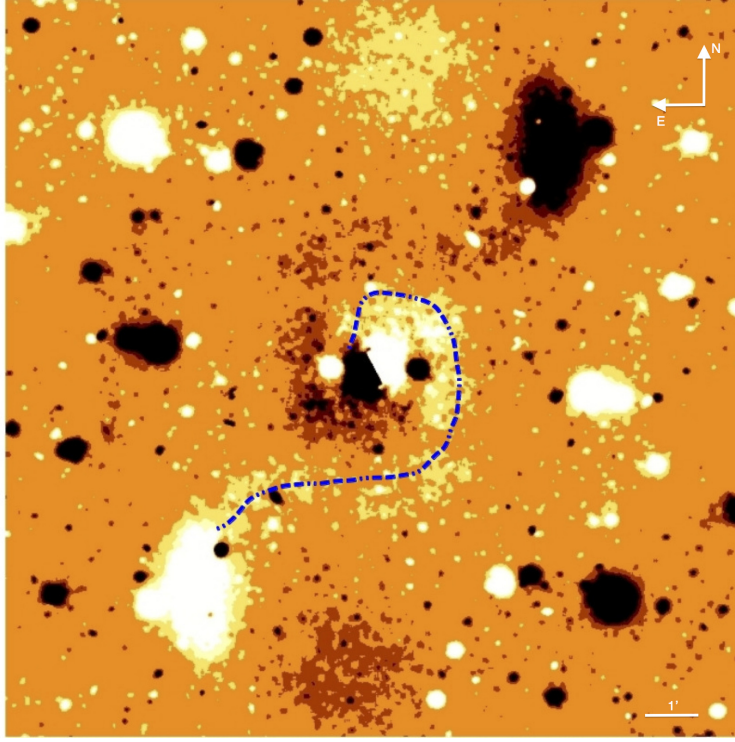


Fig. 13. Long tail connecting UGC 7636 with the core of NGC 4472, from a double-folding subtraction. The image size is 15×15 arcmin.

with higher ellipticity than the center in the outer bluer regions. Here there is a rapid transition from boxy to disk-like isophote shapes and a quite significant twisting of the isophotes of about 20° at $a \sim 20''$. These are all indications of a multicomponent system.

The comparison with the K+09 photometry (Fig. 19) again is quite good.

5.5. VCC 1199

VCC 1199 is another close companion of NGC 4472, located at $4.5'$ from its center. F+06 found that it has a surface brightness brighter than galaxies of similar luminosity and is tidally truncated in the outer regions. They also found a very thin edge-on disk aligned with the galaxy major axis, extending less than $1''$, and a large-scale spiral pattern.

The ELLIPSE azimuthal SB profiles are shown in Fig. 21. They provide a $(g-i)$ color profile with almost no gradient outside $1''$, which is the reddest in our sample. The shape parameters (see Fig. 20) show a structure very similar to NGC 4467, with a rapid and significant variation of ellipticity and position angle, and the transition from inner boxy isophotes to outer disk-like ones (although less pronounced than in NGC 4467). This confirms the multicomponent nature of the object and the presence of an outer disk.

The comparison with the K+09 photometry (Fig. 21) again is quite good.

5.6. UGC 7636

As a byproduct of this paper, we also analyzed the dwarf irregular UGC 7636 (VCC1249) (Nilson, 1973) located $5.6'$ to the southeast of NGC 4472. This object has been extensively analyzed by Arrigoni Battaia et al. (2012), who studied the tidal

interaction with NGC 4472 and the gas-stripping phenomena. They found an extensive series of shells and filaments, in agreement with Janowiecki et al. (2010). Lee et al. (2000) carried out spectroscopic observations of the system and discovered an HII region associated with this galaxy but not spatially coincident with it, lying in the envelope of the giant galaxy NGC 4472.

Lacking the possibility of deriving a geometrical model of this very irregular object, we computed mean profiles by azimuthally averaging the background-corrected flux in annuli with orientation, flattening, and center all identical to that of the best ellipse encircling the visible boundaries of the object ($\epsilon = 0.39$, P.A. = 0° deg and center at R.A. = 12h30m01.0s Dec. = +07d55m46s). The result is shown in Fig. 22. The procedure is reasonably reliable because the output changes marginally by varying the input parameters within a fair range. The method is effective in providing the trend of the color with distance. Both profiles mimic the behavior of late spiral or irregular galaxies (Capaccioli, 1973). The temptation to fit the data with the sum of an $r^{1/4}$ bulge and an exponential disk is hampered by the complexity of the body of the object (Fig. 23).

Based on Fig. 7 of Arrigoni Battaia et al. (2012), we judge that our light profiles agree with those of these authors, extending twice as deep, down to $\mu_g \sim 28.7$ mag/arcsec².

We also derived the average $(g-i)$ color profile (Fig. 22). It reddens steadily outwards with the higher slope from $a > 80$ arcsec. We note, however, that in the outer range the errors are quite large. Our result agrees with that of Arrigoni Battaia et al. (2012). Outside the main galaxy body, where the SB profiles steepen, the color becomes consistent with NGC 4472 (Fig. 8), indicating a continuity between the two systems, as expected in the close interaction of the dwarf irregular with the giant elliptical.

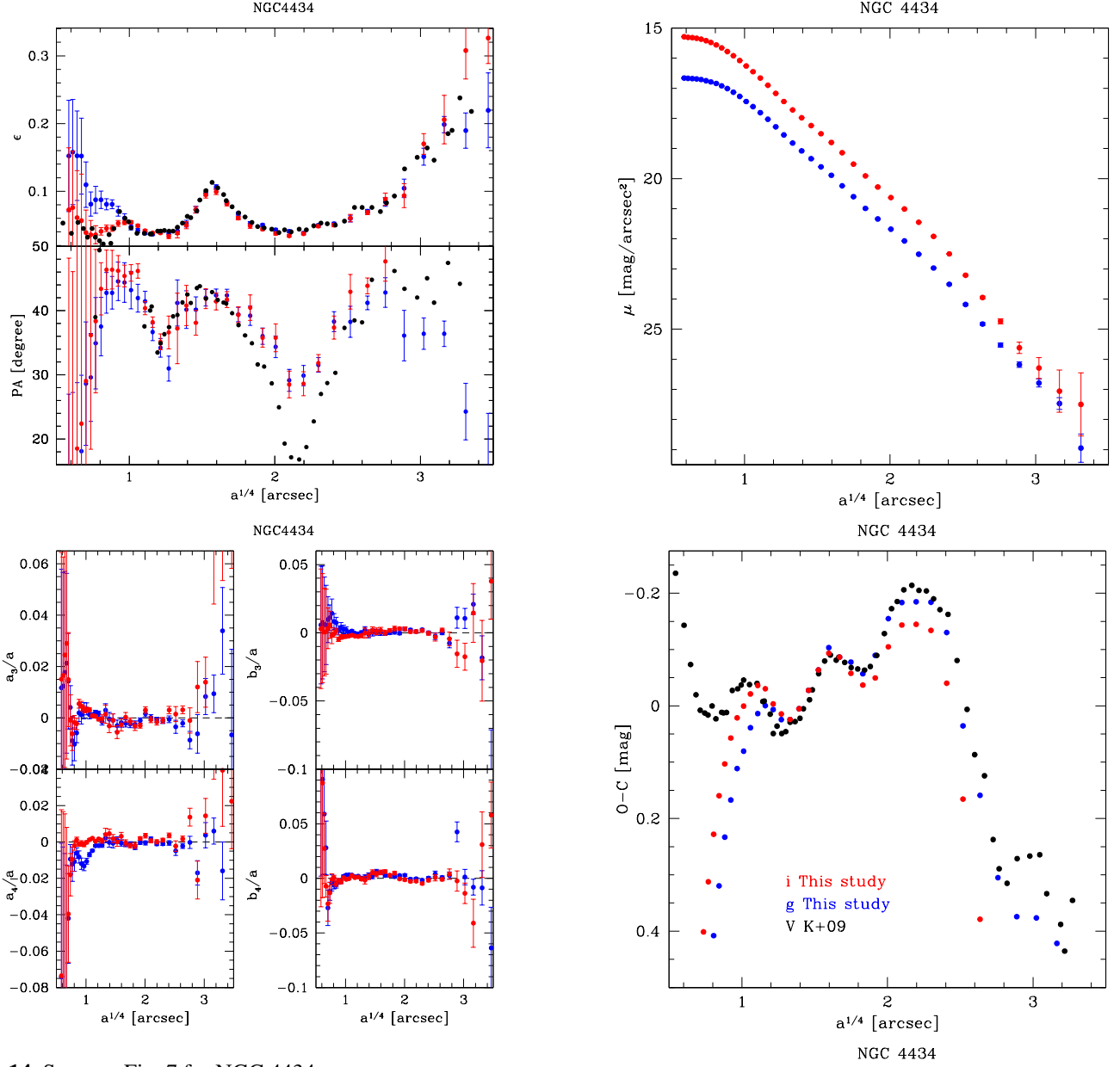


Fig. 14. Same as Fig. 7 for NGC 4434.

6. Scattered light

The surface brightness levels where our estimated effects of the extended PSF are larger than twenty per cent (0.2 mag) are ~ 29 mag/arcsec² in *g* and ~ 28 mag/arcsec² in *i*. The following is apparent from these values:

1. Typically, the azimuthally averaged light profiles derived out to a surface brightness $\mu_g \sim 28$ mag/arcsec² are little affected by scattered light for all of our angularly small galaxies. This fact may explain the remarkable agreement between our results and those of Kormendy (Kormendy et al., 2009) because this author did not mention any correction of his light profiles, which were made using a material quite different from ours.
2. The dip observed in the color profiles of NGC 4434, NGC 4464, and NGC 4467 (see Fig. 24) occurs at a surface brightness level at least two magnitudes brighter than the one where scattering becomes important.

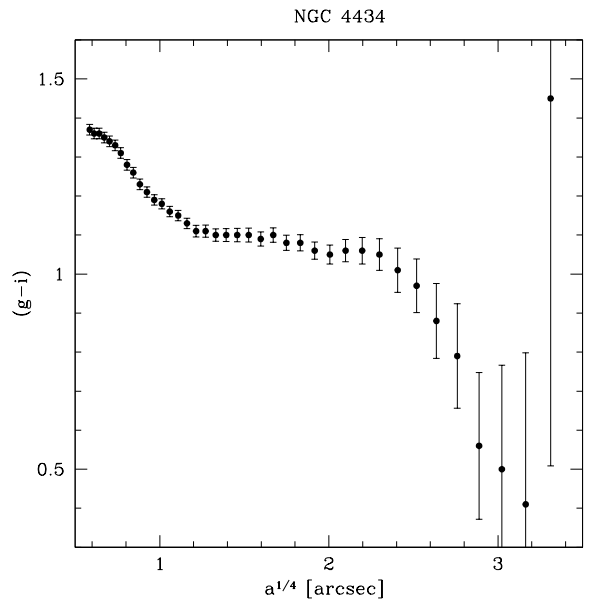


Fig. 15. NGC 4434. Top panel: azimuthally averaged light profiles in the *g* (blue) and *i* (red) bands. Center panel: (O-C) residuals of the VEGAS profiles and the V-band profile of K+09 with respect to the best-fitting $r^{1/4}$ model (see Table 4). The best match is obtained with the shifts listed in Table 5. VEGAS data for $a^{1/4} < 1.2$ are affected by seeing. Bottom panel: (*g-i*) color profile. Again the data at $a^{1/4} < 1.2$ have not been corrected for seeing.

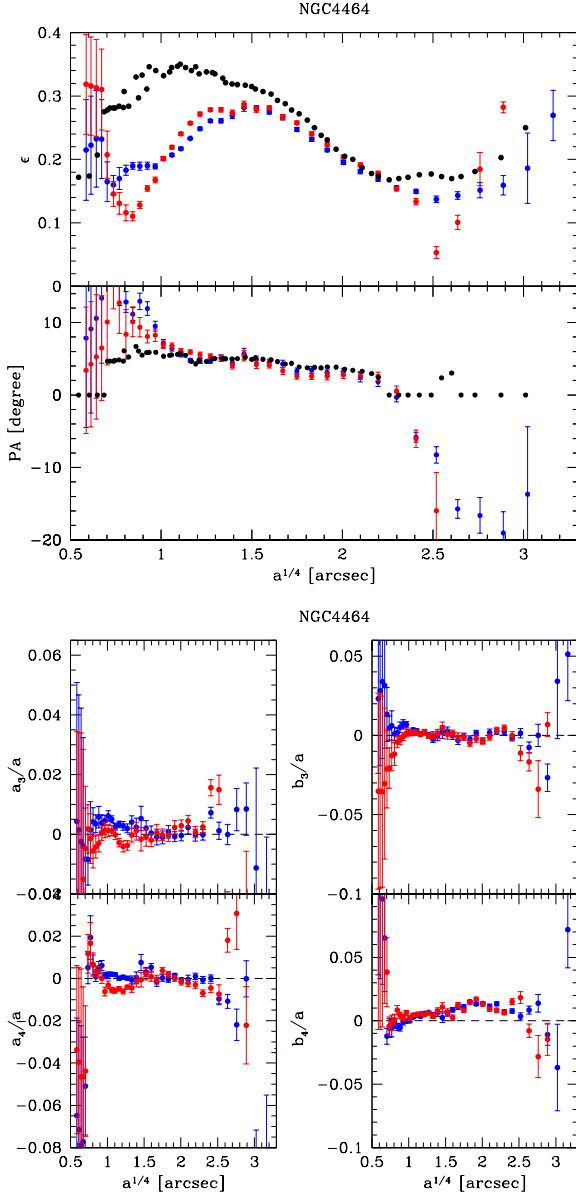


Fig. 16. Same as Fig. 7 for NGC 4464.

7. Discussion and conclusions

We have presented the VST Early-type Galaxy Survey (VEGAS) that is currently ongoing with VST/OmegaCAM (PI: M. Capaccioli) and aims at studying about one hundred galaxies mainly in the southern hemisphere. The survey is as deep as the Next Generation Virgo Survey, but has no environment constraints and is expected to provide a systematic coverage of the surface photometry in at least three optical bands, g , r , and i , down to 27.3, 26.8, and 26 mag arcsec⁻² ($S/N > 3$ per arcsec²), respectively, while u band is foreseen for a subsample of the entire survey. VEGAS is also expected to provide a census of the faint satellites (globular clusters, ultra-compact dwarfs, and dwarf galaxies; see, e.g., Cantiello et al. 2015) in the surroundings of the targeted systems, characterize their extended stellar haloes, and find evidence of the intracluster or group light around the giant galaxies in denser environments as well as signatures of merging and interactions between galaxies (e.g., tidal tails and

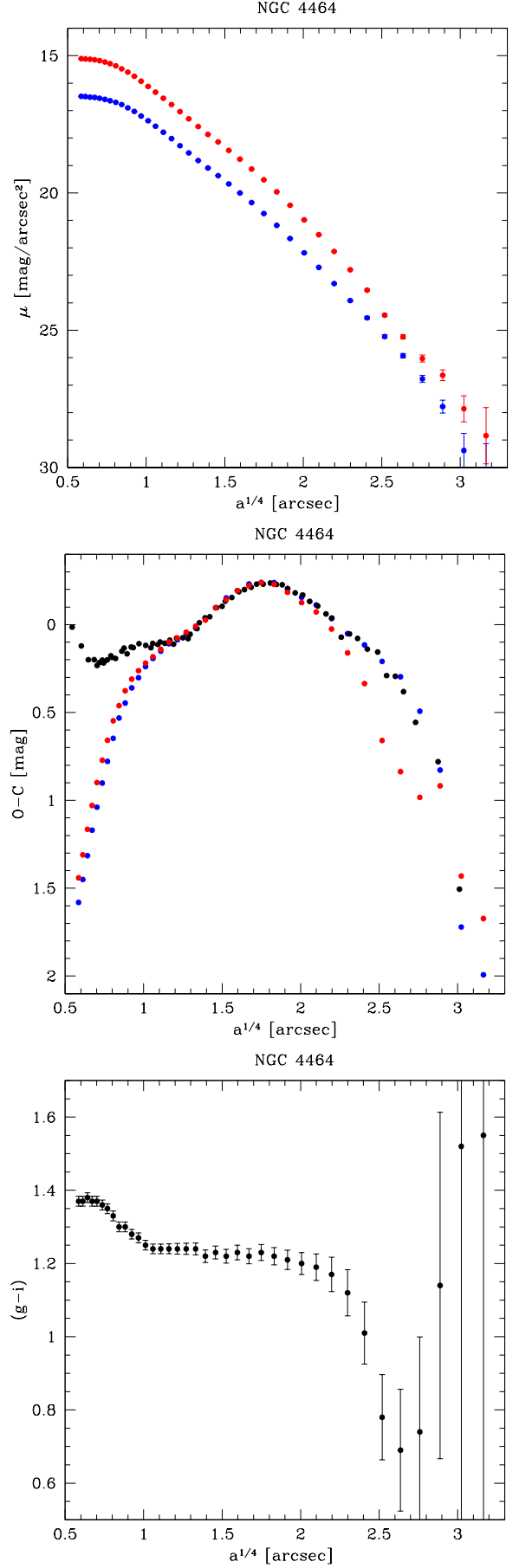


Fig. 17. Same as Fig. 15 for NGC 4464.

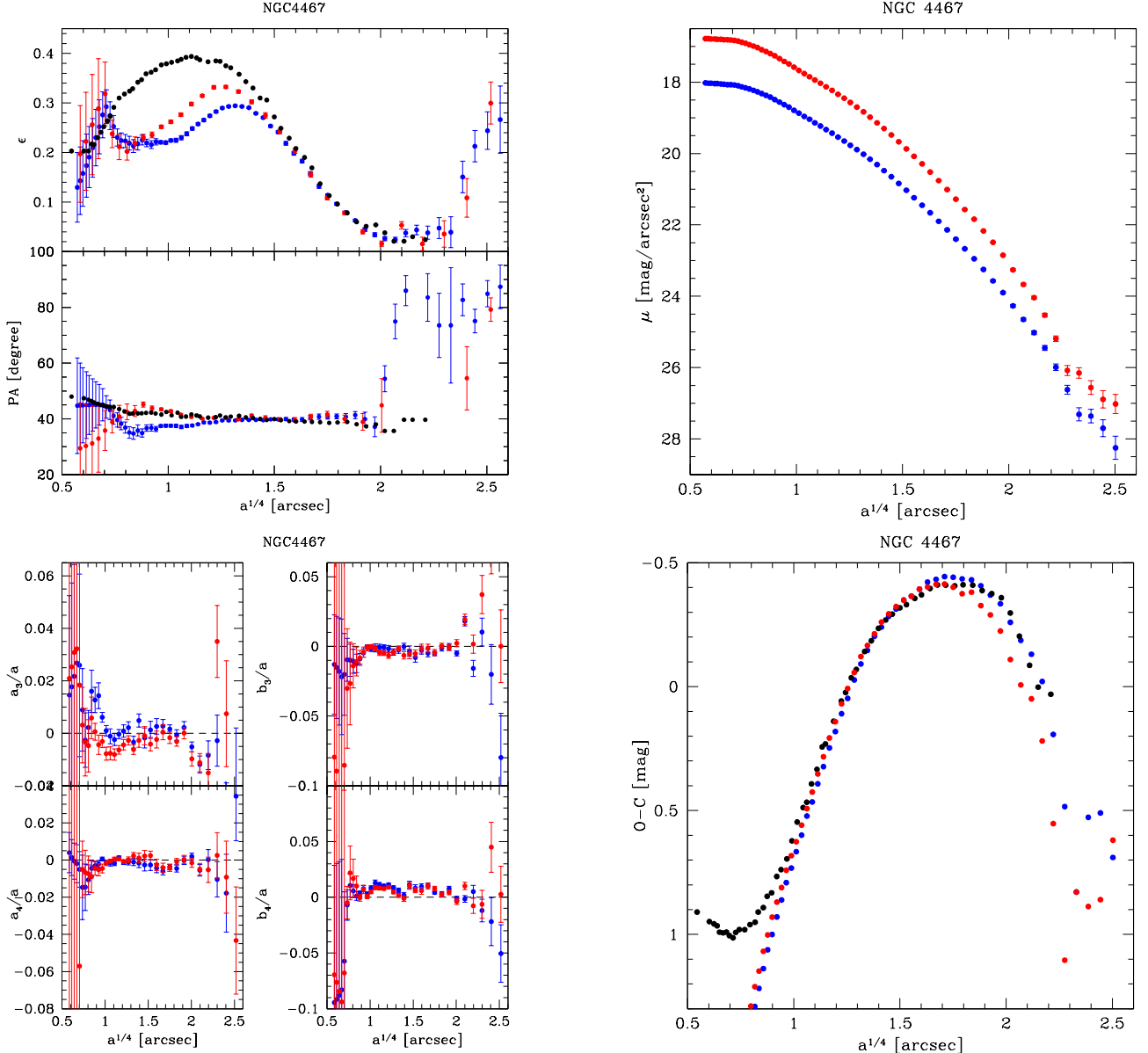


Fig. 18. Same as Fig. 7 for NGC 4467.

stellar streams) and between galaxies and the group or cluster medium.

We demonstrated the typical specifications of the survey in terms of depth and photometric accuracy and illustrated the performance of the telescope and camera as well as the data reduction and data analysis approach. To this end, we chose the field of the giant elliptical galaxy NGC 4472 in the southern extension of the Virgo cluster. This is a well-studied system with extensive literature photometry to compare our results with.

In particular, we presented the deep observations in two bands (g and i). The observations were collected with the VST/OmegaCAM in March, April and May of 2013. The major advantage of this wide-field dataset is the good seeing in both filters and the uniformity of the observing conditions (data are taken within one month), which are uncommon for service-mode observations.

The surface brightness profiles of NGC 4472 reach a depth of $27.5 \text{ mag/arcsec}^2$ in g band and 26 mag/arcsec^2 in i band, which is similar to previous deep studies (see Fig. 9). This depth

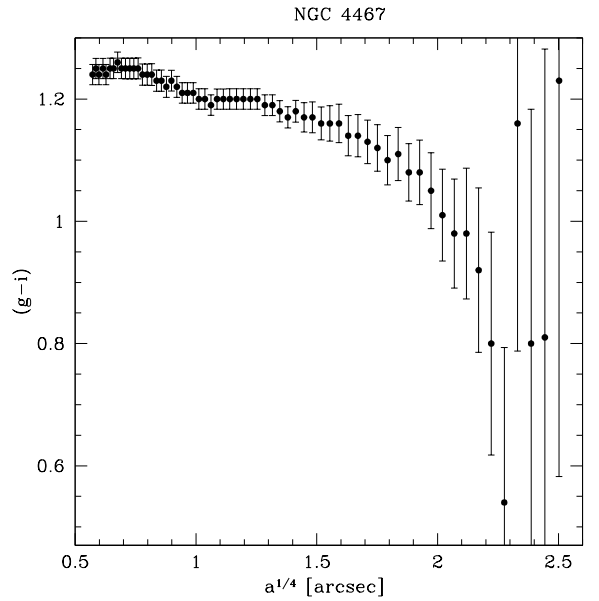


Fig. 19. Same as Fig. 15 for NGC 4467.

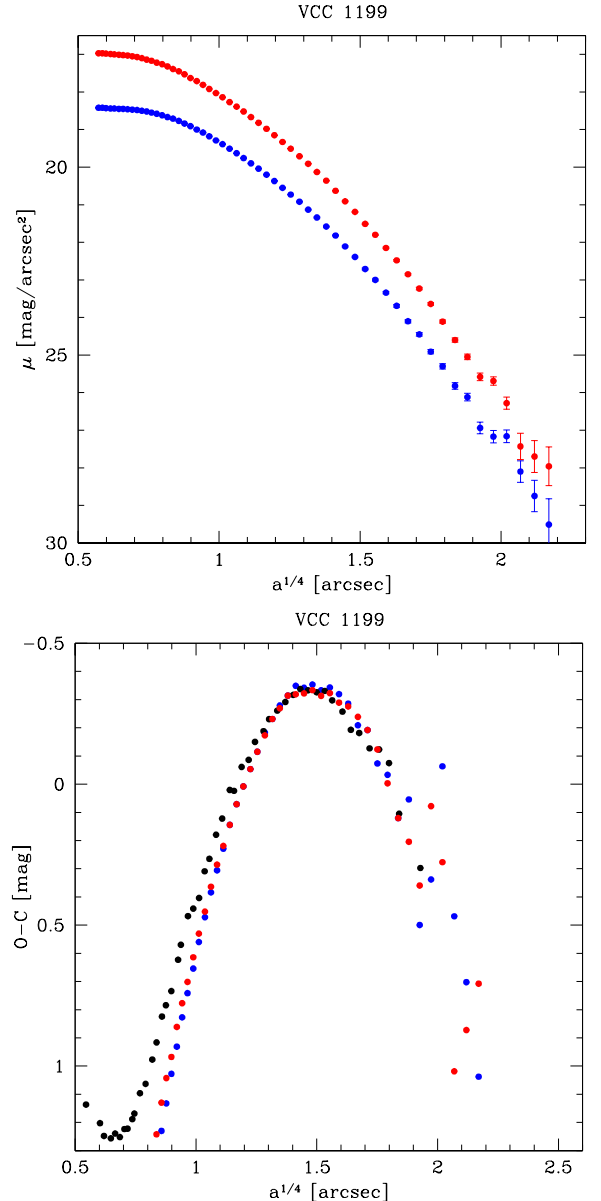
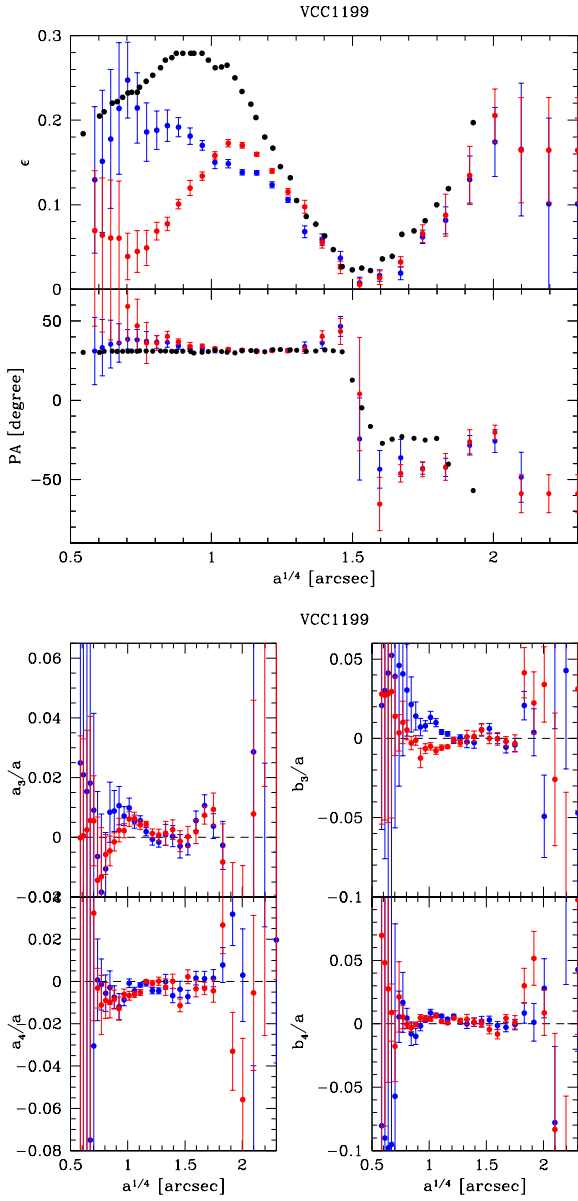


Fig. 20. Same as Fig. 7 for VCC 1199.

allowed us to spot deviations from a simple de Vaucouleurs profile and in particular a change of slope at $a \sim 14''.2$ (see Fig. 8) that we have associated with a decoupled ICL component that has not been detected in previous analyses (e.g., K+09). The ICL in the Virgo Cluster has been discussed before and is mainly concentrated in the cluster core. It has been detected either through direct deep imaging (Mihos et al., 2005) or using planetary nebulae as stellar light tracers (ICPNe, e.g., Arnaboldi et al. 2002; Aguerri et al. 2005). In the area around NGC 4472, evidence of ICL has been obtained with PNe by Feldmeier et al. (2004) (see also Castro-Rodríguez et al. 2009 for a summary of ICPNe observations over a range of Virgo cluster -centric distances). However, none of these studies has addressed a detailed 2D distribution of the ICL around NGC 4472 and its connection with the giant galaxy. Here we stress that the simple inspection of the deep SB profile of NGC 4472 clearly shows a diffuse component starting to dominate at $\mu_g \sim 26.5$ mag/arcsec² (see Fig. 8), which is compatible with the typical SB values at which Zibetti et al.

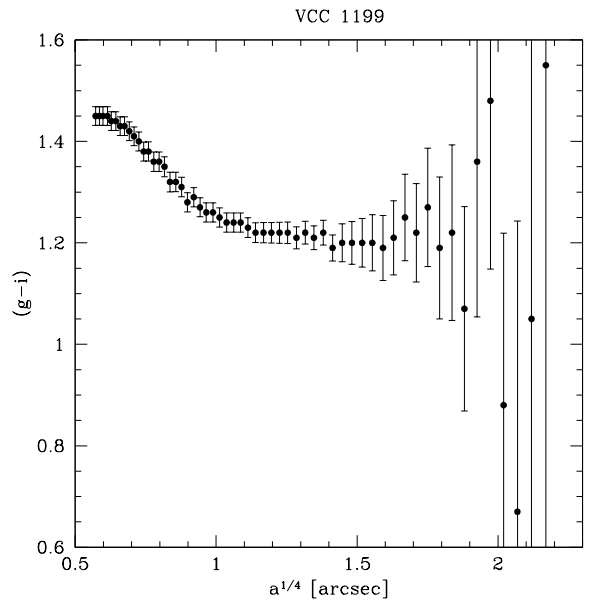


Fig. 21. Same as Fig. 15 for VCC 1199.

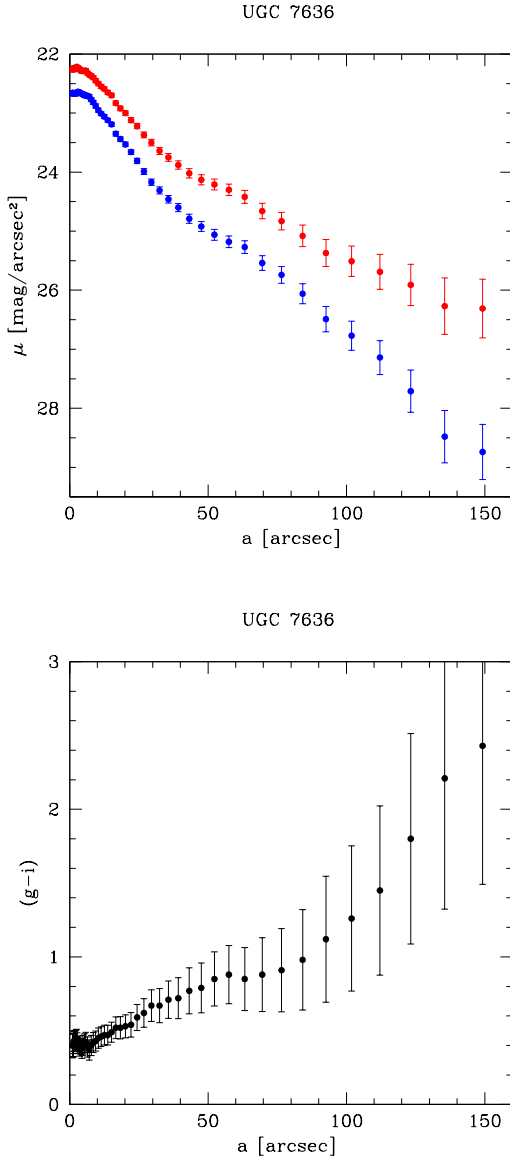


Fig. 22. UGC 7636. Top panel: azimuthally averaged light profiles in the g (blue dots) and i (red dots) bands. Bottom panel: $(g-i)$ color profile.

(2005) have observed a change of slope induced by the ICL in a series of stacked galaxy clusters.

We note that the trend of the residuals of the luminosity profiles of NGC 4472 with respect to an $r^{1/4}$ best-fitting model has some striking analogies with the similar curve for NGC 3379 (de Vaucouleurs & Capaccioli, 1979). In addition to a bright extended core, we found evidence for a wavy pattern that is possibly associated with shells of diffuse material.

We also studied the fainter ETGs in the one square degree of the OmegaCAM field: NGC 4434, NGC 4464, NGC 4467, and VCC 1199, including the dwarf irregular UGC 7636 in the proximity of the giant galaxy NGC 4472. For the two galaxies projected onto the bright halo of NGC 4472, NGC 4467 and VCC 1199, located at $r \sim 4.1'$ and $r \sim 4.5'$ from NGC 4472, we were able to estimate and subtract the galaxy background and trace the SB distribution down to $\mu_g \sim 29$ mag/arcsec² and $\mu_i \sim 27.5$ mag/arcsec², which is well beyond the nominal specifications of

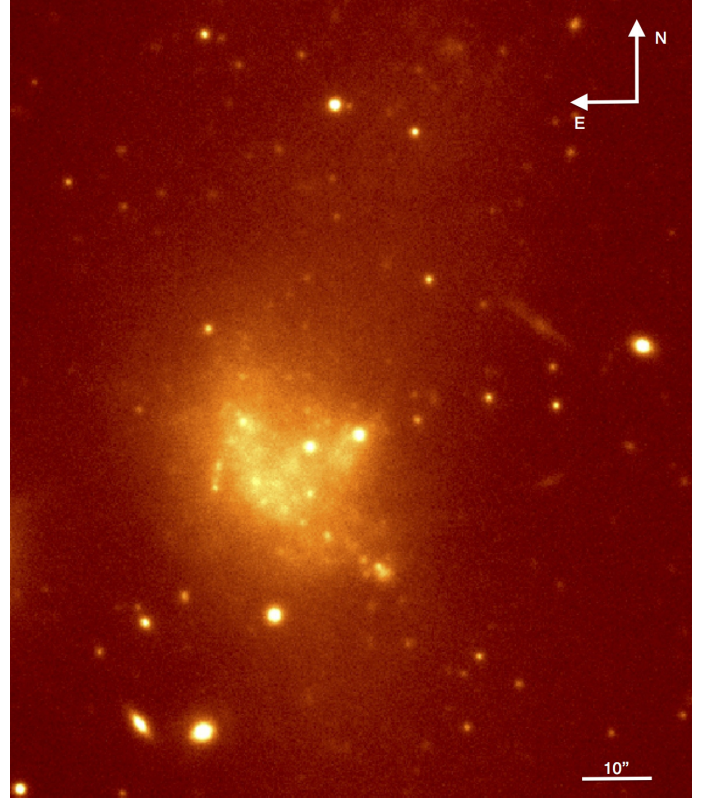


Fig. 23. VST g -band image (100×117 arcsec) of the interacting system UGC 7636.

the survey. We reached an even greater depth for the farther systems NGC 4464 and NGC 4434, which are not (deeply) affected by the extended halo of NGC 4472 and for which we have gone down to $29 - 30$ mag/arcsec² in g band and ~ 28 mag/arcsec² in i band. Together with the extremely good comparison with the V-band photometry by Kormendy et al. (2009), at least for our g band, this demonstrates that for normal galaxies the survey VEGAS provides an unprecedented view of the faint features around early-type galaxies, with less than one night of telescope time per galaxy (in g , r , i).

For all these systems we have highlighted some substructures that were defined as deviations from a simple de Vaucouleurs (1948) best-fit profile, as done for NGC 4472. In particular, we found evidence of bumps seen in both bands for the intermediate-luminosity systems NGC 4434 and NGC 4464. These bumps are associated with strongly varying values of the ellipticity and P.A. and a_4 and b_4 parameters, hence suggesting some substructures. They are possibly also seen in their kinematics, as for NGC 4464 (Halliday et al. 2001), but are not clearly seen in NGC 4434 (e.g., Simien & Prugniel 1997).

The color profiles, at variance with simulations (Tortora et al., 2013), do not show either the sharp decrease of the average value in the first r_e for objects fainter than $M_g \sim -19$ or the pattern of the gradient as a function of the host galaxy absolute magnitude, which remains very flat with M_{tot} . We instead found an indication, which needs to be confirmed, that for $r > 3r_e$ a very negative colour gradient develops in some galaxies, which apparently vanishes at $r \approx 8r_e$ (see Fig. 24).

To conclude, we illustrated the performance and accuracy achieved with the VST/OmegaCAM to produce surface photometry of early-type galaxies also in very extreme conditions. For the case of NGC 4472 the extended halo around the giant galaxy,

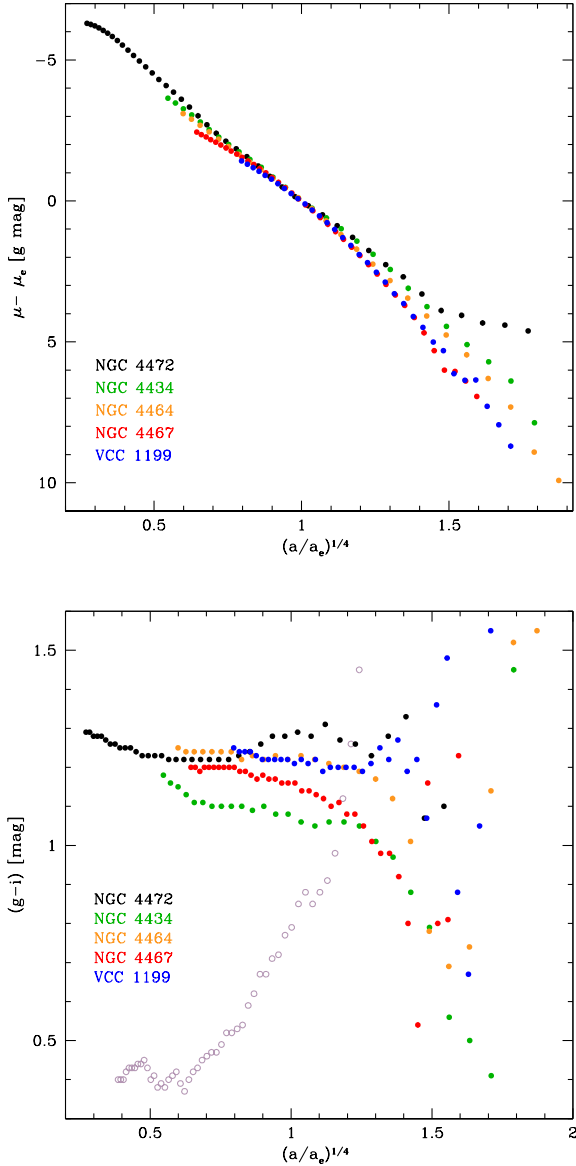


Fig. 24. Top panel: azimuthally averaged light profiles in the g band for the five ETGs of this paper scaled to their effective parameters. Bottom panel: assembly of the $(g-i)$ color profiles for the five ETGs and for the interacting system UGC 7636 (open circles).

reaching the edge of the one-square-degree field of view, has allowed us to fully test the procedure for data reduction and background subtraction. The results obtained with our observations are similar in accuracy to the collection of observations from different telescopes (see K+09). In the future we expect to implement a more general surface analysis including a wider set of photometric laws (Sersic, cored Sersics, double de Vaucouleurs, etc.) to characterize the SB measurements in a larger sample of galaxies and thus discuss results in the context of galaxy formation theories. Moreover, a forthcoming paper based on the same data as were used in the present work will be devoted to the study of small stellar systems (e.g., GCs and UCDs).

Acknowledgements. The optical imaging is collected at the ESO VLT Survey Telescope on Cerro Paranal under program ID 090.B-0414(D) and 091.B-0614(A), using the Italian INAF Guaranteed Time Observations. The data re-

duction for this work was carried out with the computational infrastructures of the INAF-VST Center at Naples (VSTceN). The authors wish to thank L. Ferrarese, C. Mihos, and S. Janowiecki for the data provided, C. Tortora for illuminating discussion on colors, and R. Peletier for the ongoing discussion on the best way to remove the sky background. This research made use of the NASA/IPAC Extragalactic Database (NED), which is operated by the Jet Propulsion Laboratory, California Institute of Technology, under contract with the National Aeronautics and Space Administration, and has been partly supported by the PRIN-INAF “Galaxy evolution with the VLT Survey Telescope (VST)” (PI A. Grado). M. Cantiello acknowledges support from Progetto FSE Abruzzo “Sapere e Crescita”.

References

- Aguerri, J. A. L., Gerhard, O. E., Arnaboldi, M., et al. 2005, *AJ*, 129, 2585
 Andersen, M. I., Freyhammer, L., & Storm, J. 1995, *Calibrating and Understanding HST and ESO Instruments*, 53, 87
 Arnaboldi, M., Aguerri, J. A. L., Napolitano, N. R., et al. 2002, *AJ*, 123, 760
 Arnaboldi, M., Ventimiglia, G., Iodice, E., Gerhard, O., & Coccato, L. 2012, *A&A*, 545, A37
 Arnold, J. A., Romanowsky, A. J., Brodie, J. P., et al. 2011, *ApJ*, 736, L26
 Arrigoni Battaia, F., Gavazzi, G., Fumagalli, M., et al. 2012, *A&A*, 543, AA112
 Ashman, K. M., & Zepf, S. E. 1992, *ApJ*, 384, 50
 Balcells, M., Graham, A. W., & Peletier, R. F. 2007, *ApJ*, 665, 1104
 Bender, R., Surma, P., Doebereiner, S., Moellenhoff, C., & Madejsky, R. 1989, *A&A*, 217, 35
 Bertin, E., & Arnouts, S. 1996, *A&AS*, 117, 393
 Bertin, E., Mellier, Y., Radovich, M., et al. 2002, *Astronomical Data Analysis Software and Systems XI*, 281, 228
 Bertin, E. 2006, *Astronomical Data Analysis Software and Systems XV*, 351, 112
 Binney, J., & Petrou, M. 1985, *MNRAS*, 214, 449
 Sánchez-Blázquez, P., Forbes, D. A., Strader, J., Brodie, J., & Proctor, R. 2007, *MNRAS*, 377, 759
 Blom, C., Forbes, D. A., Brodie, J. P., et al. 2012, *MNRAS*, 426, 1959
 Brodie, J. P., Usher, C., Conroy, C., et al. 2012, *ApJ*, 759, L33
 Brodie, J. P., Romanowsky, A. J., Strader, J., et al. 2014, *ApJ*, 796, 52
 Bruzual, G., & Charlot, S. 2003, *MNRAS*, 344, 1000
 Cantiello, M., Blakeslee, J. P., Raimondo, G., et al. 2005, *ApJ*, 634, 239
 Cantiello, M., & Blakeslee, J. P. 2007, *ApJ*, 669, 982
 Cantiello, M., Grado, A., Blakeslee, J. P., et al. 2013, *A&A*, 552, AA106
 Cantiello, M., Capaccioli, M., Napolitano, N., et al. 2015, *A&A*, 576, AA14
 Caon, N., Capaccioli, M., & D’Onofrio, M. 1993, *MNRAS*, 265, 1013
 Caon, N., Capaccioli, M., & D’Onofrio, M. 1994, *A&AS*, 106, 199
 Capaccioli, M. 1973, *Mem. Soc. Astron. Italiana*, 44, 417
 Capaccioli, M., & de Vaucouleurs, G. 1983, *ApJS*, 52, 465
 Capaccioli, M., Held, E. V., & Nieto, J.-L. 1987, *AJ*, 94, 1519
 Capaccioli, M. 1988, *Bol. Acad. Nac. Cienc. Córdoba, Argent.*, Tomo 58, Nos. 3 - 4, p. 317 - 367, 58, 317
 Capaccioli, M., Caon, N., & D’Onofrio, M. 1992, *MNRAS*, 259, 323
 Capaccioli, M., & Schipani, P. 2011, *The Messenger*, 146, 2
 Carlberg, R. G. 1984, *ApJ*, 286, 403
 Castro-Rodríguez, N., Arnaboldi, M., Aguerri, J. A. L., et al. 2009, *A&A*, 507, 621
 Chen, C.-W., Côté, P., West, A. A., Peng, E. W., & Ferrarese, L. 2010, *ApJS*, 191, 1
 Coccato, L., Gerhard, O., Arnaboldi, M., et al. 2009, *MNRAS*, 394, 1249
 Coccato, L., Gerhard, O., & Arnaboldi, M. 2010, *MNRAS*, 407, L26
 Côté, P., Marzke, R. O., & West, M. J. 1998, *ApJ*, 501, 554
 Côté, P., Blakeslee, J. P., Ferrarese, L., et al. 2004, *ApJS*, 153, 223
 Côté, P., Ferrarese, L., Jordán, A., et al. 2007, *ApJ*, 671, 1456
 D’Abrusco, R., Fabbiano, G., & Zezas, A. 2015, *arXiv:1503.04819*
 Daddi, E., Renzini, A., Pirzkal, N., et al. 2005, *ApJ*, 626, 680
 de Jong, J. T. A., Verdoes Kleijn, G. A., Kuijken, K. H., & Valentijn, E. A. 2013, *Experimental Astronomy*, 35, 25
 de Vaucouleurs, G. 1948, *Annales d’Astrophysique*, 11, 247
 de Vaucouleurs, G., & Capaccioli, M. 1979, *ApJS*, 40, 699
 de Vaucouleurs, G., de Vaucouleurs, A., Corwin, H. G., Jr., et al. 1991, *Third Reference Catalogue of Bright Galaxies. Volume I: Explanations and references. Volume II: Data for galaxies between 0^h and 12^h. Volume III: Data for galaxies between 12^h and 24^h.*, by de Vaucouleurs, G.; de Vaucouleurs, A.; Corwin, H. G., Jr.; Buta, R. J.; Paturel, G.; Fouqué, P., Springer, New York, NY (USA), 1991, 2091 p., ISBN 0-387-97552-7, Price US\$ 198.00. ISBN 3-540-97552-7, Price DM 448.00. ISBN 0-387-97549-7 (Vol. I), ISBN 0-387-97550-0 (Vol. II), ISBN 0-387-97551-9 (Vol. III).
 Duc, P.-A., Cuillandre, J.-C., Karabal, E., et al. 2015, *MNRAS*, 446, 120

Feldmeier, J. J., Ciardullo, R., Jacoby, G. H., & Durrell, P. R. 2004, *ApJ*, 615, 196

Ferrarese, L., Côté, P., Jordán, A., et al. 2006, *ApJS*, 164, 334

Ferrarese, L., Côté, P., Cuillandre, J.-C., et al. 2012, *ApJS*, 200, 4

Forbes, D. A., Brodie, J. P., & Grillmair, C. J. 1997, *AJ*, 113, 1652

Forbes, D. A., Spitler, L. R., Strader, J., et al. 2011, *MNRAS*, 413, 2943

Gonzalez, A. H., Zabludoff, A. I., & Zaritsky, D. 2005, *ApJ*, 618, 195

Grado, A., Capaccioli, M., Limatola, L., & Getman, F. 2012, *Memorie della Società Astronomica Italiana Supplementi*, 19, 362

Halliday, C., Davies, R. L., Kuntschner, H., et al. 2001, *MNRAS*, 326, 473

Hopkins, P. F., Bundy, K., Hernquist, L., Wuyts, S., & Cox, T. J. 2010, *MNRAS*, 401, 1099

Huang, Z., Radovich, M., Grado, A., et al. 2011, *A&A*, 529, A93

Ibata, R. A., Gilmore, G., & Irwin, M. J. 1994, *Nature*, 370, 194

James, F., & Roos, M. 1975, *Computer Physics Communications*, 10, 343

Janowiecki, S., Mihos, J. C., Harding, P., et al. 2010, *ApJ*, 715, 972

Jedrzejewski, R. I. 1987, *MNRAS*, 226, 747

Jensen, J. B., Tonry, J. L., Barris, B. J., et al. 2003, *ApJ*, 583, 712

Jordán, A., Blakeslee, J. P., Côté, P., et al. 2007, *ApJS*, 169, 213

Kim, E., Lee, M. G., & Geisler, D. 2000, *MNRAS*, 314, 307

Kormendy, J. 1985, *ApJ*, 295, 73

Kormendy, J., Fisher, D. B., Cornell, M. E., & Bender, R. 2009, *ApJS*, 182, 216

Kuijken, K. 2011, *The Messenger*, 146, 8

Lee, H., Richer, M. G., & McCall, M. L. 2000, *ApJ*, 530, L17

Mei, S., Blakeslee, J. P., Côté, P., et al. 2007, *ApJ*, 655, 144

Mihos, J. C., Harding, P., Feldmeier, J., & Morrison, H. 2005, *ApJ*, 631, L41

Mihos, J. C., Harding, P., Rudick, C. S., & Feldmeier, J. J. 2013, *ApJ*, 764, L20

Napolitano, N. R., Romanowsky, A. J., Coccato, L., et al. 2009, *MNRAS*, 393, 329

Napolitano, N. R., Pota, V., Romanowsky, A. J., et al. 2014, *MNRAS*, 439, 659

Nilson, P. 1973, *Nova Acta Regiae Soc. Sci. Upsaliensis Ser. V*, 0

Oser, L., Ostriker, J. P., Naab, T., Johansson, P. H., & Burkert, A. 2010, *ApJ*, 725, 2312

Peletier, R. F., Davies, R. L., Illingworth, G. D., Davis, L. E., & Cawson, M. 1990, *AJ*, 100, 1091

Peng, E. W., Jordán, A., Côté, P., et al. 2006, *ApJ*, 639, 95

Pipino, A., D'Ercole, A., & Matteucci, F. 2008, *A&A*, 484, 679

Pohlen, M., & Trujillo, I. 2006, *A&A*, 454, 759

Proctor, R. N., Forbes, D. A., Romanowsky, A. J., et al. 2009, *MNRAS*, 398, 91

Prugniel, P., & Simien, F. 1996, *A&A*, 309, 749

Simien, F., & Prugniel, P. 1997, *A&AS*, 122, 521

Radovich, M., Arnaboldi, M., Ripepi, V., et al. 2004, *A&A*, 417, 51

Romanowsky, A. J., Douglas, N. G., Arnaboldi, M., et al. 2003, *Science*, 301, 1696

Romanowsky, A. J., Strader, J., Spitler, L. R., et al. 2009, *AJ*, 137, 4956

Romanowsky, A. J., Strader, J., Brodie, J. P., et al. 2012, *ApJ*, 748, 29

Saglia, R. P., Maraston, C., Thomas, D., Bender, R., & Colless, M. 2002, *ApJ*, 579, L13

Sersic, J. L. 1968, *Atlas de galaxias australes* (Cordoba, Argentina: Observatorio Astronomico), 1968)

Shen, S., Mo, H. J., White, S. D. M., et al. 2003, *MNRAS*, 343, 978

Tal, T., van Dokkum, P. G., Nelán, J., & Bezanson, R. 2009, *AJ*, 138, 1417

Tonry, J., & Schneider, D. P. 1988, *AJ*, 96, 807

Tonry, J. L., Dressler, A., Blakeslee, J. P., et al. 2001, *ApJ*, 546, 681

Tortora, C., Romeo, A. D., Napolitano, N. R., et al. 2011, *MNRAS*, 411, 627

Tortora, C., Pipino, A., D'Ercole, A., Napolitano, N. R., & Matteucci, F. 2013, *MNRAS*, 435, 786

Usher, C., Forbes, D. A., Brodie, J. P., et al. 2012, *MNRAS*, 426, 1475

Usher, C., Forbes, D. A., Brodie, J. P., et al. 2015, *MNRAS*, 446, 369

van Dokkum, P. G., Whitaker, K. E., Brammer, G., et al. 2010, *ApJ*, 709, 1018

Watkins, A. E., Mihos, J. C., Harding, P., & Feldmeier, J. J. 2014, *ApJ*, 791, 38

Whitmore, B. C., & Bell, M. 1988, *ApJ*, 324, 741

Wood, S. N. 2007, *arXiv:0709.3906*

Wood, S. N. (2011) Fast stable restricted maximum likelihood and marginal likelihood estimation of semiparametric generalized linear models. *Journal of the Royal Statistical Society (B)* 73(1):3-36

Yoon, S.-J., Yi, S. K., & Lee, Y.-W. 2006, *Science*, 311, 1129

Zibetti, S., White, S. D. M., & Brinkmann, J. 2004, *MNRAS*, 347, 556

Zibetti, S., White, S. D. M., Schneider, D. P., & Brinkmann, J. 2005, *MNRAS*, 358, 949

Appendix A: Data reduction

A.1. Overscan correction and master bias

For each exposure, the median value of an overscan region is computed and then subtracted, row by row. Then a masterbias, created as a sigma-clipped (5σ) average of (at least) ten bias frames, is subtracted from all the other scientific and technical exposures for full 2D bias removal.

A.2. Flat-fielding

The conversion from photons to ADUs, called gain, varies over the whole camera frame, owing to the optical design, pixel response, and electronics behavior. In principle, an exposure of a uniformly illuminated field is sufficient to build a gain-variation map. We use exposures of the sky at twilight. Because of the wide field of the instrument, these twilight flat fields may suffer from illumination variations amounting to some percent units on a degree scale. This undesired effect is mitigated by the illumination-correction procedure described below (Sect. A.5).

A master flat-field is created by averaging a set of twilight flat-fields (typically five); a sigma-clipping rejection procedure helps removing non-stationary features. The method tracks the gain variations at high spatial frequencies well, but sometimes fails at low frequencies. The reason may be the color and flux mismatch between twilight and science exposures. In this case, the twilight flat-fields are combined with some science images taken during the same night with exposure times similar to those of the images under correction. This type of frame combination has been used to process the NGC 4472 exposures. Specifically, we applied the formula

$$MasterFlat^i = \frac{MFlat^i}{\langle MFlat^i \rangle} \times Gain^i \times IC^i, \quad (A.1)$$

where

$$MFlat^i = \frac{SFlat_{low}^i}{\langle SFlat_{low}^i \rangle} \times \frac{TFlat^i}{TFlat_{low}^i}. \quad (A.2)$$

The superscript indicates the i^{th} CCD, the subscript *low* is for the low-frequency spatial component obtained by applying a low-pass spatial filter in the Fourier space. The master twilight (TFlat) and master skyflat (SFlat) are produced using a sigma-clipped average of overscan- and bias-corrected twilight frames and sky frames, respectively. The choice of the exposures used to produce the master skyflat requires special care. The dithering pattern of the exposures must be wider than the largest structure in the images (such as galaxies or the halo of bright stars) to avoid fictitious gain variations. Moreover, all the bright features in the science images (galaxies stars, halos, etc.) are accurately masked. In all these formulas, chevron brackets indicate medians done on a 1000×2000 pixel central spot in the CCDs.

The terms $Gain^i \times IC^i$ accounts for the average CCD gain and for the illumination correction and is described in Sect. A.5.

A.3. Defringing

The i -band images need a correction for the fringe pattern caused by thin-film interference of sky emission lines in the detector. This is an additive component and, as such, it must be subtracted. The first step of the defringing is determining the fringing pattern by the formula

$$frP = \frac{SFlat}{TFlat} \times \langle TFlat \rangle - imsurfit\left(\frac{SFlat}{TFlat} \times \langle TFlat \rangle\right), \quad (A.3)$$

where *imsurf* indicates a fifth-order surface Chebyshev polynomial fit.

Once the pattern is found, it must be subtracted from the science image,

$$Im_{defring} = Im_{fring} - fr_{scale} \times frP \quad (A.4)$$

using a scale factor, fr_{scale} , that is derived as follows. We assume that the fringe-pattern features are quite stable in time. We have then a priori determined the regions in the OmegaCAM frame where they clearly stand out. The best scale factor minimizes within these regions the absolute differences between peak and valley values in the fringe-corrected image.

A.4. Gain harmonization

The gain harmonization procedure sets the photometric zero point over the whole OmegaCAM mosaic. We derive the relative gain coefficients that minimize the background differences in adjacent CCDs. First we select a set of auxiliary scientific images belonging to the same night and having approximately the same exposure time as the science image to be calibrated.

Each such image is heavily clipped around the median pixel level to flag out all the sources; holes created by the procedure are filled up in a subsequent step. After overscan and bias correction, the auxiliary images are properly scaled and sigma-clipped combined. The scaling factor is calculated as the median over the scientific image divided by the median of the medians. All the holes surviving the stacking procedure are filled by interpolated values. The resulting image, corrected for the master twilight flat-frame, is then fitted with a third-order polynomial surface. This is used to compute 32 median values over subregions of 1000×2000 pixels centered on each CCD. These values, normalized to the median of all the CCDs medians, are the relative gain corrections. The gain harmonization correction typically ranges from 0.9 to 1.17.

A.5. Illumination correction

Another effect to be considered is the scattered light in the telescope and in the camera that is due to insufficient baffling, which produces an uncontrolled redistribution of light. In the presence of this additive contribution to the signal, the flat field is no longer an accurate model of the spatial detector response. Indeed, after flat-fielding, the image background appears perfectly flat, but the photometric response is position dependent (Andersen et al., 1995). This bias in the flat field can be mitigated by applying the illumination correction (IC) map. We determine such a map by comparing our magnitude measurements of stars observed in equatorial fields with the corresponding SDSS DR8 psf magnitudes.

The differences of magnitudes, $\Delta m(x, y)$, as a function of the position are fitted with a generalized additive model (GAM) (Wood, 2011) to derive a surface used to correct the science images during the pre-reduction stage. GAM also provides a well-behaved surface when the standard stars do not sample the field of view uniformly, and in general the resulting image has a smoother behavior at the frame edges than do simple polynomial fits. Figures A.1 and A.2 illustrate the position dependency of the zero point before and after the IC application and the IC shape. The statistics on the differences in magnitude between the reference photometric catalog and the magnitude of sources before and after the illumination correction are the following: STD = 0.09 and MAD = 0.084 before and STD 0.05 and MAD 0.026

Table A.1. Absolute photometric calibration for NGC 4472.

Band	Zero Point	Color term ($g-i$)	Extinction
g	24.864 ± 0.006	0.027 ± 0.006	0.180 ± 0.0
i	24.160 ± 0.006	-0.004 ± 0.005	0.043 ± 0.0

after the correction. The IC was created using 2189 sources. As shown in Eq. A.1, the IC is embedded in the master flat field. In this way, the images have a uniform zero point all over the field, but the background does not appear flat. To have a flat background, the properly rescaled IC surface is also subtracted from the images.

A.6. Photometric and astrometric calibration

In VST-tube, the absolute photometric calibration is performed by observing standard star fields each night and comparing their OmegaCAM magnitudes with SDSS DR8 photometry. For the data analyzed in this work, the absolute photometric calibration was derived using 4392 sources in the g and 4489 in the i band. For each night and band, the zero point (ZP) and color term were obtained using the tool Photcal provided by Mario Radovich (Radovich et al., 2004). The extinction coefficient was derived from the extinction curve M.OMEGACAM.2011-12-01T16:15:04.474 provided by ESO. Table A.1 lists the fitted values for the zero points and color terms obtained for the nights used for the absolute photometric calibration.

Relative photometric correction among the exposures was obtained by minimizing the quadratic sum of magnitude differences between overlapping detections. The tool used for this task was SCAMP (Bertin, 2006). The final coadded images were then normalized to an exposure time of one second of time and a ZP of 30 magnitudes.

The absolute and relative astrometric calibrations were performed using SCAMP. For the absolute astrometric calibration we refer to the 2MASS catalog. Compared to this catalog, the rms of the residuals after the astrometric correction has been applied is $0.28''$. The rms on the residuals of the differences between coordinates of overlapping detections, that is, the internal astrometric accuracy, is $0.09''$. The image resampling for the application of the astrometric solution and final image coaddition is made with the program SWARP (Bertin et al., 2002).

Appendix B: Convolution by the scattering profile of the point spread function

To evaluate the contribution of the scattered light, which is indeed a reason of concern for the surface photometry of galaxy outskirts, we first derived an extended stellar point spread function (PSF) by combining the unsaturated azimuthally averaged light profiles of stars of different luminosities, properly shifted in magnitudes. Our interest is not in the seeing profile, that is, in the inner few arcseconds of the PSF, but instead in the wings produced by the scattering in the mirror and in the atmosphere (Capaccioli & de Vaucouleurs, 1983).

The measured PSF profiles for the g and i band are shown in Fig. B.1, normalized to unity up to the last observed point. Although the inner PSF has an average behavior that is uncorrelated with the actual seeing of each of the images contributing to the final mosaic, it could not be used for deconvolving the inner regions of the galaxy. Nonetheless, it must be kept just for providing a way to normalize the PSF itself.

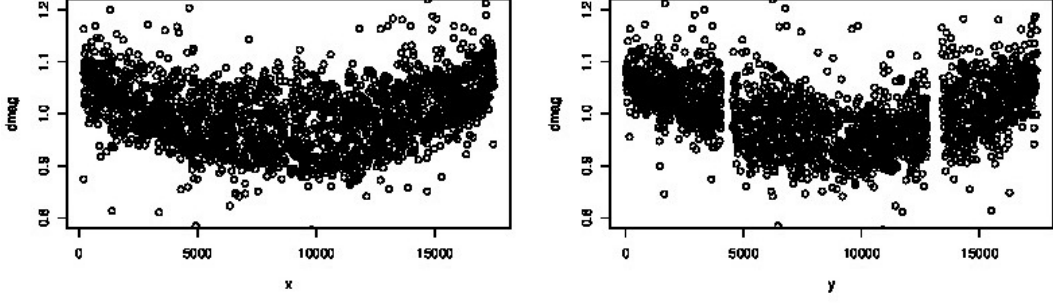


Fig. A.1. Differences of magnitude among observed and SDSS DR8 equatorial stars as a function of x and y pixel coordinates.

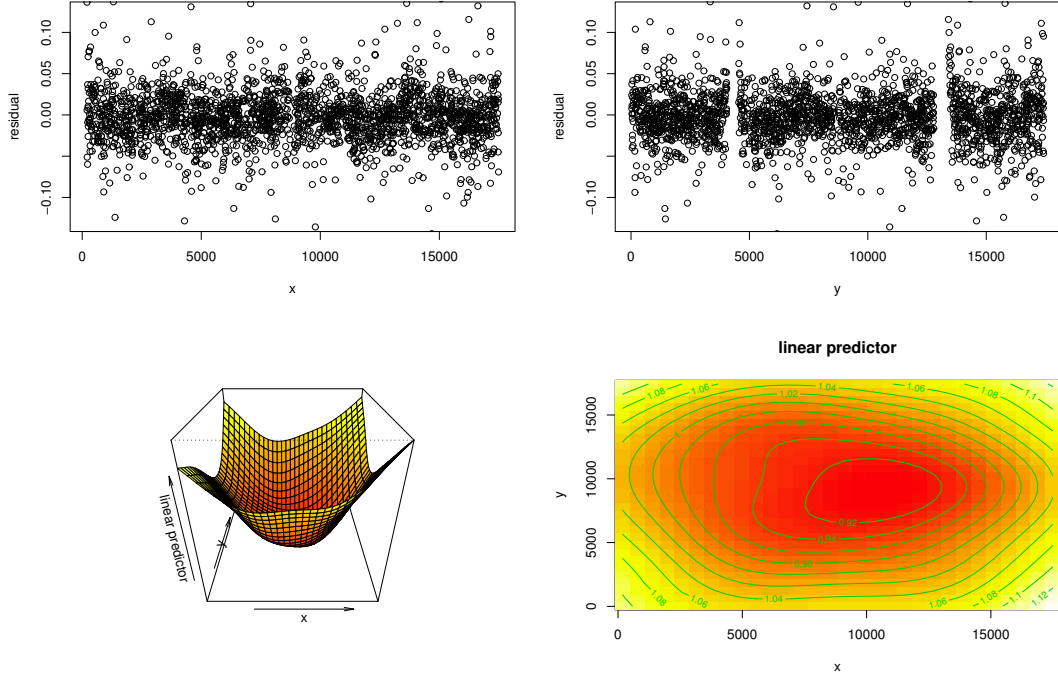


Fig. A.2. Differences of magnitude among observed and SDSS DR8 equatorial stars as a function of x and y pixel coordinates after applying the surface fit (top). *Bottom right panel:* contour plot of the IC image. *Bottom left panel:* IC 3D view.

To extend the PSF beyond the observational limits, we adopted the polynomial expansion of Capaccioli & de Vaucouleurs (1983), which was used to interpolate the total PSF profile (see Fig. B.1):

$$PSF = c_0 + \sum_{i=1}^3 c_i (\log r)^i, \quad (\text{B.1})$$

where $c_0 = 2.187 \times 10^{-6}$ (mag/arcsec²), $c_1 = 1.725 \times 10^{-5}$, $c_2 = -8.559 \times 10^{-6}$ and $c_3 = 1.570 \times 10^{-6}$ for the g band and $c_0 = -9.497 \times 10^{-4}$ (mag/arcsec²), $c_1 = 2.109 \times 10^{-3}$, $c_2 = 1.157 \times 10^{-3}$ and $c_3 = 2.134 \times 10^{-4}$ for the i band. As expected, the g PSF spans a wider range than in the i band. The total integrated energy included in the inner regions, $r^{1/4} \leq 2.3$, is 94 % of the total flux from the stars for the g band.

The expressions B.1 were used to estimate the effect of the scattered light in the outskirts of the galaxies of this study, which have quite different sizes. It is indeed expected that the effect will be quite different at the same surface brightness level between angularly large and small galaxies.

Two methods were employed. The first method is a plain numerical convolution of each galaxy modeled through azimuthally averaged light profiles under the assumptions that the isophotes are ellipses of average flattening and no twisting. At first order, the difference between the model and its convolution provides an estimate of the excess of light in the observed galaxy caused by the broad smearing of the extended PSF.

Another method consists of a straightforward deconvolution of the noiseless model of the galaxy by the extended PSF. To this end, we used the IRAF task LUCY. The two methods provide very consistent results that will be illustrated in a forthcoming paper (Spavone et al., in preparation).

One additional comment is in order about the effect of the background interpolation on the partial removal of the excess of light that is due to PSF scattering. It is expected and verified numerically that small galaxies will be widely broadened by the PSF wings. If this causes the outer light profile to become much flatter, one may expect that the background interpolation procedure is capable of removing part of it, if not all. This is precisely

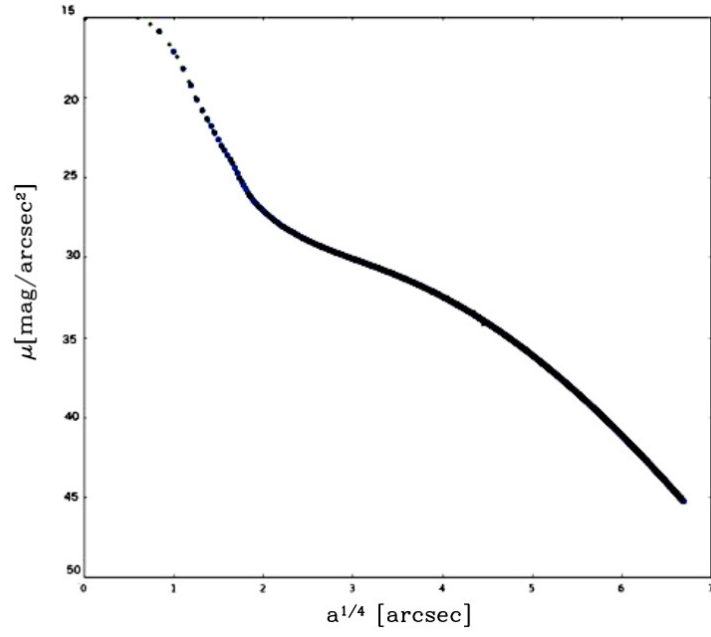


Fig. B.1. Adopted extended PSF for VST.

what our numerical experiments show (Spavone et al., in preparation).

Appendix C: Online tables

Table C.1. The VEGAS sample.

Name	R.A. [deg]	Dec. [deg]	Type	T-type	P.A. [deg]	μ_e [mag/arcsec ²]	B_t [mag]	(B-V) [mag]	σ [km/s]	v [km/s]	ag [mag]	B_{tc} [mag]	M_B [mag]
ESO075-028	21.8495056	-71.4132778	E	-4.8	19.64	21.154	13.389	1.08	205.49	3928	0.117	13.213	-20.425
ESO137-010	16.263925	-60.8030833	E-SO	-3.3	167.73	22.841	12.571	-	215.79	3407.5	1.028	11.491	-21.839
ESO137-045	16.8507634	-60.8087988	E	-4.9	27.47	21.485	13.452	-	210.4	3292.2	1.028	12.374	-20.9
ESO138-005	16.8981651	-58.7781169	E-SO	-3	143.57	21.021	12.838	-	349.44	2632.8	0.577	12.221	-20.549
ESO183-030	18.9488541	-54.5456659	E-SO	-3.3	23.25	20.42	12.619	0.97	172.81	2724.8	0.367	12.211	-20.628
ESO194-021	0.4949153	-51.5206693	E-SO	-3	100.31	20.817	13.612	-	228.59	3439	0.069	13.492	-19.838
ESO270-014	13.4742477	-44.1719654	E-SO	-3.1	33.29	21.474	13.932	1.14	171.8	3871.9	0.535	13.339	-20.323
ESO322-038	12.6384452	-41.5033989	E-SO	-3	84.22	20.721	13.787	-	216.39	3126.3	0.576	13.164	-20.024
ESO322-051	12.681667	-41.6066322	E-SO	-2.8	51.1	20.906	14.026	1.15	205.69	3237.1	0.625	13.353	-19.893
ESO323-015	12.8621611	-38.8291944	E-SO	-3	153.97	21.802	13.91	-	153.54	3058.5	0.362	13.502	-19.626
ESO423-024	5.5780811	-29.2322714	SO	-2.1	-9	20.712	13.213	-	176.01	3937.3	0.111	13.043	-20.619
ESO428-011	7.2586941	-29.3589361	E-SO	-3.1	23.25	21.197	12.94	1.05	170.16	2115.7	0.812	12.097	-20.157
ESO499-023	9.9404727	-26.0949238	E-SO	-3.2	102.03	20.674	12.925	-	213.6	2512	0.307	12.58	-20.118
ESO507-021	12.8412924	-26.8425635	E-SO	-2.5	27.57	20.964	13.396	-	202.71	3167.6	0.333	13.015	-20.231
ESO507-025	12.8588463	-26.4521027	E-SO	-3	99.37	21.186	12.612	1	260.24	3235.3	0.387	12.177	-21.125
ESO567-051	10.3340084	-21.5186201	E	-4.5	170.55	21.145	14.159	0.96	151.81	3706.1	0.234	13.87	-19.72
IC1459	22.9529445	-36.4621765	E	-4.8	43.1	20.62	10.949	0.98	306.1	1794.5	0.071	10.852	-21.064
IC2311	8.3127802	-25.3695888	E	-4.8	-9	21.324	12.494	1.01	224.35	1844	0.622	11.844	-20.124
IC2552	10.1794778	-34.8447266	E-SO	-2.8	89.29	21.803	13.085	1.03	159.5	3113.9	0.518	12.521	-20.638
IC2586	10.5173341	-28.7165771	E	-4.9	85.13	21.389	13.564	1	346.02	3673.3	0.272	13.237	-20.304
IC2594	10.6011578	-24.3230111	E-SO	-3	111.53	21.696	13.499	-	216.74	3546.9	0.266	13.18	-20.31
IC2597	10.6298222	-27.0812518	E	-3.9	7.99	21.841	12.924	1	257.97	2995.2	0.306	12.573	-20.525
IC3370	12.4603126	-39.3379207	E	-4.9	52.86	21.747	11.997	0.97	204.49	2937.5	0.401	11.552	-21.484
IC3896	12.9453372	-50.3467167	E	-4.8	6.36	21.903	12.172	1.17	203.29	2052.5	0.914	11.226	-20.936
IC4197	13.1345203	-23.7969418	E-SO	-3.1	162.33	21.164	13.546	1.07	185.99	3013.2	0.628	12.873	-20.286
IC4296	13.6108474	-33.9658219	E	-4.9	41.57	21.785	11.576	1.01	332.81	3781.4	0.276	11.244	-22.395
IC4421	14.4753451	-37.5835389	E	-4.7	164.35	21.367	13.391	1.02	202.28	3636.4	0.347	12.989	-20.551
IC4797	18.9415806	-54.3058612	E	-3.9	148.1	20.467	12.263	1.01	212.13	2715.3	0.336	11.887	-20.953
IC4889	19.7542178	-54.3442167	E	-4.7	2.03	20.529	12.058	0.95	181.88	2554.2	0.229	11.791	-20.907
IC4943	20.1078543	-48.3756503	E	-4.9	-9	21.043	13.622	0.95	165.25	2913.6	0.216	13.363	-19.642
IC5011	20.4760662	-36.0272354	SO	-2	17.77	20.043	12.683	-	212.81	2289.9	0.184	12.465	-20.042
IC5063	20.8673137	-57.0688469	SO-a	-1.2	119.98	21.984	12.962	1.02	160.91	3383.1	0.267	12.644	-20.686
IC5181	22.2226958	-46.0176284	SO	-2	73.1	19.507	12.464	0.97	-	1980.4	0.086	12.349	-19.766
IC5250A	22.7881584	-65.0608292	E-SO	-2.8	-9	21.897	12.706	-	190	3581	0.141	12.512	-20.926
IC5267	22.953758	-43.3960525	SO-a	-1.1	137.55	21.612	11.391	0.89	-	1714.9	0.054	11.311	-20.443
IC5328	23.5545553	-45.0160034	E	-4.2	40.87	21.144	12.268	0.96	195.43	3138	0.064	12.157	-21.002
NGC0474	1.3351857	3.4153385	SO	-2	-9	21.979	12.383	0.86	157.12	2371.6	0.15	12.197	-20.463
NGC0584	1.5224182	-6.8680509	E	-4.7	104.48	20.364	11.326	0.96	199.34	1849.8	0.183	11.114	-20.953
NGC0636	1.6518172	-7.5125923	E	-4.9	5.84	20.801	12.351	0.95	165.06	1854.7	0.109	12.214	-19.853
NGC0720	1.8834808	-13.7385764	E	-4.9	141.9	20.921	11.148	0.98	241.14	1717.3	0.069	11.053	-20.81
NGC0731	1.915624	-9.0108753	E	-4.1	155.5	21.032	13.069	0.93	157.22	3881.2	0.094	12.916	-20.793
NGC0936	2.4603827	-1.1559362	SO-a	-1.2	132.45	21.368	11.195	0.97	179.33	1368.2	0.153	11.022	-20.367
NGC1052	2.6846621	-8.2558045	E	-4.7	109.01	21.055	11.454	0.94	213.31	1483.8	0.115	11.316	-20.201
NGC1162	2.982225	-12.3985278	E	-4.9	-9	-9	13.806	-	194.85	3936.2	0.205	13.542	-20.168
NGC1199	3.0606951	-15.6138377	E	-4.8	47.67	21.69	12.388	1.02	203.87	2681.6	0.24	12.109	-20.731
NGC1201	3.0688995	-26.0696616	E-SO	-2.6	8.08	20.67	11.703	0.94	163.82	1680.3	0.067	11.61	-20.087
NGC1209	3.1008348	-15.6112629	E	-4.5	83.25	20.623	12.35	0.96	229.75	2641	0.16	12.151	-20.654
NGC1316	3.3782565	-37.2082112	SO	-1.8	49.65	-9	9.409	0.89	224.54	1788.3	0.091	9.292	-22.517
NGC1332	3.4381105	-21.3352765	E-SO	-2.9	121.49	20.127	11.198	0.96	320.86	1526.2	0.14	11.035	-20.483
NGC1340	3.4721166	-31.0681243	E	-4	167.2	-9	11.218	0.88	166.02	1183.1	0.079	11.121	-19.662
NGC1380	3.6076629	-34.9761257	SO	-2.3	6.23	-9	10.896	0.94	211.01	1874.1	0.073	10.795	-21.121
NGC1387	3.6158538	-35.5066275	E-SO	-2.8	-9	20.549	11.772	0.99	170.22	1260.5	0.054	11.699	-19.252
NGC1395	3.6415799	-23.0274642	E	-4.9	104.5	21.371	10.601	0.96	244.67	1701.4	0.1	10.476	-21.278
NGC1399	3.641408	-35.4506257	E	-4.6	-9	-9	10.426	0.96	336.04	1425.7	0.055	10.35	-20.902
NGC1400	3.6585692	-18.6881481	E	-3.7	42.93	21.09	11.933	0.96	251.52	589.9	0.28	11.644	-20.436
NGC1404	3.6477546	-35.5942446	E	-4.8	163.3	-9	10.891	0.97	228.35	1946.3	0.049	10.812	-21.206
NGC1407	3.6699637	-18.5803554	E	-4.5	-9	22.053	10.701	1.03	270.65	1791.4	0.296	10.378	-21.485
NGC1426	3.7136417	-22.1083611	E	-4.9	112.49	21.291	12.271	0.9	150.74	1444.7	0.071	12.179	-19.21
NGC1427	3.7053874	-35.3927754	E	-4	77.85	-9	11.777	0.91	155.99	1388.2	0.051	11.705	-19.476

Table C.1. continued.

Name	R.A. [deg]	Dec. [deg]	Type	T-type	P.A. [deg]	μ_e [mag/arcsec ²]	B_t [mag]	(B-V) [mag]	σ [km/s]	v [km/s]	ag [mag]	B_{tc} [mag]	M_B [mag]
NGC1439	3.7472206	-21.9207205	E	-4.8	-9	21.971	12.29	0.88	150.85	1667.9	0.125	12.141	-19.557
NGC1453	3.7742559	-3.968888	E	-4.7	19	21.556	12.586	1.05	331.89	3906.6	0.456	12.071	-21.638
NGC1537	4.2279746	-31.6452899	E	-3.6	102.31	20.539	11.472	0.89	159.3	1406.8	0.104	11.347	-19.905
NGC1549	4.2625382	-55.5922874	E	-4.3	138.25	21.092	10.678	0.93	202.69	1243.4	0.053	10.606	-20.177
NGC1550	4.3272	2.4098611	E	-4.1	27.75	22.156	13.163	1.08	307.97	3785.2	0.576	12.53	-21.132
NGC1553	4.2695796	-55.780024	S0	-2.3	150.1	20.906	10.285	0.88	177.25	1148.4	0.064	10.203	-20.398
NGC1587	4.5110844	0.6616683	E	-4.8	72.82	21.531	12.721	1.02	227.14	3671.7	0.311	12.355	-21.235
NGC1588	4.5121711	0.6647302	E	-4.8	164.55	21.39	13.893	0.98	152.53	3484.9	0.309	13.532	-19.932
NGC1596	4.460582	-55.027671	S0	-2	19.23	19.872	12.009	0.94	172.02	1511.4	0.042	11.944	-19.377
NGC1700	4.9489833	-4.8659744	E	-4.7	86.97	20.421	12.03	0.97	238.71	3891.4	0.187	11.784	-21.925
NGC1726	4.9949816	-7.7553421	S0	-2.4	0.5	21.531	12.679	0.98	247.72	3991.3	0.303	12.316	-21.439
NGC1993	5.5904361	-17.8152222	E-S0	-3.2	77.35	21.134	13.621	-	150.51	3140.3	0.295	13.279	-19.909
NGC2073	5.7649753	-21.9990983	E-S0	-3	-9	21.017	13.454	-	152.78	2983.8	0.128	13.282	-19.785
NGC2089	5.7976106	-17.6024234	E-S0	-2.9	41.75	20.44	13.04	-	206.01	3001.4	0.287	12.708	-20.359
NGC2217	6.3610332	-27.2336632	S0-a	-0.6	-9	21.966	11.633	1	220.83	1617	0.187	11.422	-20.157
NGC2271	6.7147194	-23.4759167	E-S0	-3.1	78.49	21.947	13.201	-	228.16	2596	0.507	12.654	-20.079
NGC2293	6.7951824	-26.7539001	S0-a	-1	129.8	22.023	12.233	1.07	262.62	2037	0.517	11.685	-20.477
NGC2305	6.8103583	-64.2733333	E	-4.9	137.24	21.08	12.757	1.02	246.92	3570	0.332	12.372	-21.013
NGC2325	7.04455	-28.69725	E	-4.8	4.2	22.772	12.298	-	183.57	2157.2	0.498	11.768	-20.53
NGC2380	7.3985	-27.5291	S0	-2	-9	21.364	12.291	1.05	191	1782	1.331	10.934	-20.929
NGC2434	7.5808894	-69.2842123	E	-4.8	139.56	21.553	12.338	1.07	186.89	1449.7	1.069	11.247	-19.934
NGC2663	8.7522889	-33.79475	E	-4.9	110.6	22.45	11.89	-	292	2156	1.559	10.299	-21.999
NGC2695	8.9075195	-3.0670221	S0	-2.2	160.55	20.946	12.843	0.95	199.85	1834.3	0.076	12.74	-19.327
NGC2822	9.2305596	-69.6448861	E	-4.5	93.8	21.485	11.557	-	156.32	1614.9	0.414	11.119	-20.335
NGC2865	9.3917154	-23.1616091	E	-4.2	154.64	20.2	12.446	0.91	171.96	2722.1	0.361	12.045	-20.828
NGC2887	9.3900028	-63.8125833	E-S0	-3.1	79.87	21.791	12.763	1.1	281.95	2874.5	0.983	11.737	-21.17
NGC2902	9.5146999	-14.7358814	S0	-2	21.78	20.766	13.237	-	-	1993.1	0.283	12.923	-19.285
NGC2904	9.5047205	-30.3849959	E-S0	-3	89.13	21.362	13.52	1.06	234.45	2371.4	0.566	12.919	-19.628
NGC2974	9.709242	-3.698761	E	-4.3	43.99	21.095	11.876	1	237.13	1891.4	0.235	11.613	-20.549
NGC2983	9.7280895	-20.4772017	S0-a	-0.8	86.42	-9	12.736	0.985	173.16	2029.9	0.261	12.446	-19.763
NGC2986	9.7377826	-21.2781478	E	-4.7	-9	21.479	11.692	0.97	259.17	2326.1	0.252	11.405	-21.141
NGC3078	9.973478	-26.9262608	E	-4.8	177.2	21.084	12.067	1.01	252.65	2563.6	0.31	11.719	-21.015
NGC3082	9.9814223	-30.3577716	E-S0	-2.8	28.7	20.239	13.576	-	191.73	2805.9	0.345	13.189	-19.751
NGC3087	9.9857443	-34.2251812	E	-4.3	46.05	20.623	12.63	1.05	184	2636.7	0.464	12.127	-20.643
NGC3091	10.0039505	-19.6362038	E	-4.8	144.43	21.742	12.126	1	321.37	3809	0.188	11.881	-21.757
NGC3100	10.0113312	-31.6642967	S0	-2	148.22	21.846	12.031	0.89	199.92	2583.6	0.323	11.67	-21.064
NGC3108	10.0414028	-31.6774686	S0-a	-1.1	58.71	21.713	12.756	1.03	203.62	2669.1	0.343	12.373	-20.432
NGC3115	10.0872139	-7.7185556	E-S0	-2.9	42.51	19.537	10.082	0.97	261.08	648.6	0.201	9.871	-19.939
NGC3136	10.0967083	-67.3779722	E	-4.9	27.24	21.442	11.697	1.01	228.88	1706	1.037	10.634	-21.005
NGC3136B	10.17025	-67.0050833	E	-3.7	23.25	21.844	12.774	0.98	172.82	1782.9	0.862	11.885	-19.869
NGC3250	10.4422974	-39.9439207	E	-4.9	139.67	20.971	12.162	1.05	267.08	2816.6	0.455	11.664	-21.243
NGC3258	10.4815547	-35.6053845	E	-4.3	67.34	21.863	12.502	1.01	263.27	2800.1	0.349	12.111	-20.796
NGC3260	10.4851259	-35.5951366	E	-4.9	9.08	20.741	13.733	1.06	204.46	2427.7	0.366	13.33	-19.255
NGC3268	10.5001969	-35.3255622	E	-4.3	70.82	22.048	12.324	1.05	230.41	2798.6	0.444	11.838	-21.069
NGC3271	10.5072837	-35.3586217	S0	-1.8	109.24	21.003	12.822	1.09	255.26	3800.7	0.472	12.294	-21.321
NGC3305	10.6032811	-27.1622212	E	-4.9	-9	20.729	13.748	1.02	221.96	3933.7	0.339	13.35	-20.359
NGC3308	10.6062169	-27.4378684	E-S0	-3	34.4	22.229	13.39	1.03	189.66	3555.2	0.338	12.999	-20.491
NGC3311	10.6118836	-27.5278788	E-S0	-3.3	-9	23.867	12.799	1	185.17	3835.5	0.344	12.397	-21.265
NGC3315	10.6220067	-27.1912561	E-S0	-2.9	-9	21.866	14.361	1.05	179.47	3755.8	0.353	13.951	-19.663
NGC3497	11.1216884	-19.4715273	S0	-1.8	56.67	-9	12.996	-	224.46	3701	0.173	12.767	-20.823
NGC3557	11.166028	-37.539245	E	-4.9	32.4	21.105	11.405	1.03	267.72	3056.9	0.436	10.924	-22.205
NGC3585	11.2214178	-26.754864	E	-4.8	103.97	20.928	10.819	0.97	205.67	1373.4	0.276	10.522	-20.8
NGC3606	11.2710034	-33.8274951	E	-4.8	-9	20.571	13.399	-	208.18	3000.6	0.322	13.032	-20.066
NGC3640	11.3519162	3.234786	E	-4.9	97.5	21.095	11.331	0.92	192.27	1315.2	0.185	11.127	-20.327
NGC3706	11.4956778	-36.3912997	E-S0	-3.2	78.38	21.116	12.352	1.04	270.27	2979.6	0.406	11.902	-21.166
NGC3818	11.6992674	-6.1555814	E	-4.6	95.93	21.452	12.709	0.96	194.78	1696.1	0.156	12.528	-19.44
NGC3904	11.8203344	-29.2768138	E	-4.8	11.35	20.692	11.795	0.98	205.48	1576.1	0.31	11.461	-20.178
NGC3923	11.8504901	-28.8059748	E	-4.8	48	21.553	10.767	1	256.61	1550	0.35	10.394	-21.245
NGC3962	11.9111368	-13.9749309	E	-4.8	10	21.333	11.608	0.95	232.98	1854.5	0.193	11.388	-20.727
NGC4024	11.9753387	-18.3468954	E-S0	-3	63.78	20.882	12.699	0.94	150.57	1690.8	0.182	12.492	-19.372

Table C.1. continued.

Name	R.A. [deg]	Dec. [deg]	Type	T-type	P.A. [deg]	μ_e [mag/arcsec ²]	B_I [mag]	(B-V) [mag]	σ [km/s]	v [km/s]	ag [mag]	B_{Ic} [mag]	M_B [mag]
NGC4105	12.11134	-29.7602517	E	-4.7	136.43	21.548	11.567	0.95	261.81	1873.4	0.269	11.27	-20.797
NGC4179	12.2144722	1.2996667	S0	-1.9	146.98	20.656	11.839	0.92	168.93	1261.7	0.143	11.677	-19.712
NGC4373	12.4216498	-39.7596561	E-S0	-3.3	53.87	21.529	11.904	0.98	247.52	3421.8	0.331	11.522	-21.863
NGC4546	12.5915281	-3.7932771	E-S0	-2.7	89.68	20.654	11.353	0.98	195.22	1054.2	0.146	11.191	-19.839
NGC4636	12.7137983	2.6876184	E	-4.8	149.65	-9	10.429	0.94	200.04	925.3	0.124	10.291	-20.492
NGC4643	12.7222582	1.9782772	S0-a	-0.6	131.66	20.484	11.674	0.96	150.1	1329.1	0.132	11.52	-19.998
NGC4645	12.7361061	-41.7499317	E	-3.9	46.21	21.089	12.891	1.06	188.92	2613.3	0.591	12.261	-20.509
NGC4645B	12.7253256	-41.3624578	S0	-2	157.9	21.285	13.48	-	183.84	2308.2	0.815	12.631	-19.836
NGC4696	12.8136889	-41.3111281	E	-3.8	87.79	-9	11.654	-	256.08	2973.9	0.483	11.127	-21.941
NGC4696B	12.789364	-41.2375561	E-S0	-2.9	40.15	20.559	13.786	1.08	243.62	2831.8	0.503	13.241	-19.699
NGC4697	12.8099705	-5.8006924	E	-4.5	83.07	21.664	10.25	0.91	168.12	1240.5	0.128	10.104	-21.218
NGC4751	12.8807793	-42.6600013	E-S0	-2.8	174.58	21.386	13.095	-	349.18	2101.9	0.522	12.541	-19.712
NGC4767	12.8980417	-39.7143333	E	-4	141	21.184	12.52	1.04	212.57	3060	0.464	12.01	-21.118
NGC4783	12.9101591	-12.5583986	E	-4.9	133.5	21.474	12.825	-	265.16	3992.9	0.23	12.535	-21.266
NGC4830	12.9577444	-19.6913076	E-S0	-2.8	164.26	22.237	13.086	1	180.08	3352	0.351	12.684	-20.727
NGC4831	12.9601913	-27.2922281	E-S0	-3.2	176.83	21.338	13.497	-	155.31	3243.3	0.421	13.027	-20.275
NGC4915	13.0244861	-4.5463022	E	-4.7	-9	20.043	12.89	0.89	211.21	3135.5	0.125	12.718	-20.585
NGC4936	13.0713803	-30.5262311	E	-4.8	6.45	22.208	11.976	-	285.45	3095	0.359	11.57	-21.618
NGC4946	13.0915	-43.5910833	E	-3.8	135.06	21.44	13.397	1.05	198.44	3112.6	0.499	12.851	-20.307
NGC4958	13.096928	-8.0201732	S0	-1.9	7.18	19.531	11.49	0.92	156.08	1294.7	0.204	11.267	-20.122
NGC4976	13.14372	-49.5063	E	-4.5	161.2	21.005	10.97	1.01	161.24	1411.5	0.813	10.136	-21.186
NGC4984	13.1492258	-15.516305	S0-a	-0.8	45	19.79	12.198	0.92	-	1214.8	0.267	11.913	-19.268
NGC4993	13.1632522	-23.3838872	E-S0	-3	173.2	20.399	13.452	-	169.48	2951.7	0.534	12.874	-20.254
NGC5011	13.2144109	-43.0961268	E	-4.8	153.97	21.663	12.396	1.02	256.28	3127	0.439	11.91	-21.278
NGC5017	13.2151385	-16.7657761	E	-4.2	28.5	20.482	13.544	0.97	176.85	2529.4	0.358	13.148	-19.657
NGC5018	13.2169453	-19.518201	E	-4.4	99.13	20.342	11.687	0.92	208.19	2843.2	0.412	11.232	-21.804
NGC5044	13.256655	-16.385291	E	-4.8	41	22.813	11.589	1	241.81	2692.9	0.303	11.245	-21.695
NGC5061	13.3014199	-26.8370999	E	-4.3	108.55	20.444	11.209	0.92	185.8	2031	0.297	10.882	-21.372
NGC5077	13.3254466	-12.6565178	E	-4.8	4.18	21.123	12.328	1.03	257.63	2828.7	0.212	12.074	-20.993
NGC5084	13.3380211	-21.8272255	S0	-2	80.4	22.64	11.599	1.11	202.77	1721.3	0.506	11.067	-20.85
NGC5087	13.3402759	-20.6110916	E-S0	-2.9	5.94	20.651	12.228	1.01	282.8	1814.2	0.447	11.754	-20.313
NGC5090	13.3535811	-43.7046333	E	-4.9	105.91	22.041	12.562	-	268.68	2946	0.614	11.904	-21.132
NGC5114	13.4004778	-32.3438288	E-S0	-3.1	77.51	20.788	13.641	-	200.47	3674.3	0.207	13.379	-20.186
NGC5140	13.4393684	-33.8685154	E-S0	-3	46.93	21.731	12.851	-	194.95	3866.7	0.247	12.546	-21.139
NGC5193	13.5315347	-33.2339269	E	-4.1	-9	21.472	12.579	0.93	205.67	3733.9	0.246	12.276	-21.338
NGC5266	13.7172545	-48.1693386	S0	-2.5	97.52	21.951	12.053	-	201.36	3006.3	0.384	11.624	-21.443
NGC5304	13.833746	-30.5784422	E-S0	-3.2	140.02	21.65	13.619	-	211.01	3774.7	0.241	13.322	-20.317
NGC5493	14.1914944	-5.0436389	S0	-2.1	-9	20.442	12.289	0.87	204.05	2695.5	0.154	12.094	-20.911
NGC5576	14.3510283	3.2710301	E	-4.8	89.66	20.585	11.789	0.89	184.27	1506.7	0.133	11.634	-20.23
NGC5638	14.4945621	3.2332952	E	-4.8	154.71	21.429	12.156	0.94	161.92	1657.4	0.141	11.99	-20.028
NGC5791	14.9795028	-19.2668765	E	-4.2	171.63	21.133	12.698	1.01	252.01	3346.8	0.392	12.256	-21.156
NGC5796	14.9900088	-16.6239335	E	-4.7	89.73	21.094	12.729	1.07	273.17	2910.3	0.451	12.234	-20.894
NGC5812	15.0154681	-7.4572376	E	-4.8	73.37	21.219	12.192	1.03	199.61	1917.7	0.374	11.789	-20.509
NGC5813	15.0198046	1.7020095	E	-4.9	142.5	22.337	11.517	0.99	238.27	1955.8	0.246	11.242	-21.142
NGC5831	15.0685994	1.2199386	E	-4.8	128.71	21.585	12.437	0.97	164.07	1630.9	0.253	12.159	-19.859
NGC5838	15.0906396	2.0994875	E-S0	-2.7	38.75	20.767	11.786	0.98	276.8	1252.1	0.23	11.537	-19.917
NGC5846	15.1081241	1.6062912	E	-4.7	-9	22.042	11.091	1.01	236.81	1749	0.241	10.824	-21.338
NGC5846A	15.108091	1.5949712	E	-4.3	111.67	-9	12.721	-	221.98	2309.9	0.242	12.445	-20.253
NGC5869	15.163722	0.4701069	S0	-2.2	110.7	21.624	13.148	0.96	167.78	2074	0.236	12.881	-19.626
NGC5898	15.3037785	-24.0980507	E	-4.3	50.75	21.236	12.438	1.06	206.88	2127.4	0.626	11.78	-20.646
NGC5903	15.3101444	-24.0685833	E	-4.8	164.34	22.059	12.215	1.01	206.54	2561.6	0.655	11.521	-21.318
NGC6305	17.300247	-59.1719975	E-S0	-2.9	136.7	20.401	13.22	1.07	155.12	2677.2	0.44	12.74	-20.065
NGC6758	19.2311953	-56.3095216	E	-4.2	110.85	21.325	12.606	1.04	241.89	3484.6	0.286	12.268	-21.143
NGC6799	19.5379184	-55.9080055	E-S0	-3.5	106.7	21.536	13.509	-	150.64	3413.5	0.267	13.192	-20.166
NGC6851	20.0595516	-48.2845444	E	-4.5	160.87	20.553	12.689	0.91	228.49	3049.5	0.203	12.439	-20.689
NGC6861	20.122079	-48.3702995	E-S0	-2.7	133.11	20.455	12.077	1.01	414	2823.9	0.234	11.8	-21.14
NGC6868	20.1650169	-48.3794926	E	-4.9	80.83	21.451	11.671	1.01	255.04	2949.3	0.24	11.386	-21.65
NGC6875	20.2201365	-46.1617223	E-S0	-2.6	22.06	20.394	12.984	0.95	-	3121.4	0.171	12.767	-20.392
NGC6876	20.3052897	-70.8590603	E	-4.9	110.19	22.036	11.943	-	233.44	3868.9	0.194	11.691	-21.923
NGC6893	20.3471223	-48.2393344	S0	-2	8.63	20.909	12.747	0.98	-	3056	0.173	12.528	-20.6

Table C.1. continued.

Name	R.A. [deg]	Dec. [deg]	Type	T-type	P.A. [deg]	μ_e [mag/arcsec ²]	B_t [mag]	(B-V) [mag]	σ [km/s]	v [km/s]	ag [mag]	B_{tc} [mag]	M_B [mag]
NGC6903	20.3958003	-19.3254017	E-S0	-3.3	-9	22.062	12.9	-	226.61	3292.3	0.289	12.562	-20.822
NGC6920	20.7325936	-80.0008073	S0	-2	131.52	20.861	13.193	1.22	234.96	2634.8	1.032	12.121	-20.577
NGC6942	20.6771732	-54.3030482	S0-a	-0.3	134.28	22.719	12.969	-	-	3274	0.205	12.688	-20.558
NGC6958	20.8118337	-37.9973321	E	-3.7	97.42	20.842	12.284	0.91	187.77	2719.5	0.195	12.048	-20.826
NGC6964	20.7900844	0.3008814	E	-4.5	164.5	20.686	13.954	1.01	206.61	3791.5	0.426	13.472	-20.261
NGC7020	21.1889168	-64.0253426	S0-a	-1.2	165.27	22.096	12.693	0.95	195.43	3153	0.17	12.475	-20.653
NGC7029	21.1978029	-49.2837797	E	-4.6	67.61	20.71	12.395	0.89	185.01	2804.1	0.16	12.193	-20.715
NGC7041	21.2756582	-48.3635931	E-S0	-3	83.61	20.731	12.102	0.91	225.52	1945.6	0.169	11.904	-20.163
NGC7049	21.3167278	-48.5608333	S0	-1.9	63.72	21.086	11.676	1.05	246.48	2261.8	0.243	11.399	-21.026
NGC7079	21.5431359	-44.0675693	S0	-1.8	76.69	20.763	12.485	0.87	158.9	2653.5	0.137	12.308	-20.496
NGC7097	21.6702463	-42.5394127	E	-4.9	17.17	20.724	12.611	0.91	221.85	2602.1	0.086	12.486	-20.283
NGC7135	21.8294475	-34.876334	E-S0	-2.9	44.87	22.791	12.794	0.99	-	2718	0.123	12.63	-20.243
NGC7144	21.8784659	-48.2539237	E	-4.8	-9	21.371	11.687	0.92	174.03	1924.4	0.089	11.569	-20.449
NGC7166	22.0091491	-43.389778	E-S0	-2.9	10.21	20.573	13.033	0.99	-	2451.6	0.066	12.93	-19.693
NGC7168	22.0353944	-51.7431111	E	-4.8	69.4	20.964	12.834	0.93	180.17	2846	0.1	12.691	-20.249
NGC7173	22.034261	-31.9737228	E	-4.3	140.54	22.144	12.905	0.92	203.86	2497.2	0.115	12.752	-19.945
NGC7176	22.0356785	-31.9900967	E	-4.8	75.1	21.549	12.434	-	253.84	2515.4	0.115	12.282	-20.416
NGC7192	22.1139243	-64.3161871	E	-4	-9	21.44	12.202	0.95	178.6	2959.5	0.147	12.011	-20.962
NGC7196	22.0985626	-50.1190894	E	-4.8	58.52	20.734	12.366	0.94	278.92	2886.5	0.095	12.227	-20.746
NGC7200	22.1193075	-49.995513	E	-3.7	44.89	20.759	13.774	0.91	194.45	2907.9	0.084	13.647	-19.326
NGC7216	22.2099498	-68.6619852	E	-4.2	127.41	21.384	13.535	0.95	172.58	3529.7	0.152	13.33	-20.055
NGC7302	22.5399237	-14.1205203	E-S0	-2.8	95.4	20.788	13.151	0.97	150.61	2671.5	0.309	12.802	-20.105
NGC7391	22.8433537	-1.5447783	E	-4.9	96.32	21.331	13.117	1.07	243.84	3045.4	0.416	12.655	-20.591
NGC7484	23.1180401	-36.2753442	E	-4.8	-9	21.908	12.981	-	193.19	2738.1	0.074	12.866	-20.007
NGC7507	23.2021016	-28.5396671	E	-4.5	-9	20.384	11.378	0.98	222.37	1606.6	0.213	11.14	-20.557
NGC7585	23.3003716	-4.6504582	S0-a	-1.1	94.86	21.323	12.445	0.9	214.25	3458	0.232	12.162	-21.328
NGC7600	23.3149747	-7.5805507	E-S0	-2.9	62.34	21.187	12.908	0.96	210.2	3441.5	0.141	12.716	-20.748
NGC7676	23.4838058	-59.7167044	E-S0	-3.3	86.18	20.301	13.539	0.98	198.52	3367.2	0.068	13.42	-19.854
NGC7702	23.5913627	-56.0122925	S0-a	-1.1	118.07	21.423	13.067	0.92	-	3227.3	0.071	12.948	-20.241
NGC7744	23.7497847	-42.9096325	E-S0	-2.5	108.55	20.634	12.797	0.95	-	3091.8	0.063	12.687	-20.441
NGC7796	23.9832784	-55.4583824	E	-4	177.96	21.203	12.44	0.97	258.84	3342.4	0.045	12.345	-20.93

Notes. Column1: Object name. Column 2: Right ascension. Column 3: Declination. Column 4: Morphological type. Column 5: Morphological type code. Column 6: Position angle. Column 7: Mean effective surface brightness. Column 8: Total B-magnitude. Column 9: Total (B-V) color. Column 10: Central velocity dispersion. Column 11: Mean Heliocentric radial velocity (cz). Column 12: Galactic extinction in B-band. Column 13: Total B-magnitude. Column 14: Absolute B-band magnitude.

Table C.2. Surface photometry of NGC 4472.

$a_g^{1/4}$	μ_g	$\sigma(\mu_g)$	ϵ_g	$P.A._g$	$a_i^{1/4}$	μ_i	$\sigma(\mu_i)$	ϵ_i	$P.A._i$
[arcsec]	[mag/arcsec ²]	[mag/arcsec ²]		[deg]	[arcsec]	[mag/arcsec ²]	[mag/arcsec ²]		[deg]
0.000	16.64	0.013	0.202	0.49	0.000	15.34	0.009	0.145	-88.83
0.586	16.64	0.007	0.202	0.49	0.586	15.34	0.006	0.145	-88.83
0.613	16.65	0.007	0.204	0.75	0.613	15.35	0.006	0.146	-88.53
0.642	16.65	0.007	0.205	1.05	0.642	15.35	0.006	0.149	-88.00
0.672	16.65	0.007	0.206	1.34	0.672	15.35	0.006	0.153	-87.54
0.703	16.65	0.007	0.098	2.83	0.703	15.35	0.006	0.054	-80.71
0.736	16.65	0.007	0.111	10.19	0.736	15.35	0.006	0.044	-31.71
0.769	16.65	0.007	0.143	10.31	0.769	15.36	0.006	0.084	-21.02
0.806	16.66	0.007	0.170	10.93	0.806	15.36	0.006	0.132	-21.19
0.843	16.66	0.007	0.132	16.65	0.843	15.37	0.006	0.117	-17.28
0.883	16.67	0.007	0.133	12.79	0.883	15.38	0.006	0.150	-9.12
0.924	16.69	0.006	0.104	3.51	0.924	15.39	0.006	0.125	-7.76
0.967	16.71	0.006	0.099	-2.08	0.967	15.41	0.006	0.113	-12.77
1.012	16.73	0.006	0.092	-7.91	1.012	15.44	0.006	0.107	-13.68
1.059	16.77	0.006	0.076	-15.60	1.059	15.48	0.006	0.102	-13.98
1.109	16.82	0.006	0.073	-14.93	1.109	15.54	0.006	0.093	-16.18
1.161	16.89	0.006	0.065	-14.46	1.161	15.61	0.006	0.086	-15.95
1.215	16.98	0.006	0.061	-13.29	1.215	15.70	0.006	0.075	-15.39
1.271	17.08	0.006	0.061	-14.13	1.271	15.81	0.006	0.072	-15.47
1.331	17.20	0.007	0.048	-18.52	1.331	15.94	0.006	0.057	-20.40
1.393	17.34	0.007	0.053	-19.67	1.393	16.08	0.006	0.061	-18.07
1.458	17.50	0.007	0.060	-16.03	1.458	16.25	0.006	0.061	-20.55
1.526	17.68	0.007	0.067	-19.40	1.526	16.43	0.006	0.072	-22.06
1.597	17.87	0.007	0.074	-18.72	1.597	16.62	0.006	0.083	-20.66
1.671	18.07	0.007	0.093	-18.65	1.671	16.83	0.006	0.099	-21.89
1.749	18.27	0.007	0.109	-20.60	1.749	17.04	0.006	0.110	-20.69
1.831	18.49	0.007	0.123	-19.96	1.831	17.26	0.006	0.126	-20.61
1.916	18.72	0.007	0.142	-20.04	1.916	17.49	0.006	0.145	-20.81
2.006	18.94	0.007	0.163	-21.18	2.006	17.71	0.006	0.162	-21.34
2.099	19.17	0.007	0.175	-21.11	2.099	17.95	0.007	0.174	-21.12
2.197	19.42	0.007	0.175	-20.81	2.197	18.20	0.007	0.176	-20.81
2.299	19.70	0.007	0.172	-20.92	2.299	18.48	0.007	0.175	-21.63
2.407	20.01	0.008	0.164	-20.88	2.407	18.79	0.007	0.166	-21.34
2.519	20.33	0.008	0.160	-21.45	2.519	19.11	0.008	0.160	-22.34
2.636	20.63	0.009	0.164	-21.61	2.636	19.41	0.009	0.163	-22.57
2.759	20.91	0.010	0.170	-22.30	2.759	19.69	0.010	0.168	-23.01
2.888	21.18	0.011	0.175	-22.94	2.888	19.96	0.011	0.175	-22.77
3.023	21.46	0.011	0.174	-23.41	3.023	20.23	0.013	0.177	-22.51
3.164	21.79	0.013	0.170	-23.03	3.164	20.55	0.015	0.169	-21.18
3.311	22.16	0.015	0.161	-23.60	3.311	20.90	0.019	0.155	-21.48
3.466	22.54	0.017	0.162	-24.89	3.466	21.26	0.025	0.154	-21.89
3.627	22.88	0.020	0.180	-26.01	3.627	21.60	0.032	0.164	-23.47
3.796	23.20	0.023	0.197	-26.10	3.796	21.91	0.040	0.171	-24.85
3.973	23.52	0.028	0.212	-26.81	3.973	22.24	0.052	0.177	-22.88
4.159	23.91	0.034	0.206	-26.82	4.159	22.60	0.070	0.169	-17.53
4.353	24.32	0.041	0.214	-29.74	4.353	23.05	0.101	0.149	-14.40
4.556	24.79	0.052	0.220	-32.35	4.556	23.53	0.151	0.131	-7.06
4.768	25.29	0.069	0.234	-35.05	4.768	24.06	0.238	0.112	0.38
4.990	25.72	0.091	0.270	-39.20	4.990	24.44	0.332	0.076	-72.85
5.223	26.33	0.133	0.270	-46.22	5.223	25.00	0.543	0.076	-72.85
5.467	26.92	0.194	0.307	-53.26	5.467	25.85	1.154	0.076	-72.85
5.722	27.09	0.218	0.417	-54.40	5.722	25.99	1.304	0.076	-72.85
5.988	27.36	0.265	0.505	-56.16					
6.268	27.44	0.284	0.582	-60.02					
6.560	27.64	0.328	0.644	-63.09					

Notes. Column 1: Semi-major axis in the g band. Column 2: Azimuthally averaged surface brightness in the g band. Column 3: Error on the surface brightness in the g band. Column 4: Ellipticity in the g band. Column 5: Position angle in the g band. Column 6: Semi-major axis in the i band. Column 7: Azimuthally averaged surface brightness in the i band. Column 8: Error on the surface brightness in the i band. Column 9: Ellipticity in the i band. Column 10: Position angle in the i band.

Table C.3. Surface photometry of NGC 4434.

$a_g^{1/4}$	μ_g	$\sigma(\mu_g)$	ϵ_g	$P.A._g$	$a_i^{1/4}$	μ_i	$\sigma(\mu_i)$	ϵ_i	$P.A._i$
[arcsec]	[mag/arcsec ²]	[mag/arcsec ²]		[deg]	[arcsec]	[mag/arcsec ²]	[mag/arcsec ²]		[deg]
0.000	16.62	0.012	0.152	9.65	0.000	15.23	0.006	0.073	9.35
0.586	16.66	0.007	0.152	9.65	0.586	15.29	0.006	0.073	9.35
0.613	16.67	0.007	0.158	11.41	0.613	15.31	0.006	0.076	12.02
0.642	16.68	0.007	0.152	14.85	0.642	15.32	0.006	0.061	18.51
0.672	16.69	0.007	0.152	18.09	0.672	15.34	0.006	0.057	22.38
0.703	16.71	0.007	0.110	28.62	0.703	15.37	0.006	0.039	29.03
0.736	16.75	0.007	0.081	29.59	0.736	15.42	0.006	0.036	36.16
0.769	16.79	0.007	0.087	34.91	0.769	15.48	0.006	0.036	38.35
0.806	16.84	0.007	0.087	37.51	0.806	15.56	0.006	0.041	43.38
0.843	16.92	0.007	0.081	42.76	0.843	15.66	0.006	0.045	46.36
0.883	17.01	0.007	0.081	42.76	0.883	15.78	0.006	0.045	46.36
0.924	17.13	0.007	0.071	44.55	0.924	15.92	0.006	0.053	46.19
0.967	17.27	0.007	0.060	44.37	0.967	16.08	0.006	0.054	45.39
1.012	17.44	0.007	0.048	43.19	1.012	16.26	0.006	0.054	45.86
1.059	17.61	0.007	0.042	41.94	1.059	16.45	0.006	0.049	46.16
1.109	17.81	0.007	0.038	41.43	1.109	16.66	0.006	0.042	40.36
1.161	18.03	0.007	0.036	36.65	1.161	16.90	0.006	0.038	38.19
1.215	18.28	0.007	0.040	34.21	1.215	17.17	0.006	0.039	35.13
1.271	18.55	0.008	0.038	30.97	1.271	17.44	0.006	0.033	36.60
1.331	18.82	0.008	0.042	41.18	1.331	17.72	0.006	0.038	37.22
1.393	19.08	0.008	0.052	40.14	1.393	17.98	0.006	0.050	40.78
1.458	19.34	0.009	0.073	40.14	1.458	18.24	0.006	0.073	38.09
1.526	19.61	0.009	0.097	41.99	1.526	18.51	0.006	0.095	41.85
1.597	19.89	0.009	0.106	42.37	1.597	18.80	0.006	0.099	41.42
1.671	20.24	0.009	0.083	42.37	1.671	19.14	0.006	0.082	41.71
1.749	20.60	0.010	0.067	39.39	1.749	19.52	0.006	0.060	39.33
1.831	20.99	0.010	0.052	39.20	1.831	19.91	0.006	0.049	40.45
1.916	21.34	0.011	0.050	36.01	1.916	20.28	0.006	0.044	35.75
2.006	21.68	0.012	0.043	34.35	2.006	20.63	0.006	0.038	35.75
2.099	22.07	0.014	0.041	29.14	2.099	21.01	0.007	0.034	28.48
2.197	22.51	0.017	0.038	29.87	2.197	21.45	0.007	0.037	28.61
2.299	22.97	0.020	0.050	31.53	2.299	21.92	0.009	0.049	31.82
2.407	23.51	0.028	0.052	38.28	2.407	22.50	0.012	0.050	37.35
2.519	24.18	0.034	0.060	38.24	2.519	23.21	0.021	0.060	42.92
2.636	24.83	0.048	0.071	41.20	2.636	23.95	0.040	0.069	43.85
2.759	25.53	0.067	0.084	42.81	2.759	24.74	0.083	0.088	47.65
2.888	26.18	0.094	0.104	36.10	2.888	25.62	0.185	0.093	58.63
3.023	26.79	0.133	0.151	36.39	3.023	26.29	0.346	0.170	62.97
3.164	27.47	0.194	0.199	36.39	3.164	27.06	0.702	0.206	65.79
3.311	28.95	0.471	0.190	24.26	3.311	27.50	1.047	0.308	65.79

Notes. Column 1: Semi-major axis in the g band. Column 2: Azimuthally averaged surface brightness in the g band. Column 3: Error on the surface brightness in the g band. Column 4: Ellipticity in the g band. Column 5: Position angle in the g band. Column 6: Semi-major axis in the i band. Column 7: Azimuthally averaged surface brightness in the i band. Column 8: Error on the surface brightness in the i band. Column 9: Ellipticity in the i band. Column 10: Position angle in the i band.

Table C.4. Surface photometry of NGC 4464.

$a_g^{1/4}$	μ_g	$\sigma(\mu_g)$	ϵ_g	$P.A._g$	$a_i^{1/4}$	μ_i	$\sigma(\mu_i)$	ϵ_i	$P.A._i$
[arcsec]	[mag/arcsec ²]	[mag/arcsec ²]		[deg]	[arcsec]	[mag/arcsec ²]	[mag/arcsec ²]		[deg]
0.000	16.43	0.012	0.215	7.85	0.000	15.06	0.008	0.319	3.41
0.586	16.48	0.007	0.215	7.85	0.586	15.11	0.006	0.319	3.41
0.613	16.49	0.007	0.223	9.13	0.613	15.12	0.006	0.316	4.25
0.642	16.51	0.007	0.233	10.58	0.642	15.13	0.006	0.313	5.27
0.672	16.52	0.007	0.232	13.37	0.672	15.15	0.006	0.310	6.48
0.703	16.55	0.007	0.165	22.47	0.703	15.18	0.006	0.208	10.08
0.736	16.59	0.007	0.160	20.53	0.736	15.23	0.006	0.145	16.19
0.769	16.64	0.007	0.170	15.65	0.769	15.29	0.006	0.131	12.73
0.806	16.70	0.007	0.183	12.83	0.806	15.37	0.006	0.116	8.37
0.843	16.78	0.007	0.190	11.16	0.843	15.48	0.006	0.111	10.10
0.883	16.90	0.007	0.189	12.93	0.883	15.60	0.006	0.128	9.35
0.924	17.03	0.007	0.190	11.92	0.924	15.75	0.006	0.154	8.08
0.967	17.20	0.007	0.189	9.49	0.967	15.93	0.006	0.168	8.25
1.012	17.37	0.007	0.201	7.12	1.012	16.12	0.006	0.201	6.93
1.059	17.57	0.007	0.207	6.44	1.059	16.33	0.006	0.219	6.77
1.109	17.79	0.007	0.217	5.57	1.109	16.55	0.006	0.240	6.04
1.161	18.02	0.007	0.233	4.80	1.161	16.78	0.006	0.257	5.93
1.215	18.28	0.007	0.248	4.67	1.215	17.04	0.006	0.272	5.55
1.271	18.54	0.008	0.261	4.67	1.271	17.30	0.007	0.279	5.36
1.331	18.82	0.008	0.261	5.10	1.331	17.58	0.007	0.279	5.09
1.393	19.09	0.008	0.269	4.40	1.393	17.87	0.007	0.274	4.14
1.458	19.37	0.009	0.282	5.69	1.458	18.14	0.007	0.286	5.42
1.526	19.67	0.009	0.281	4.92	1.526	18.45	0.007	0.279	4.19
1.597	20.00	0.010	0.275	4.53	1.597	18.77	0.008	0.282	4.10
1.671	20.35	0.010	0.266	4.28	1.671	19.13	0.008	0.267	3.32
1.749	20.75	0.011	0.247	3.28	1.749	19.52	0.008	0.258	2.58
1.831	21.18	0.012	0.232	3.45	1.831	19.96	0.008	0.240	2.59
1.916	21.66	0.013	0.215	3.04	1.916	20.45	0.009	0.224	2.59
2.006	22.18	0.015	0.195	3.22	2.006	20.98	0.010	0.204	2.77
2.099	22.71	0.018	0.181	2.45	2.099	21.52	0.012	0.192	2.70
2.197	23.30	0.024	0.169	1.82	2.197	22.13	0.015	0.178	2.57
2.299	23.92	0.032	0.155	-0.32	2.299	22.80	0.021	0.154	0.56
2.407	24.55	0.042	0.150	-5.82	2.407	23.54	0.030	0.134	-6.03
2.519	25.23	0.058	0.137	-8.26	2.519	24.45	0.049	0.053	-15.97
2.636	25.93	0.083	0.143	-15.71	2.636	25.24	0.079	0.101	-46.77
2.759	26.77	0.130	0.152	-16.62	2.759	26.03	0.131	0.185	-54.86
2.888	27.78	0.237	0.159	-19.04	2.888	26.64	0.198	0.282	-65.85
3.023	29.38	0.625	0.186	-13.70	3.023	27.86	0.478	0.282	-65.85
3.164	30.39	1.256	0.270	-35.14	3.164	28.84	1.025	0.282	-65.85

Notes. Column 1: Semi-major axis in the g band. Column 2: Azimuthally averaged surface brightness in the g band. Column 3: Error on the surface brightness in the g band. Column 4: Ellipticity in the g band. Column 5: Position angle in the g band. Column 6: Semi-major axis in the i band. Column 7: Azimuthally averaged surface brightness in the i band. Column 8: Error on the surface brightness in the i band. Column 9: Ellipticity in the i band. Column 10: Position angle in the i band.

Table C.5. Surface photometry of NGC 4467.

$a_g^{1/4}$	μ_g	$\sigma(\mu_g)$	ϵ_g	$P.A._g$	$a_i^{1/4}$	μ_i	$\sigma(\mu_i)$	ϵ_i	$P.A._i$
[arcsec]	[mag/arcsec ²]	[mag/arcsec ²]		[deg]	[arcsec]	[mag/arcsec ²]	[mag/arcsec ²]		[deg]
0.000	17.96	0.021	0.130	44.73	0.000	16.74	0.013	0.185	29.39
0.572	18.02	0.008	0.130	44.73	0.572	16.78	0.007	0.185	29.39
0.586	18.03	0.008	0.143	44.82	0.586	16.78	0.007	0.195	30.39
0.598	18.03	0.008	0.158	44.88	0.598	16.79	0.007	0.210	30.66
0.615	18.04	0.008	0.174	44.94	0.615	16.79	0.007	0.225	31.26
0.628	18.04	0.008	0.191	44.98	0.628	16.80	0.007	0.240	31.82
0.644	18.05	0.008	0.210	45.02	0.644	16.80	0.007	0.257	32.38
0.659	18.06	0.008	0.230	45.05	0.659	16.81	0.007	0.274	32.98
0.675	18.07	0.008	0.252	45.07	0.675	16.81	0.007	0.293	33.45
0.692	18.07	0.008	0.276	45.08	0.692	16.82	0.007	0.314	33.91
0.709	18.08	0.008	0.293	44.27	0.709	16.83	0.007	0.318	37.46
0.726	18.10	0.008	0.274	43.24	0.726	16.85	0.007	0.255	39.60
0.743	18.13	0.009	0.253	41.08	0.743	16.88	0.007	0.219	39.77
0.760	18.16	0.009	0.230	39.61	0.760	16.91	0.007	0.212	40.61
0.779	18.19	0.009	0.224	38.30	0.779	16.95	0.007	0.210	41.28
0.798	18.23	0.009	0.223	36.90	0.798	16.99	0.007	0.202	42.07
0.817	18.27	0.009	0.219	35.15	0.817	17.03	0.007	0.207	43.50
0.836	18.32	0.009	0.213	34.72	0.836	17.09	0.007	0.217	42.85
0.857	18.37	0.009	0.218	35.82	0.857	17.14	0.007	0.224	44.22
0.877	18.42	0.009	0.225	34.92	0.877	17.20	0.007	0.230	44.90
0.898	18.49	0.009	0.220	36.68	0.898	17.26	0.007	0.236	43.68
0.921	18.56	0.009	0.216	36.81	0.921	17.34	0.007	0.236	43.70
0.943	18.63	0.008	0.222	36.38	0.943	17.42	0.007	0.244	44.20
0.965	18.70	0.008	0.221	37.44	0.965	17.49	0.007	0.253	43.49
0.989	18.79	0.008	0.220	37.54	0.989	17.58	0.007	0.254	42.99
1.012	18.87	0.008	0.224	37.53	1.012	17.67	0.007	0.263	42.82
1.037	18.96	0.008	0.225	37.50	1.037	17.76	0.007	0.270	42.42
1.062	19.04	0.008	0.230	37.11	1.062	17.85	0.007	0.277	41.32
1.087	19.14	0.008	0.238	37.47	1.087	17.94	0.007	0.290	41.13
1.113	19.23	0.008	0.248	37.61	1.113	18.03	0.007	0.301	40.43
1.140	19.33	0.008	0.258	38.08	1.140	18.13	0.007	0.310	40.42
1.168	19.43	0.008	0.265	38.72	1.168	18.23	0.007	0.316	40.17
1.196	19.54	0.008	0.274	38.65	1.196	18.34	0.007	0.322	40.13
1.225	19.65	0.008	0.283	38.86	1.225	18.45	0.007	0.329	40.29
1.254	19.77	0.008	0.290	39.45	1.254	18.57	0.007	0.332	40.32
1.285	19.89	0.008	0.293	39.42	1.285	18.70	0.007	0.329	40.33
1.316	20.02	0.009	0.294	39.45	1.316	18.83	0.007	0.324	40.04
1.347	20.16	0.009	0.293	39.65	1.347	18.98	0.007	0.315	39.80
1.380	20.31	0.009	0.291	39.62	1.380	19.14	0.007	0.309	40.22
1.413	20.48	0.009	0.279	39.64	1.413	19.30	0.007	0.298	39.99
1.447	20.65	0.012	0.270	39.55	1.447	19.48	0.009	0.283	39.94
1.482	20.84	0.013	0.253	39.82	1.482	19.67	0.009	0.266	39.60
1.518	21.03	0.013	0.241	39.82	1.518	19.87	0.009	0.248	40.10
1.554	21.24	0.014	0.219	39.92	1.554	20.08	0.010	0.227	39.61
1.592	21.45	0.016	0.199	39.76	1.592	20.29	0.011	0.204	38.47
1.630	21.66	0.016	0.183	39.76	1.630	20.52	0.011	0.182	39.37
1.670	21.90	0.017	0.158	40.45	1.670	20.76	0.012	0.160	40.69
1.710	22.14	0.018	0.132	40.79	1.710	21.01	0.012	0.135	38.78
1.751	22.40	0.019	0.114	40.68	1.751	21.28	0.013	0.111	40.11
1.793	22.67	0.020	0.097	40.91	1.793	21.57	0.014	0.083	38.47
1.837	22.95	0.022	0.079	40.77	1.837	21.84	0.015	0.078	38.24
1.881	23.25	0.024	0.063	41.35	1.881	22.17	0.016	0.057	40.44
1.926	23.57	0.026	0.045	39.91	1.926	22.49	0.018	0.044	42.22
1.973	23.90	0.031	0.034	37.14	1.973	22.85	0.022	0.033	35.67
2.020	24.27	0.038	0.026	54.38	2.020	23.26	0.027	0.017	61.34
2.069	24.65	0.045	0.024	74.94	2.069	23.67	0.032	0.019	85.44
2.119	25.02	0.053	0.037	85.99	2.119	24.04	0.040	0.029	-82.29
2.170	25.45	0.067	0.044	-83.88	2.170	24.53	0.054	0.035	-63.69
2.222	25.99	0.091	0.038	83.57	2.222	25.19	0.080	0.003	-84.78
2.276	26.62	0.127	0.048	73.55	2.276	26.08	0.141	0.001	-174.80
2.331	27.31	0.186	0.039	73.55	2.331	26.15	0.148	0.105	76.97
2.387	27.36	0.192	0.151	82.69	2.387	26.56	0.195	0.168	87.41
2.444	27.70	0.236	0.213	75.10	2.444	26.89	0.245	0.168	87.41
2.503	28.25	0.324	0.244	84.88	2.503	27.02	0.271	0.168	87.41

Notes. Column 1: Semi-major axis in the g band. Column 2: Azimuthally averaged surface brightness in the g band. Column 3: Error on the surface brightness in the g band. Column 4: Ellipticity in the g band. Column 5: Position angle in the g band. Column 6: Semi-major axis in the i band. Column 7: Azimuthally averaged surface brightness in the i band. Column 8: Error on the surface brightness in the i band. Column 9: Ellipticity in the i band. Column 10: Position angle in the i band.

Table C.6. Surface photometry of VCC 1199.

$a_g^{1/4}$	μ_g	$\sigma(\mu_g)$	ϵ_g	$P.A._g$	$a_i^{1/4}$	μ_i	$\sigma(\mu_i)$	ϵ_i	$P.A._i$
[arcsec]	[mag/arcsec ²]	[mag/arcsec ²]		[deg]	[arcsec]	[mag/arcsec ²]	[mag/arcsec ²]		[deg]
0.000	18.37	0.025	0.112	30.72	0.000	16.90	0.014	0.059	77.81
0.572	18.42	0.009	0.112	30.72	0.572	16.97	0.007	0.059	77.81
0.586	18.42	0.009	0.139	30.72	0.586	16.97	0.007	0.057	76.75
0.598	18.43	0.009	0.139	34.27	0.598	16.98	0.007	0.056	75.66
0.615	18.44	0.009	0.151	34.03	0.615	16.99	0.007	0.054	74.53
0.628	18.44	0.009	0.167	33.85	0.628	17.00	0.007	0.053	73.38
0.644	18.45	0.009	0.182	34.97	0.644	17.01	0.007	0.053	72.21
0.659	18.45	0.009	0.198	35.99	0.659	17.02	0.007	0.053	71.03
0.675	18.46	0.009	0.217	36.85	0.675	17.03	0.007	0.057	69.97
0.692	18.47	0.009	0.238	37.58	0.692	17.05	0.007	0.054	65.10
0.709	18.48	0.009	0.237	39.69	0.709	17.07	0.007	0.044	64.72
0.726	18.50	0.009	0.215	38.95	0.726	17.10	0.007	0.044	53.69
0.743	18.52	0.009	0.192	38.09	0.743	17.14	0.007	0.042	41.89
0.760	18.55	0.009	0.187	38.03	0.760	17.17	0.007	0.052	38.01
0.779	18.58	0.010	0.188	37.64	0.779	17.22	0.007	0.052	38.01
0.798	18.62	0.010	0.191	37.35	0.798	17.26	0.007	0.063	36.03
0.817	18.67	0.010	0.192	36.88	0.817	17.32	0.007	0.062	35.63
0.836	18.71	0.010	0.188	37.46	0.836	17.39	0.007	0.068	41.37
0.857	18.77	0.010	0.197	36.61	0.857	17.45	0.007	0.092	34.81
0.877	18.84	0.010	0.199	33.76	0.877	17.53	0.007	0.099	36.07
0.898	18.91	0.010	0.188	33.70	0.898	17.63	0.007	0.100	37.36
0.921	19.00	0.009	0.184	32.55	0.921	17.71	0.007	0.121	33.66
0.943	19.08	0.009	0.180	31.51	0.943	17.81	0.007	0.128	33.90
0.965	19.18	0.009	0.171	32.58	0.965	17.92	0.007	0.133	34.39
0.989	19.29	0.009	0.162	31.73	0.989	18.03	0.007	0.148	32.59
1.012	19.39	0.009	0.152	31.50	1.012	18.14	0.007	0.158	32.95
1.037	19.51	0.009	0.148	32.07	1.037	18.27	0.007	0.165	33.07
1.062	19.63	0.010	0.147	31.92	1.062	18.39	0.007	0.174	32.26
1.087	19.76	0.010	0.140	31.70	1.087	18.52	0.007	0.174	32.25
1.113	19.90	0.010	0.139	31.74	1.113	18.67	0.007	0.168	31.38
1.140	20.04	0.010	0.143	30.46	1.140	18.82	0.007	0.166	30.08
1.168	20.20	0.010	0.137	31.18	1.168	18.98	0.008	0.158	30.62
1.196	20.37	0.010	0.127	31.30	1.196	19.15	0.008	0.146	31.14
1.225	20.55	0.010	0.119	31.62	1.225	19.33	0.008	0.135	31.05
1.254	20.73	0.011	0.112	31.96	1.254	19.51	0.008	0.127	31.49
1.285	20.92	0.011	0.107	31.70	1.285	19.71	0.008	0.110	31.29
1.316	21.13	0.011	0.088	31.52	1.316	19.91	0.008	0.099	32.09
1.347	21.34	0.012	0.081	31.92	1.347	20.13	0.008	0.085	34.01
1.380	21.58	0.012	0.073	32.66	1.380	20.36	0.009	0.073	34.71
1.413	21.82	0.013	0.058	33.39	1.413	20.63	0.009	0.048	34.07
1.447	22.11	0.019	0.037	35.10	1.447	20.91	0.012	0.031	39.72
1.482	22.39	0.021	0.021	50.56	1.482	21.19	0.013	0.015	53.78
1.518	22.71	0.024	0.002	-128.20	1.518	21.51	0.015	0.005	36.15
1.554	23.00	0.028	0.013	-34.15	1.554	21.80	0.017	0.008	-42.98
1.592	23.34	0.032	0.012	-43.40	1.592	22.15	0.020	0.008	-53.55
1.630	23.69	0.037	0.022	-41.00	1.630	22.48	0.023	0.023	-52.84
1.670	24.10	0.043	0.027	-41.49	1.670	22.85	0.026	0.037	-48.16
1.710	24.45	0.049	0.047	-41.49	1.710	23.23	0.031	0.050	-42.17
1.751	24.91	0.058	0.051	-49.08	1.751	23.64	0.037	0.070	-45.15
1.793	25.30	0.070	0.086	-42.10	1.793	24.11	0.046	0.065	-38.57
1.837	25.82	0.086	0.081	-35.41	1.837	24.60	0.059	0.090	-36.89
1.881	26.12	0.101	0.144	-33.56	1.881	25.05	0.075	0.096	-24.82
1.926	26.94	0.153	0.107	-35.65	1.926	25.58	0.103	0.111	-18.96
1.973	27.17	0.166	0.123	-38.56	1.973	25.69	0.112	0.213	-18.96
2.020	27.16	0.170	0.241	-33.34	2.020	26.28	0.160	0.221	-21.42
2.069	28.10	0.287	0.206	-42.19	2.069	27.43	0.351	0.154	-33.18
2.119	28.75	0.420	0.206	-42.19	2.119	27.70	0.426	0.154	-33.18
2.170	29.51	0.685	0.206	-42.19	2.170	27.96	0.514	0.154	-33.18

Notes. Column 1: Semi-major axis in the g band. Column 2: Azimuthally averaged surface brightness in the g band. Column 3: Error on the surface brightness in the g band. Column 4: Ellipticity in the g band. Column 5: Position angle in the g band. Column 6: Semi-major axis in the i band. Column 7: Azimuthally averaged surface brightness in the i band. Column 8: Error on the surface brightness in the i band. Column 9: Ellipticity in the i band. Column 10: Position angle in the i band.

Table C.7. Surface photometry of UGC 7636.

$a_g^{1/4}$	μ_g	$\sigma(\mu_g)$	ϵ_g	$P.A._g$	$a_i^{1/4}$	μ_i	$\sigma(\mu_i)$	ϵ_i	$P.A._i$
[arcsec]	[mag/arcsec ²]	[mag/arcsec ²]		[deg]	[arcsec]	[mag/arcsec ²]	[mag/arcsec ²]		[deg]
1.012	22.66	0.042	0.390	0.00	1.012	22.26	0.040	0.390	0.00
1.037	22.66	0.040	0.390	0.00	1.037	22.26	0.038	0.390	0.00
1.062	22.66	0.039	0.390	0.00	1.062	22.26	0.037	0.390	0.00
1.087	22.67	0.037	0.390	0.00	1.087	22.25	0.036	0.390	0.00
1.113	22.67	0.036	0.390	0.00	1.113	22.24	0.034	0.390	0.00
1.140	22.67	0.034	0.390	0.00	1.140	22.24	0.033	0.390	0.00
1.168	22.67	0.033	0.390	0.00	1.168	22.24	0.032	0.390	0.00
1.196	22.67	0.032	0.390	0.00	1.196	22.23	0.031	0.390	0.00
1.225	22.67	0.031	0.390	0.00	1.225	22.23	0.030	0.390	0.00
1.254	22.67	0.030	0.390	0.00	1.254	22.22	0.029	0.390	0.00
1.285	22.65	0.028	0.390	0.00	1.285	22.22	0.028	0.390	0.00
1.316	22.64	0.027	0.390	0.00	1.316	22.24	0.028	0.390	0.00
1.347	22.65	0.026	0.390	0.00	1.347	22.24	0.027	0.390	0.00
1.380	22.65	0.026	0.390	0.00	1.380	22.27	0.027	0.390	0.00
1.413	22.66	0.025	0.390	0.00	1.413	22.27	0.026	0.390	0.00
1.447	22.67	0.034	0.390	0.00	1.447	22.29	0.034	0.390	0.00
1.482	22.68	0.034	0.390	0.00	1.482	22.28	0.033	0.390	0.00
1.518	22.70	0.034	0.390	0.00	1.518	22.29	0.034	0.390	0.00
1.554	22.70	0.034	0.390	0.00	1.554	22.28	0.034	0.390	0.00
1.592	22.71	0.034	0.390	0.00	1.592	22.32	0.034	0.390	0.00
1.630	22.72	0.034	0.390	0.00	1.630	22.35	0.035	0.390	0.00
1.670	22.77	0.034	0.390	0.00	1.670	22.37	0.034	0.390	0.00
1.710	22.82	0.034	0.390	0.00	1.710	22.40	0.034	0.390	0.00
1.751	22.88	0.033	0.390	0.00	1.751	22.45	0.034	0.390	0.00
1.793	22.95	0.034	0.390	0.00	1.793	22.50	0.034	0.390	0.00
1.837	23.01	0.034	0.390	0.00	1.837	22.55	0.034	0.390	0.00
1.881	23.06	0.033	0.390	0.00	1.881	22.59	0.034	0.390	0.00
1.926	23.12	0.033	0.390	0.00	1.926	22.65	0.034	0.390	0.00
1.973	23.19	0.034	0.390	0.00	1.973	22.70	0.034	0.390	0.00
2.020	23.35	0.037	0.390	0.00	2.020	22.83	0.038	0.390	0.00
2.069	23.44	0.038	0.390	0.00	2.069	22.92	0.039	0.390	0.00
2.119	23.53	0.039	0.390	0.00	2.119	23.00	0.040	0.390	0.00
2.170	23.66	0.041	0.390	0.00	2.170	23.12	0.043	0.390	0.00
2.222	23.81	0.044	0.390	0.00	2.222	23.22	0.046	0.390	0.00
2.276	23.99	0.049	0.390	0.00	2.276	23.37	0.050	0.390	0.00
2.331	24.17	0.054	0.390	0.00	2.331	23.50	0.055	0.390	0.00
2.387	24.31	0.058	0.390	0.00	2.387	23.64	0.060	0.390	0.00
2.444	24.46	0.063	0.390	0.00	2.444	23.75	0.065	0.390	0.00
2.503	24.60	0.069	0.390	0.00	2.503	23.88	0.072	0.390	0.00
2.564	24.79	0.078	0.390	0.00	2.564	24.02	0.079	0.390	0.00
2.626	24.92	0.085	0.390	0.00	2.626	24.13	0.086	0.390	0.00
2.689	25.06	0.092	0.390	0.00	2.689	24.21	0.091	0.390	0.00
2.754	25.18	0.099	0.390	0.00	2.754	24.30	0.097	0.390	0.00
2.820	25.27	0.107	0.390	0.00	2.820	24.42	0.108	0.390	0.00
2.888	25.54	0.125	0.390	0.00	2.888	24.66	0.131	0.390	0.00
2.958	25.74	0.141	0.390	0.00	2.958	24.83	0.149	0.390	0.00
3.029	26.06	0.170	0.390	0.00	3.029	25.08	0.182	0.390	0.00
3.102	26.49	0.213	0.390	0.00	3.102	25.37	0.229	0.390	0.00
3.177	26.77	0.246	0.390	0.00	3.177	25.51	0.256	0.390	0.00
3.254	27.14	0.287	0.390	0.00	3.254	25.69	0.294	0.390	0.00
3.332	27.71	0.357	0.390	0.00	3.332	25.91	0.351	0.390	0.00
3.412	28.48	0.443	0.390	0.00	3.412	26.27	0.479	0.390	0.00
3.495	28.74	0.469	0.390	0.00	3.495	26.31	0.499	0.390	0.00
3.579	31.13	0.576	0.390	0.00	3.579	26.87	0.807	0.390	0.00
3.665	30.07	0.553	0.390	0.00	3.665	27.08	0.972	0.390	0.00
3.844	29.83	0.565	0.390	0.00	3.844	26.83	0.798	0.390	0.00
3.937	29.42	0.561	0.390	0.00	3.937	26.93	0.885	0.390	0.00

Notes. Column 1: Semi-major axis in the g band. Column 2: Azimuthally averaged surface brightness in the g band. Column 3: Error on the surface brightness in the g band. Column 4: Ellipticity in the g band. Column 5: Position angle in the g band. Column 6: Semi-major axis in the i band. Column 7: Azimuthally averaged surface brightness in the i band. Column 8: Error on the surface brightness in the i band. Column 9: Ellipticity in the i band. Column 10: Position angle in the i band.